Antal Kerpely Doctoral School of Materials Science and Technology

Deformation Field, Texture Evolution, and Grain Refinement in Friction-Assisted Lateral Extrusion Process

PhD dissertation

PhD candidate

Ali Amininejad

Supervisors

Prof. Laszlo S Toth

Prof. Valeria Mertinger

Institute of Physical Metallurgy, Metal-forming and Nanotechnology

University of Miskolc

Miskolc, Hungary

2026

Supervisors Recommendation

Ali Amininejad (Ali in the following) is coming from Iran, with a master's degree, obtained after brilliant university studies in materials science and engineering. His research topic in Iran was focusing on thermo-mechanical behavior of austenitic stainless steel, which lead to four journal publications, him being the first author each time. He was accepted for Ph.D. studies at the University of Miskolc in 2022. In Miskolc, he agreed to change his research topic, which is severe plastic deformation of metals, focusing on the FALEP process (Friction-Assisted Lateral Extrusion Process).

Ali became rapidly familiar with his new research area. He showed high interest and had many questions about the mechanics of processing as well as on the microstructure developments in FALEP. Indeed, when he started, there was not many publications and experiments/theory about FALEP, because FALEP had been re-discovered not long ago, in the research group of Laszlo S. Toth in Metz, France. Ali was very much interested in both the experimental part and in the theoretical issues.

Before going into deep theoretical studies in the microstructure evolution in SPD, Ali first wanted to understand the mechanics of the FALEP process. He planned a series of experiments in which he placed flow line markers within split aluminum samples, that could reveal the deformed flow lines during the passage of the metal in the die. He carried out these experiments in the LEM3 laboratory in Metz, during a three-months research period. From the experimental flow lines, he was able to deduce the major characteristics of the deformation. He discovered that the deformation is not homogeneous for certain geometries of the extrusion process, and there are deviations from the homogeneous simple shear modeling of FALEP. For quantitative modeling, he developed a new flow line model, which permits a full understanding of the deformation field. Apart from the geometrical validation, he verified the new approach also by viscoplastic self-consistent polycrystal modeling through texture simulations. This work led to a Q1 publication in the Materials Characterization journal.

The next step was the modeling of the microstructure in SPD, using experimental observations from FALEP of aluminum and copper. Ali was reworking and completing the previous grain fragmentation model presented in 2010 by S. Toth et al. For understanding the complex process of grain fragmentation, he first examined in detail the orientation flow field in shear deformation, then reworked the lattice curvature-based fragmentation theory with a four-level fractal approach, both for fragmentation and also for coalescence of the millions of voxels that composed an initially large grain. This work required good expertise in numerical simulations,

that he carried out with very good understanding and success. His findings on the simultaneous occurrence on fragmentation and coalescence are the first in the field of SPD. These results were one of the highlights at the NanoSPD9 conference in 2025, and a ground-breaking basic publication is being prepared now about these findings.

Ali is a deep-thinking, very careful and creative researcher. He reached in the above-mentioned research fields an internationally well recognized expertise. Therefore, both of his supervisors are supporting, without hesitation, the obtention of his Ph.D. degree at the University of Miskolc.

Miskolc, 2026.03.16

Prof. Laszlo S. Toth

Prof. Valeria Mertinger

Supervisors

Table of Contents

List of Abbreviations

Abbreviation	Definition
SPD	Severe plastic deformation
FALEP	Friction-assisted lateral extrusion process
HEM	Homogeneous equivalent medium
VPSC	Viscoplastic self-consistent
UFG	Ultrafine-grained
HPT	High-pressure torsion
ECAP	Equal-channel angular pressing
ARB	Accumulative roll bonding
HPTT	High-pressure tube twisting
NECAP	Non-equal channel angular pressing
ECMAP	Equal-channel multi-angular pressing
T-ECAP	T-shaped equal channel angular pressing
FCC	Face-centered cubic
BCC	Body-centered cubic
PDZ	Plastic deformation zone
HAGB	High-angle grain boundary
LAGB	Low-angle grain boundary
DRX	Dynamic recrystallization
CDRX	Continuous dynamic recrystallization
DDRX	Discontinuous dynamic recrystallization
EBSD	Electron back scattering diffraction
ODF	Orientation distribution function
LCE	Linear converging extrusion
GND	Geometrically necessary dislocation
SSD	Statistically stored dislocations
GNB	Geometrically necessary boundaries
TEM	Transmission electron microscopy
CPFEM	Crystal plasticity finite element method
CA	Cellular automaton
GOS	Grain orientation spread
KAM	Kernel average misorientation

Introduction

A central objective of materials science and engineering is to understand and control the interrelationship between processing routes, the microstructure, and the macroscopic properties and performance of materials. Materials researchers primarily aim to design microstructures that yield desirable properties. Among the various processing strategies, metal forming plays a key role, as it allows both the tailoring microstructures and producing products with specific shapes. The growing demand for materials with enhanced properties and functionality across diverse industrial applications necessitates the development of advanced metal forming methods. Severe plastic deformation (SPD) techniques represent effective strategies for manufacturing high-strength materials and facilitating lightweight design. By imposing very large plastic strains, SPD processes induce significant microstructural changes in polycrystalline materials, most notably grain refinement and crystallographic texture evolution. At sufficiently high strain levels, the progressive subdivision of grains leads to a substantial reduction in grain size and improvement of the material properties, especially the strength-ductility balance. This process is commonly referred to as “grain refinement”. The evolution of grain orientation, referred to as “texture evolution” in materials science, is also critical to the properties of crystalline materials. Texture evolution is not random but is governed by the crystal structure of the material and the imposed deformation mode, as described by polycrystal plasticity theories. Since texture strongly influences the anisotropy of mechanical and physical properties, understanding and predicting texture evolution is a crucial aspect of microstructure design in SPD-processed materials.

The present study addresses these issues through a combined experimental and modeling investigations. This study is structured in two closely related parts. In the first part, the deformation behavior in the friction-assisted lateral extrusion (FALEP), a novel SPD technique, is examined in detail. Based on direct experimental observations of material flow, a new analytical flow line model is developed to describe the deformation field in FALEP. Using this model, the crystallographic texture evolution during FALEP processing is successfully simulated and quantitatively compared with experimental measurements.

The second part of the thesis focuses on the mechanisms of grain refinement during severe plastic deformation and their relationship with texture evolution, with particular emphasis on FALEP processing. A robust modeling framework that combines experimental observations with crystal plasticity theory is established. The proposed model enables, for the first time, both

qualitative and quantitative analysis of grain fragmentation and coalescence within a unified framework.

For each part of the thesis, a literature review is presented covering key experimental and theoretical studies. The experimental procedures and results are then described and discussed in detail. The theoretical foundations and principles of the proposed modeling approaches are introduced, together with their potential outputs. Finally, the simulation results generated by the proposed models are presented and examined in detail. Through integrated experimental and theoretical analyses, the thesis aims to provide new insights into deformation kinematics, texture evolution, and grain refinement mechanisms in FALEP and related severe plastic deformation processes.

Part 1: Deformation Field and Texture Analysis in FALEP

1.1. Literature Review

1.1.1. Polycrystal Plasticity

Plasticity theory is a branch of continuum mechanics that describes the constitutive relationship between stress and strain fields in solids, particularly in metals, subjected to plastic deformation. In polycrystalline metals, macroscopic plastic deformation results from the interactions of a large number of crystallites with different orientations. From a materials science perspective, plastic deformation is governed by microscale lattice-defect activities, primarily dislocation slip. The primary objective of polycrystal plasticity theory is to establish a relationship between the macroscopic stress-strain response of a representative polycrystalline volume and the local grain-scale stress and strain (or strain rate) fields in each individual crystal [1-3].

During plastic deformation, a material element can experience both strain and rotation. The velocity gradient tensor $\underline{\underline{L}}$ contains strain rate and rotation rate tensors, which is generally determined by the test geometry and experimental conditions. The velocity gradient tensor can be decomposed into two tensors: the symmetric part $\underline{\underline{\dot{\varepsilon}}}$ represents the strain rate tensor, while the antisymmetric part $\underline{\underline{\dot{\beta}}}$ corresponds to the rigid body rotation [4]:

$$\underline{\underline{L}} = \underline{\underline{\dot{\varepsilon}}} + \underline{\underline{\dot{\beta}}} \tag{1}$$

Where:

$$\dot{\varepsilon}_{ij} = \frac{1}{2}\left(L_{ij} + L_{ji}\right) \tag{1}$$

$$\dot{\beta}_{ij} = \frac{1}{2}\left(L_{ij} - L_{ji}\right) \tag{3}$$

Considering the plastic deformation in a crystal is governed by dislocation slip, one can consider a velocity gradient tensor for the crystal:

$$L_{ij}^{g} = m_{ij}\,\dot{\gamma} \tag{4}$$

where m_{ij} is Schmid orientation tensor, obtained from the slip plane normal (n) and the slip direction (b), and $\dot{\gamma}$ is the slip rate. In the case of multiple slip system (N), the contribution of the individual slip systems (s) needs to be considered:

$$L_{ij}^{g} = \sum_{s}^{N} m_{ij}^{(s)}\,\dot{\gamma}^{(s)} \tag{5}$$

Similar to macroscopic velocity gradient ($\underline{\underline{L}}$), the velocity gradient of crystal ($\underline{\underline{L}}^{\mathrm{g}}$) includes a symmetric part, strain rate tensor ($\dot{\varepsilon}_{ij}^{g}$), and an antisymmetric part, plastic spin ($\dot{\omega}_{ij}^{g}$):

$$L_{ij}^{g} = \dot{\varepsilon}_{ij}^{g} + \dot{\omega}_{ij}^{g} \tag{6}$$

$$\dot{\varepsilon}_{ij}^{g} = \frac{1}{2}\left(L_{ij}^{g} + L_{ji}^{g}\right) = \sum_{s}^{N} \frac{1}{2}\left(m_{ij}^{(s)} + m_{ji}^{(s)}\right)\dot{\gamma}^{(s)} \tag{7}$$

$$\dot{\omega}_{ij}^{g} = \frac{1}{2}\left(L_{ij}^{g} - L_{ji}^{g}\right) = \sum_{s}^{N} \frac{1}{2}\left(m_{ij}^{(s)} - m_{ji}^{(s)}\right)\dot{\gamma}^{(s)} \tag{8}$$

For a single crystal, the strain rate tensor associated with the imposed velocity gradient is equal to the microscopic strain rate tensor, as plastic deformation occurs by slip. However, it does not mean that $\underline{\underline{L}}$ and $\underline{\underline{L}}^{\mathrm{g}}$ are identical, since each tensor contains an antisymmetric component (rotation tensor). Therefore, the difference between the two velocity gradients corresponds to a rotation tensor, which is called the lattice rotation $\underline{\underline{\dot{\Omega}}}$:

$$\underline{\underline{\dot{\Omega}}} = \underline{\underline{L}} - \underline{\underline{L}}^{g} \tag{9}$$

Or:

$$\underline{\underline{\dot{\Omega}}} = \underline{\underline{\dot{\beta}}} - \underline{\underline{\dot{\omega}}}^{g} \tag{10}$$

For multiple slip (N):

$$\dot{\Omega}_{ij} = L_{ij} - \sum_{s}^{N} m_{ij}^{(s)} \dot{\gamma}^{(s)} \tag{11}$$

The lattice rotation rate tensor determines the evolution of crystal orientation during plastic deformation. Therefore, it is a critical parameter for evaluating the crystallographic texture of deformed materials. For a prescribed macroscopic velocity gradient tensor, Eq. (11) can be solved only if the contribution of each slip system in deformation ($\dot{\gamma}^{(s)}$) is determined. From Eq. (7), the slip rate of each slip system can be calculated by solving five independent linear equations, corresponding to the five independent components of the strain rate tensor, including three shear components and two normal components. To solve these five equations, exactly five independent slip systems are needed. However, for example, in a face-centered cubic (FCC) crystal, twelve slip systems are available, leading to ambiguity in determining the slip rate of different slip systems.

To overcome this ambiguity, Taylor proposed selecting a combination of slip systems that minimize the sum of slip rates [5]. However, the problem with this assumption is that different combinations can yield the same sum of slips. Thus, the ambiguity remains, and a unique solution cannot be obtained. Furthermore, the role of stress is not considered in this case. Meanwhile, the Schmid criterion suggests that the slip of a crystal on its slip plane requires a critical shear stress value. Below the critical value, there is no slip, and a stress state exceeding this value is not permitted. In the Schmid criterion, however, there is no relation between stress and slip rate. Once the resolved shear stress reaches the critical value, slip can occur at different rates. Moreover, different stress states can result in the same strain rate.

Experimental observations indicate that the stress response of a tested material depends on the applied strain rate [6, 7]. This phenomenon is referred to as rate-sensitive behavior. Considering that plastic deformation is governed by slip, the same rate-sensitive behavior should exist for dislocation slip [8]. The local stress-strain relationship in a crystal can be modelled by a viscoplastic power law function relating the shear rate ($\dot{\gamma}^{(s)}$) to the resolved shear stress ($\tau^{(s)}$):

$$\dot{\gamma}^{(s)} = \dot{\gamma}_0^{(s)} \frac{\tau^{(s)}}{\tau_0^{(s)}} \left| \frac{\tau^{(s)}}{\tau_0^{(s)}} \right|^{\frac{1}{m}-1} \tag{12}$$

Here, m is the viscosity coefficient, which is independent of the strain rate value [9]. $\dot{\gamma}_0^{(s)}$ and $\tau_0^{(s)}$ are the reference shear rate and the reference shear stress in the slip system indexed by (s), respectively. The resolved shear stress ($\tau^{(s)}$) can be obtained by the projection of the macroscopic stress tensor (σ_{ij}) on the slip system:

$$\tau^{(s)} = \sigma_{ij} \,.\, m_{ij}^{(s)} \tag{13}$$

By replacing Eqs. (12) and (13) in Eq. (7), we get:

$$\dot{\varepsilon}_{ij}^{g} = \dot{\gamma}_0^{(s)} \sum_{s}^{N} \frac{1}{2}\left(m_{ij}^{(s)} + m_{ji}^{(s)}\right) \frac{\sigma_{ij} \,.\, m_{ij}^{(s)} \left|\sigma_{ij} \,.\, m_{ij}^{(s)}\right|^{\frac{1}{m}-1}}{\left(\tau_0^{(s)}\right)^{\frac{1}{m}}} \tag{14}$$

Eq. (14) provides a direct relation between the imposed strain rate and stress tensor in a single crystal. The ambiguity problems are solved in the viscoplastic slip approach since the number of unknowns, stress components, is equal to the number of equations. However, the equation is strongly non-linear and needs iteration techniques to be solved.

The presented crystal plasticity equations are valid for single crystals, while most engineering materials are polycrystalline, consisting of numerous grains with varying orientations. Extending crystal plasticity theory from the single crystal to the polycrystal level requires additional assumptions to account for interactions between grains. Polycrystal plasticity models address this problem by specifying the distribution of strain and stress among individual crystals within a representative volume element. Depending on whether uniform strain, uniform stress, or intermediate interaction conditions are assumed, different polycrystal plasticity models have been proposed, including the Taylor [5], Sachs [10], static [11], relaxed constraints [12], and self-consistent models [13, 14]. The Taylor and the self-consistent models are widely used for texture prediction and deformation modeling in polycrystalline metals. The Taylor model assumes that all grains in a polycrystal deform exactly the same way as the sample. As a result, the local velocity gradient of each grain is equal to the macroscopic velocity gradient:

$$L_{ij}^{g} = L_{ij} \tag{15}$$

Considering that the deformation of the grains is the same, the compatibility between grains is satisfied. However, the crystals within the sample have different orientations, which means the stress states must vary to satisfy the same deformation for all the grains. Within a grain, the stress state is constant, and the equilibrium equation is satisfied. However, at the grain boundaries, the stress state of each side is different, meaning that the equilibrium equation is violated. The volume around the grain boundary is also affected by this non-equilibrium condition. The Taylor model assumes that this volume is negligible.

The most comprehensive polycrystal plasticity models are represented by self-consistent approaches, which can take into account the shape of the grain via the interaction that it has with the surrounding polycrystalline aggregate. In self-consistent models, each grain is treated as an inclusion embedded in a homogeneous equivalent medium (HEM). The unique advantage of this model is that the shape evolution of each grain during large deformation can be followed. Moreover, the local stress and strain state of each crystal can vary from the macroscopic average, meaning that the intergranular heterogeneity is captured in a physically realistic manner. Self-consistency means that macroscopic mechanical behavior is the average of the behavior of the constituent crystals. Molinari et al. [14] developed an early self-consistent viscoplastic (VPSC) formulation for predicting macroscopic response and texture evolution of polycrystals during large deformations. Later, this framework was reformulated by Lebensohn and Tome [13]. The implementation of this model led to the development of an open-access computational tool, commonly referred to as the Los Alamos VPSC code, which has become one of the most widely used codes for simulating texture evolution and anisotropic plastic behavior in polycrystalline materials. The formulation of the self-consistent crystal plasticity approach can be expressed by the interaction law [15]:

$$s^{\mathrm{g}} - S = s^{\mathrm{g}} - A^{s} : D = \alpha\left(\Gamma^{\mathrm{sgg}^{-1}} + A^{s}\right)(d^{\mathrm{g}} - D) \tag{16}$$

Here S and D denote the macroscopic deviatoric stress and strain rate tensors, respectively, while s^{g} and d^{g} are the corresponding microscopic (grain-level) deviatoric stress and strain rate tensors. The fourth-order tensor A^{s} is the macroscopic secant modulus of the polycrystal. The tensor $\Gamma^{\mathrm{sgg}^{-1}}$accounts for the shape of the grain. The scalar positive parameter α was introduced to calibrate the interaction law [15].

1.1.2. Severe Plastic Deformation

Over the past decades, severe plastic deformation (SPD) techniques have attracted considerable attention due to their capability to produce bulk ultrafine-grained (UFG) structures by imposing extremely large strains. While conventional metal-forming techniques, such as rolling, forging, and drawing, exhibit technical limitations for large plastic deformation, SPD techniques have been shown to be effective alternatives for this purpose [16, 17]. Numerous studies have demonstrated that UFG microstructures generated by SPD processing lead to significant improvements in the physical, mechanical, and functional properties of materials [18, 19]. Moreover, the high hydrostatic pressure existing in most SPD techniques effectively suppresses the initiation and growth of micro-cracks and voids, thereby facilitating the deformation of hard-to-deform materials. Although metals have been the primary focus of SPD research, a broad range of other materials, including ceramics [20], metallic glasses [21], polymers [22], and semiconductors [23], have also been successfully processed using SPD techniques.

Various SPD techniques have been developed, among which high-pressure torsion (HPT), equal-channel angular pressing (ECAP), and accumulative roll bonding (ARB) are the most widely used. In 1935, Bridgman introduced the first version of the HPT process by combining high hydrostatic pressure and large shear strain using a rotational anvil [24]. Fig. 1a shows a schematic illustration of the HPT process. In this technique, a disk-shaped sample is compressed between two anvils under an applied pressure *P*. While one anvil remains fixed, the other rotates, imposing shear strain on the sample. With increasing anvil rotation (number of turns), the imposed shear strain increases, while the applied pressure prevents the sample from breaking. HPT is therefore highly effective in achieving very high equivalent strains (exceeding 1000 [25]), and in refining the microstructure down to a minimum attainable (steady-state) grain size. However, the technical barriers related to sample size and strain inhomogeneity limit the industrial applications of the conventional HPT process. A variant of the HPT process, known as high-pressure tube twisting (HPTT), was proposed in 2009 [26], in which, instead of a disk-shaped sample, a thin-walled tube specimen is subjected to very large shear strains. Compared with conventional HPT disks, the HPTT process provides more practical sample geometry as tubes, which can be used for a wider range of engineering applications. The initial HPPT configuration was later modified to further increase the imposed hydrostatic pressure by applying the axial force directly to the tube wall, as schematically shown in Fig. 1b [27].

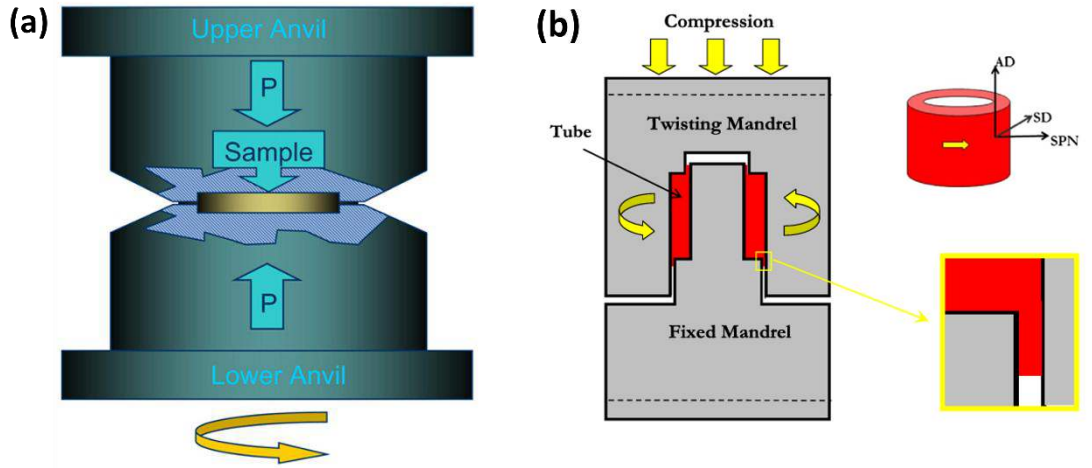

Fig. 1. Schematic illustration of **(a)** high-pressure torsion (HPT) [28], and **(b)** high-pressure tube twisting (HPTT) [27].

Invented by Segal in 1974 [29, 30], ECAP has become one of the most widely used SPD techniques for producing UFG microstructures through applying large plastic strains to materials. The significant potential of ECAP for fabricating bulk UFG materials was widely recognized in the early 1990s, thanks to the contributions of Valiev and co-workers to this field [31, 32]. ECAP is a relatively simple and versatile processing technique that can be applied to a wide range of materials [33]. As schematically illustrated in Fig. 2a, in this technique, a workpiece is introduced at the top of a die and pressed through two channels with identical cross sections to extrude from the exit channel. During processing, the material undergoes shear deformation while retaining its original dimensions, which allows the procedure to be repeated multiple times. The ECAP sample is typically in the form of a billet, and depending on the die design and press capacity, relatively large bulk specimens can be processed. However, during ECAP processing, the stress-strain distribution is generally non-uniform across the billet, leading to variations in microstructure and texture [34-36]. An efficient solution to overcome this problem is to apply back-pressure at the exit channel of the ECAP die, which improves strain homogeneity and retains the sample shape for multiple-pass processing [37, 38]. In addition, the length of work-piece is limited in ECAP processing due to a limited travel distance of the press arm and the possibility of bending of long-length samples, which makes ECAP a discontinuous process and reduces its production efficiency. To address this issue, a continuous ECAP variant, known as ECAP-Conform, was developed to enable the continuous processing of UFG materials for large-scale production [39]. A schematic illustration of the ECAP-Conform process is presented in Fig. 2b. Another limitation of the ECAP technique is that it usually requires several passes, commonly between four and eight passes depending on the material, to achieve a homogeneous UFG microstructure. From an industrial perspective,

reducing the number of required passes is therefore highly desirable. To this end, a modified ECAP technique, referred to as non-equal channel angular pressing (NECAP), was proposed, in which the exit channel has a smaller cross-section than the ingoing channel, leading to a larger equivalent strain per pass (Fig. 2c) [40, 41]. Meanwhile, numerous efforts have been made to modify the ECAP technique and expand its applications, including equal-channel multi-angular pressing (ECMAP) [42], rotary-die ECAP [43], cross-ECAP [44], and T-shaped ECAP (T-ECAP) [45, 46]. Nevertheless, the diversity of SPD techniques extends far beyond the methods discussed here. The rapidly growing demand for UFG materials requires the continuous development of novel SPD techniques to expand both the range of product geometries and the achievable production scale. A comprehensive overview of a wide variety of SPD techniques can be found in Ref. [47].

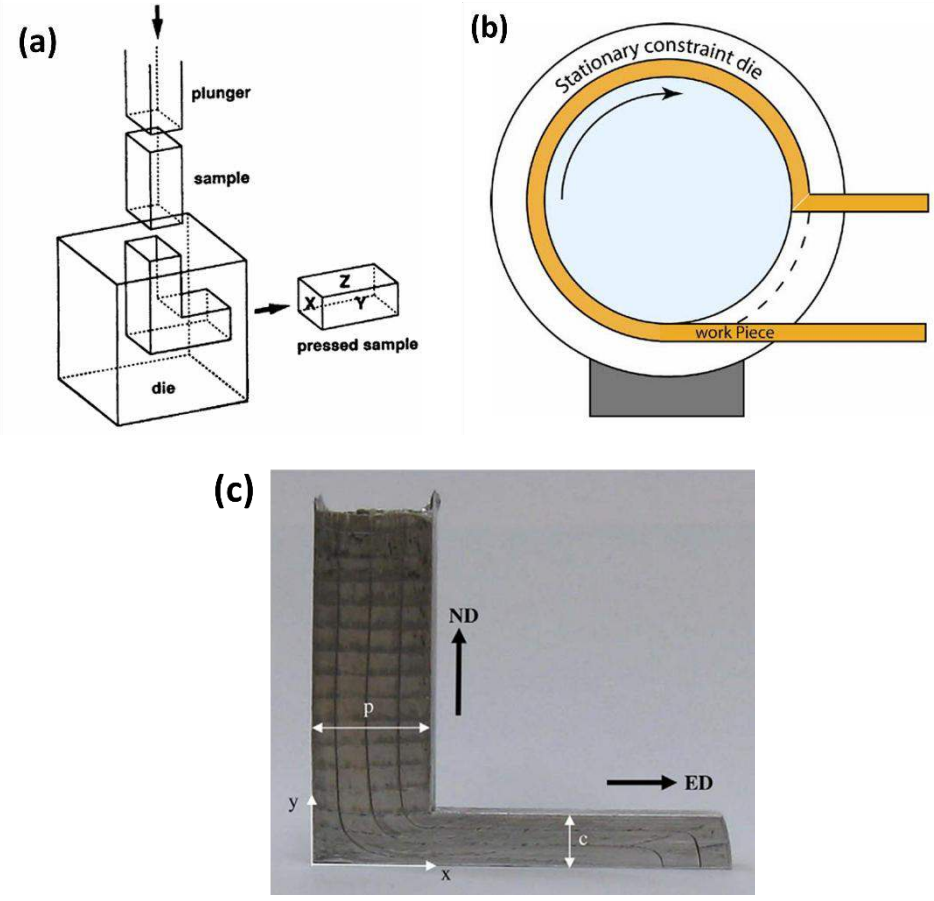

Fig. 2. Schematic illustration of **(a)** equal-channel angular pressing (ECAP) [48], **(b)** ECAP-Conform [39]. **(c)** Photo of a sample after non-equal channel angular pressing (NECAP) [40].

1.1.3. Modeling of Deformation Behavior in ECAP Variants

1.1.3.1. Simple Shear Model

Segal proposed an analytical model to describe the strain field in ECAP, in which the deformation mode is idealized as simple shear occurring along the intersection plane of the two

channels [49, 50]. Based on the simple shear model, the shear strain imposed during a single ECAP pass is given by [51]:

$$\gamma = 2\cot\left(\frac{\phi}{2}+\frac{\Psi}{2}\right)+\Psi\csc\left(\frac{\phi}{2}+\frac{\Psi}{2}\right) \tag{17}$$

Here, ϕ and Ψ are the channel angle and the curvature angle of the outer corner of the die, respectively (Fig. 3a). The corresponding equivalent von Mises plastic strain can then be expressed as:

$$\bar{\varepsilon} = \frac{\gamma}{\sqrt{3}} \tag{18}$$

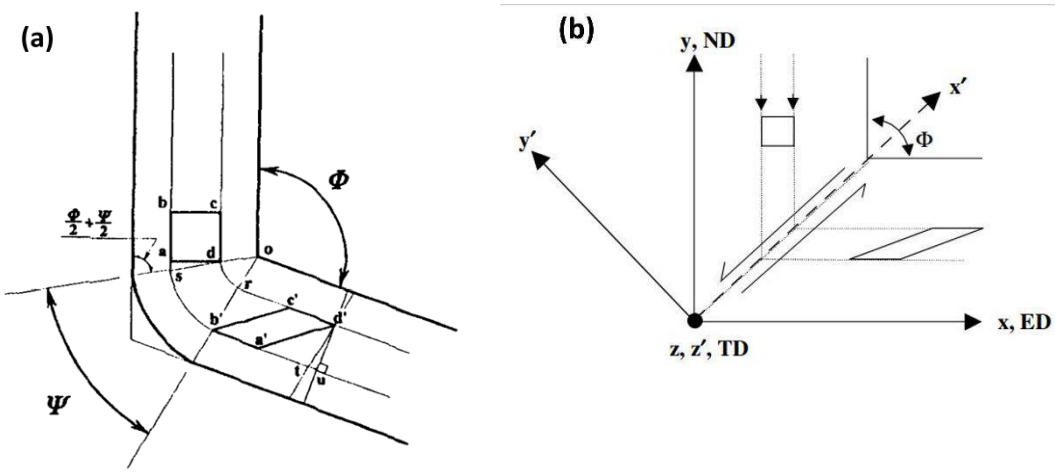

Fig. 3. **(a)** Principle of deformation in ECAP [51], **(b)** the position of the shear plane in a 90° ECAP die [52].

For a sharp outer corner ($\Psi = 0$), Eq. (17) simplifies to:

$$\gamma = 2\cot\left(\frac{\phi}{2}\right) \tag{19}$$

When the cross-sectional dimensions of the two channels are different (NECAP), the imposed shear strain can be expressed as [53]:

$$\gamma = \cot\alpha + \cot\beta \tag{20}$$

where α and β denote the angles between the shear plane and the ingoing and exit channels, respectively. For a 90° die, Eq. (20) can be rewritten as [54]:

$$\gamma = \frac{p}{c} + \frac{c}{p} \tag{21}$$

where p and c represent the thicknesses of the ingoing and exit channels, respectively. Fig. 3b indicates the position of the shear plane in a 90° ECAP die. Assuming ideal simple shear deformation, the velocity gradient tensor in the shear reference system (x'-y'-z') can be written as (note that $\dot{\gamma}$ is positive):

$$\boldsymbol{L}' = \begin{pmatrix} 0 & -\dot{\gamma} & 0 \\ 0 & 0 & 0 \\ 0 & 0 & 0 \end{pmatrix} \tag{22}$$

When the velocity gradient is expressed in the die reference system (x-y-z), we obtain:

$$\boldsymbol{L} = \frac{\dot{\gamma}}{2} \begin{pmatrix} 1 & -1 & 0 \\ 1 & -1 & 0 \\ 0 & 0 & 0 \end{pmatrix} \tag{23}$$

This velocity gradient corresponds to tension in the extrusion direction (x-axis), compression in the normal direction (y-axis), and a pure rigid body rotation around the z-axis. Eq. (23) can be readily incorporated as an imposed velocity gradient into polycrystal plasticity models. Using the simple shear model, the ideal texture components formed during ECAP processing with a 90° die can be derived by applying an additional 45° increase in the φ_1 Euler angle to the ideal shear orientations. This transformation corresponds to a 45° clockwise rotation about the z-axis, which aligns the shear plane normal (y') with respect to the normal direction of the ECAP die, as schematically illustrated in Fig. 3b. Table 1 presents the ideal shear and the ideal ECAP (90° die) texture components for FCC materials [55].

Table 1. Ideal shear and ideal ECAP (90° die) orientations for FCC materials [55].

Ideal shear orientations				Ideal ECAP orientations			
Notation	Euler angles[a] (°)			Notation	Euler angles (°)		
	φ_1	Φ	φ_2		φ_1	Φ	φ_2
A_1	35.26/215.26	45	0	A_{1E}	80.26/260.26	45	0
	125.26	90	45		170.26	90	45
A_2	144.74	45	0	A_{2E}	9.74/189.74	45	0
	54.74/234.74	90	45		99.74	90	45
A	0	35.26	45	A_E	45	35.26	45
Ab	180	35.26	45	Ab_E	225	35.26	45
B	0/120/240	54.74	45	B_E	45/165	54.74	45
Bb	60/180	54.74	45	Bb_E	105/225	54.74	45
C	90/270	45	0	C_E	135	45	0
	0/180	90	45		45/225	90	45

[a] Given in the φ_2 = 0° and 45° sections with φ_1 = 0-270° only.

Several studies have employed the simple shear model to describe deformation mode and predict texture evolution in ECAP and its variants. Li et al. [56] applied the simple shear model coupled with the Taylor and VPSC polycrystal plasticity models to predict the texture evolution of FCC and BCC (body-centered cubic) materials subjected to one pass of a 90° die ECAP. They demonstrated that the sign of simple shear deformation in ECAP is negative, and a positive shear strain leads to inappropriate interpretations of the texture results. Beyerlein et al. [57] used the VPSC approach with the simple shear model to predict texture evolution in copper during ECAP for four different processing routes (A, C, B_A, B_C). They also proposed an empirical grain subdivision model based on grain morphology to examine the effect of grain shape and grain refinement on texture evolution. Another study on the deformation behavior in ECAP [57] showed that the strain mode and deformation zone are strongly influenced by the die angle, friction conditions, and the application of back-pressure. It was shown that under conditions of low friction and in the absence of back pressure, the deformation zone becomes expanded, and plastic deformation is distributed over a wider region rather than being localized in a narrow shear plane, as assumed in the idealized simple shear model proposed by Segal. However, when a sharp die corner is employed and back pressure is applied, the strain distribution becomes more uniform and most closely approximates ideal simple shear occurring at the intersection plane of the two channels.

Numerous experiments [58-61] and simulations [62-65] have demonstrated that the strain distribution within the billet during ECAP processing is not fully uniform. The simple shear model is unable to capture the deformation heterogeneity during ECAP. Moreover, the model assumes that deformation takes place in a narrow region at the intersection plane of two channels, which is inconsistent with experimental observations, where deformation can occur over a relatively wide region at the intersection zone of two channels [66, 67]. The simple shear model describes the deformation in ECAP as a discontinuous process, in which each material element deforms by passing the intersection plane. Indeed, when the plastic deformation zone is idealized as a plane of infinitesimal thickness, the shear strain rate would be infinite, which is physically unrealistic.

1.1.3.2. Analytical Flow Models

Segal [50] proposed the first analytical model using the slip line theory for a sharp corner ECAP die ($\Psi = 0$), a rigid plastic material, and uniform friction. This analysis revealed that the plastic deformation zone (PDZ) expands into a fan-shaped region that is symmetric with respect to the channel intersection plane. In a later study [34], Segal extended the slip field analysis to ECAP dies with rounded corners ($\Psi > 0$) and reported that increasing the corner curvature leads to a progressive broadening of the PDZ. Building on Segal's work [34], Beyerlein and Tomé [68] proposed a new analytical model for material flow in ECAP, with circular flow lines within the PDZ. Two distinct plastic deformation zone configurations were considered for a 90° ECAP die: (i) a central fan deformation zone (Fig. 4a), and (ii) a two-part deformation zone consisting of a central fan in the upper region and a lower region with low-intensity shear deformation (Fig. 4b). Within this framework, the PDZ can be simply determined by a single parameter, α. It was found that for $\alpha < \pi/4$, the deformation mode is not limited to simple shear but a combination of biaxial straining, rotation, and shearing. In the case of a central fan-shaped PDZ, the deformation across the billet is uniform. In the two-part PDZ configuration, however, deformation is inhomogeneous, as the local deformation depends on the position of the material point. In the upper region, the flow line deformation and velocity gradients are similar to those in the central fan model, whereas in the lower region, deformation is reduced, and the rigid body rotation becomes dominant.

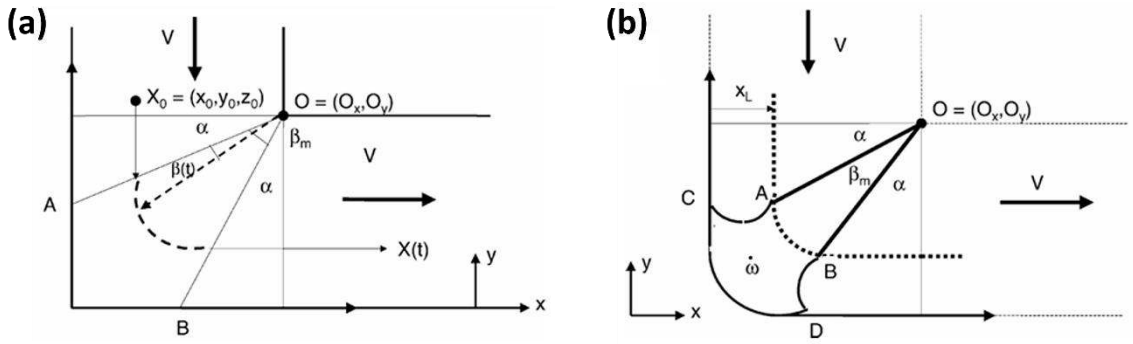

Fig. 4. Schematic of **(a)** central fan deformation zone, **(b)** a two-part plastic deformation zone (PDZ) within a central fan in the upper region and rotating lower region with angular velocity $\dot{\omega}$ (flow line shape is circular) [68].

Another fan-shaped flow line model was developed by Hasani and Toth for a 90° ECAP die [69]. It was found that the shape of the flow lines within the PDZ must be elliptical rather than circular. While Beyerlein and Tomé's [68] approach exhibits a discontinuity in the velocity gradient at the PDZ boundaries, this model describes deformation along the flow lines without such discontinuities. A schematic illustration of the PDZ and the corresponding geometry of the fan-shaped plastic zone is shown in Fig. 5. In the limiting case where the fan angle φ is zero, the flow line shape becomes parabolic, and the deformation mode is ideal simple shear.

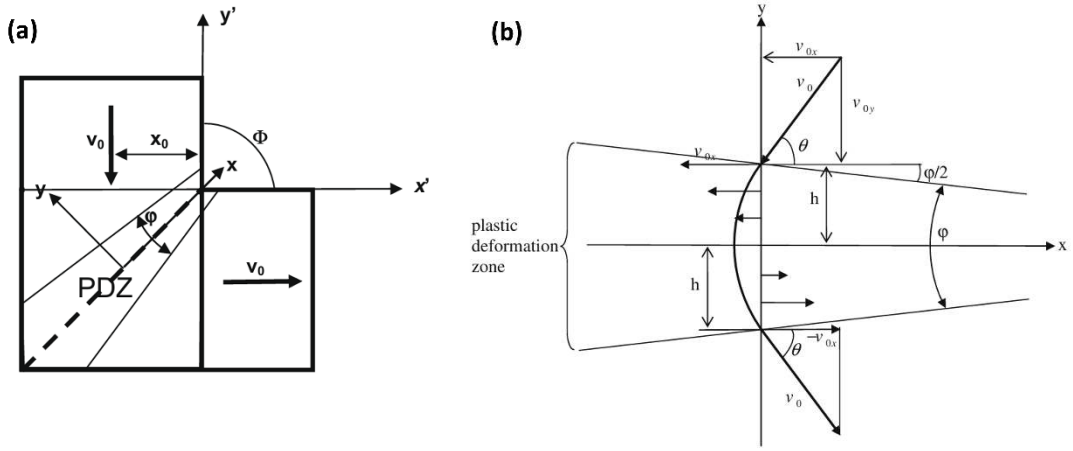

Fig. 5. Schematic of **(a)** PDZ and **(b)** fan-shaped plastic zone proposed in Ref. [69] (flow line shape is elliptical).

A widely accepted flow line model for describing plastic flow during ECAP with a 90° die was proposed by Toth and co-workers in 2004 [52]. In Toth's model, plastic deformation occurs continuously at the intersection zone of two channels. Furthermore, this approach allows for defining different deformation paths and strain levels across the billet thickness, thereby enabling heterogeneous deformation in ECAP processing to be considered. The flow line function is described by a power-law relationship, which can be expressed as:

$$\phi = (d - x)^n + (d - y)^n = (d - x_0)^n \tag{24}$$

Here, d is the diameter of the die, and x_0 determines the incoming and outgoing position of the flow line. The only parameter of the model is n, which controls the shape of the flow line. For $n = 2$, the flow line is circular, while for $n \to \infty$, the flow line consists of two straight lines joined at the symmetry plane of the die, corresponding to the limiting case of ideal simple shear deformation. Fig. 6 shows a schematic illustration of flow lines within the deformation zone. The flow line function is valid only in the intersection zone of the die, which is between the lines defined by y = d and x = d. Moreover, the flow line function represents a continuously curving trajectory. Inspired by the original flow line function (Eq. (24)), the authors later proposed a new function to describe material flow in a 120° ECAP die [70].

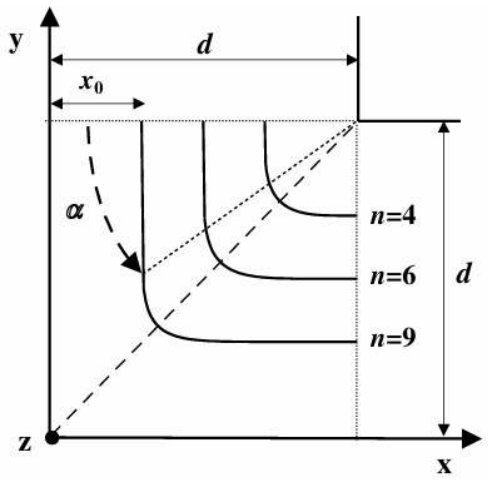

Fig. 6. Description of flow field by flow lines. n is the value of the exponent in the flow line equation proposed in Ref [52].

A modified version of the flow line function was proposed to analyze material deformation in NECAP, in which the difference in cross-sectional dimensions between the ingoing (p) and exit (c) channels must be explicitly considered. In this formulation, two additional parameters, k and m, were introduced to the original function to provide greater flexibility in controlling the shape of the flow lines [71]:

$$f = \left(1 - \frac{x}{p}\right)^n + m\left(1 - \frac{ky}{c}\right)^n = \left(1 - \frac{x_0}{p}\right)^n \tag{25}$$

where the newly introduced parameters allow the adjustment of the curvature and asymmetry of the flow lines, enabling a more realistic description of material flow under NECAP conditions. A further modification of the flow line function was made to model the deformation

field in T-ECAP [46], where the exit channel is open in both the left and right directions, resulting in a T-shape die configuration. The modified flow function is expressed as:

$$f = \left(1 - \frac{qx}{p}\right)^n + m\left(1 - \frac{ky}{c}\right)^n = \left(1 - \frac{qx_0}{p}\right)^n \tag{26}$$

where the additional parameter q controls the termination position of the flow line relative to the intersection zone of the channels. When $q = 1$, the flow line finishes exactly at the end part of the intersection zone of two channels, recovering Eq. (25). For $q < 1$ and $q > 1$, the flow line terminates after and before the end part of the intersection zone, respectively. The new parameter enables more accurate determination of the flow line exit point with respect to the experiment observations, even if the end point is outside the intersection zone. In addition to these developments, two generalized extensions of Toth's flow line model were proposed to describe plastic deformation in ECAP with arbitrary die angles [72, 73].

1.1.4. Friction-Assisted Lateral Extrusion Process (FALEP)

Nakamura et al. [74, 75] developed the first version of the friction-assisted extrusion technique in 1992. However, since then, this technique received limited attention and has been nearly forgotten. In 2021, Vu et al. [76] independently reintroduced the same deformation concept and termed it the friction-assisted lateral extrusion process (FALEP). The development of FALEP was motivated by the technical limitations observed in NECAP for large extrusion ratios. From a processing perspective, NECAP can be considered the closest technique to FALEP. However, compared to NECAP, FALEP benefits from a unique advantage: an additional moving tool (driving punch) laid horizontally at the bottom of the sample that moves in the same direction as the material flow and assists the extrusion process. Fig. 7 presents a schematic illustration of the FALEP technique. While the normal punch provides compression pressure to maintain a non-sliding condition at the interface between the driving punch and the material, the driving punch itself facilitates the material deformation by applying a friction force. In contrast to other SPD processes, such as ECAP and NECAP, in which the friction force acts against the material flow, the friction force in FALEP is applied in the same direction as the material flow and therefore plays a beneficial role in the deformation process. For this reason, the technique is referred to as friction-assisted. A recent study on the mechanics of FALEP revealed that this technique requires about five times lower extrusion force than NECAP at the same extrusion ratio, owing to an additional shear stress component provided by the driving punch [77]. The unique design of FALEP allows imposing extremely large shear strains, exceeding 100, on

initial bulk or powder materials to produce UFG sheet products in a single operation step at room temperature, making it a highly promising SPD technique for industrial applications.

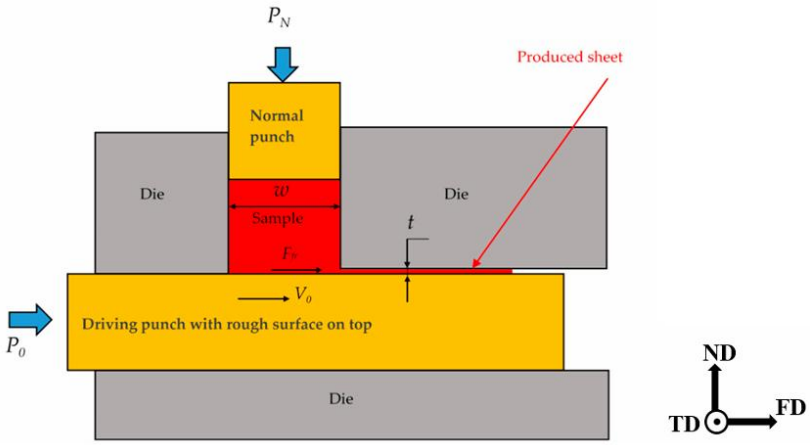

Fig. 7. Schematic of the friction-assisted lateral extrusion process (FALEP) [76].

Vu et al. [76] conducted FALEP experiments on a commercially pure Al-1050 alloy using ingoing and exit channel sizes of 20 and 1 mm, respectively, corresponding to an extrusion ratio of 20. As shown in Fig 8, after FALEP, the initial microstructure was extremely refined, with an average grain size reduced from 100 μm to near the minimum attainable grain size (steady-state) of 600 nm, achieved through a single processing step. Meanwhile, relatively equiaxed grains with a homogeneous distribution across the sheet thickness were achieved at this extrusion ratio.

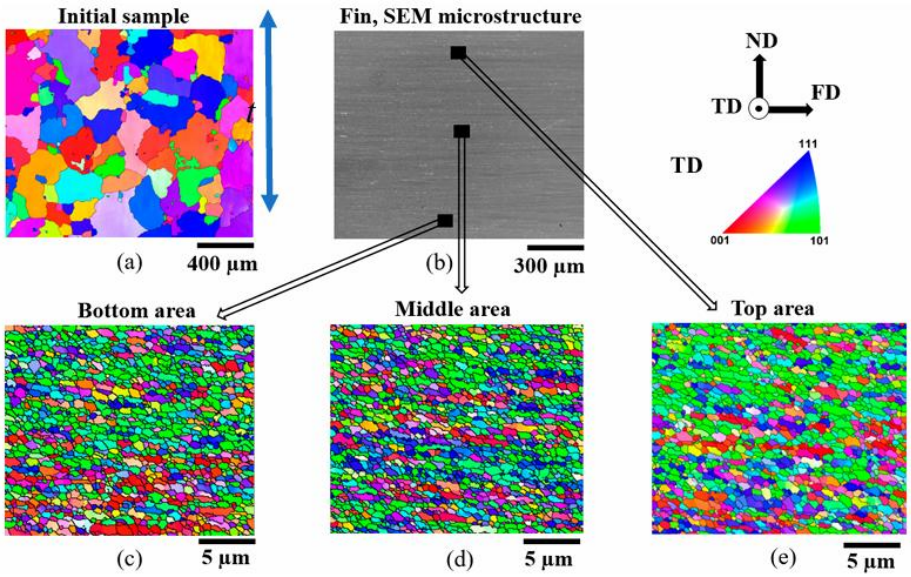

Fig 8. **(a)** EBSD microstructure of the initial sample. **(b)** SEM microstructure across the thickness of the produced fin. **(c–e)** EBSD microstructures of the bottom, middle, and top regions of the Al-1050 produced fin, respectively [76].

An analysis of the texture of the FALEP sample can indirectly confirm that the dominant deformation mode is simple shear. As shown in Fig. 9, a typical shear texture was achieved, with the shear plane (SP) oriented 3° with respect to the FALEP direction (FD), which agrees with the theoretical orientation of the ideal shear plane in NECAP for this die geometry (2.86°). Among the ideal shear components, the C component exhibited the highest intensity. However, the second-most relevant component was the 45° rotated-cube orientation, which is not an ideal shear component. The unique features of the rotated-cube fiber during shear deformation and its influences on microstructural evolution will be discussed in detail in the second part of this thesis.

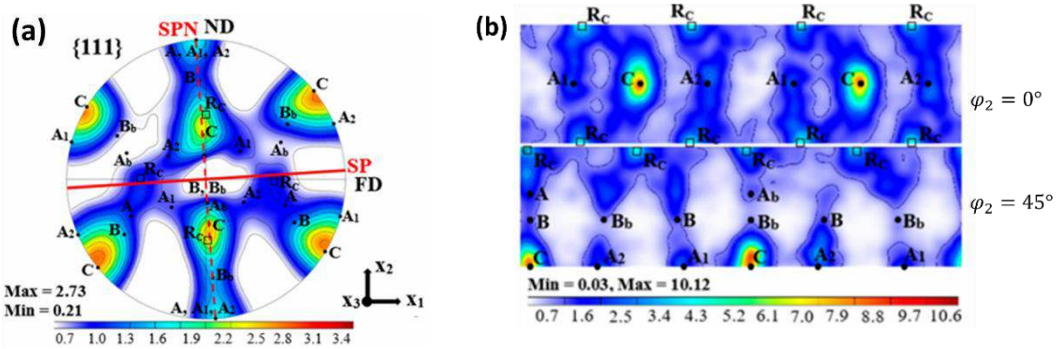

Fig. 9. **(a)** Pole figure, and **(b)** ODF sections of the Al-1050 sample after FALEP processing [76].

Pariyar et al. [78] investigated the potential of the FALEP technique for producing sheet metal from initial powder material. They reported that a fully dense sheet product was successfully fabricated by FALEP at an extrusion ratio of 13.3 in a single processing step at room temperature. Fig. 10a shows the resulting microstructure of the powder-FALEP specimen. A UFG microstructure with a number-weighted average grain size of 500 nm was obtained. Furthermore, the high fraction of high-angle grain boundaries (HAGBs) indicates that the large shear strain imposed during FALEP promoted continuous dynamic recrystallization (CDRX) at room temperature (Fig. 10b).

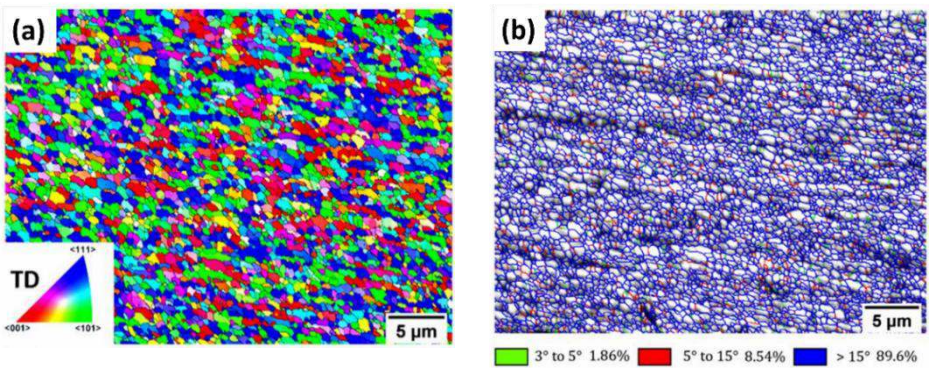

Fig. 10. **(a)** IPF map of powder-FALEP sample projected on the TD plane. **(b)** The corresponding grain boundary map [78].

Another potential application of the FALEP technique is the fabrication of multilayer sheet metals and composites. Adams et al. [79] employed FALEP to produce multilayer sheets composed of five alternating layers of dissimilar aluminum alloys, AA1050 and AA5052. Fig. 11a shows the configuration of the specimen within the FALEP die before and after extrusion. Electron back scattering diffraction (EBSD) analysis revealed that grain refinement was pronounced in both alloys (Fig. 11b). A uniform microstructure with an average area-weighted grain size of 0.75 µm was obtained in AA1050 layer. The AA5052 layer, however, exhibited a bimodal grain size distribution with an average grain size of 1.14 µm. Considering that AA5052 is a harder material with a higher content of alloying elements, a smaller grain size than that of AA1050 would be expected at the same strain level. The opposite trend observed in this study suggests that the plastic deformation was different between the two layers at the given measurement position. Furthermore, the initial thicknesses of the layers were identical before FALEP, whereas their final thicknesses after processing were different in the composite material, which confirms that the strain distribution was not uniform.

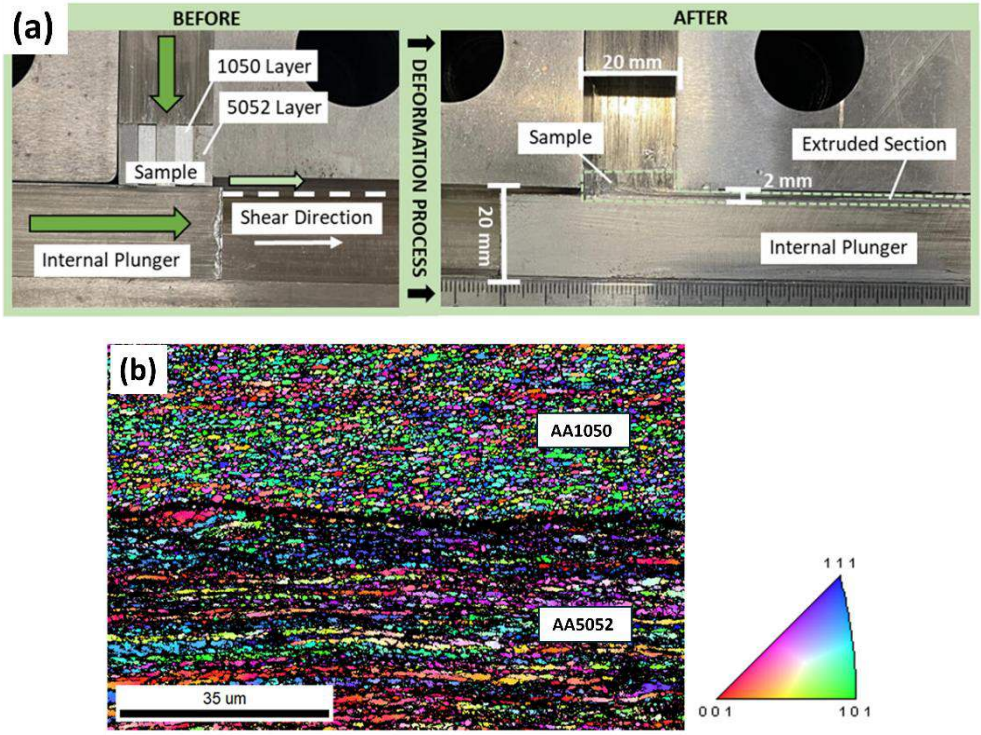

Fig. 11. **(a)** The configuration of the multilayer specimen within the FALEP die before and after extrusion. **(b)** EBSD image after FALEP processing showing different grain sizes between the two layers [79].

Due to the novelty of the FALEP technique and the limited number of available studies, several aspects of this processing technique remain poorly understood, particularly the deformation mode and material flow characteristics. Accordingly, the primary objective of the present study is to evaluate deformation behavior during FALEP processing. To this end, a new analytical

flow line model is proposed based on experimental observations to describe the deformation mode and to estimate the equivalent strain imposed during FALEP. Using the new flow line model and polycrystal plasticity approaches, texture evolution during FALEP processing is simulated. The proposed model is indirectly validated through quantitative comparisons between the measured and simulated textures. In the following sections, the experimental procedures and results, the principles of the new modelling approach, and the texture simulation outcomes are presented and discussed in detail.

1.2. Experimental Procedures and Results

1.2.1. Flow Line Experiments

FALEP experiments were carried out on commercially pure Al-1050 alloy at room temperature using the FALEP facility at the LEM3 laboratory (Metz, France). In total, nine FALEP experiments were performed with a constant ingoing channel cross-section of 20 × 20 mm^2. The exit channel size, however, varied between 4.3 and 1.1 mm, corresponds to extrusion ratios p/c ranging from 4.6 to 18. In all experiments, the normal punch applied a constant pressure of P_{ND} = 160 MPa (6.4 tons), while the driving punch was operated at a constant displacement rate of 3 mm/s.

To directly investigate the material flow kinematics during FALEP, each sample was split into two identical parts along the middle of their longitudinal axis prior to deformation. Trajectory lines were then engraved longitudinally only on the surface of one part using either laser marking or CNC machining, depending on the specimen. The two parts were inserted into the FALEP die such that the marked surface was positioned at the internal interface between the two parts, thereby the effect of friction between the marked surface and the die surface was avoided. An example of the FALEP die configuration is presented in Fig. 12a. The marked part of all samples after FALEP processing for the different applied extrusion ratios (p/c) are shown in Fig. 12b.

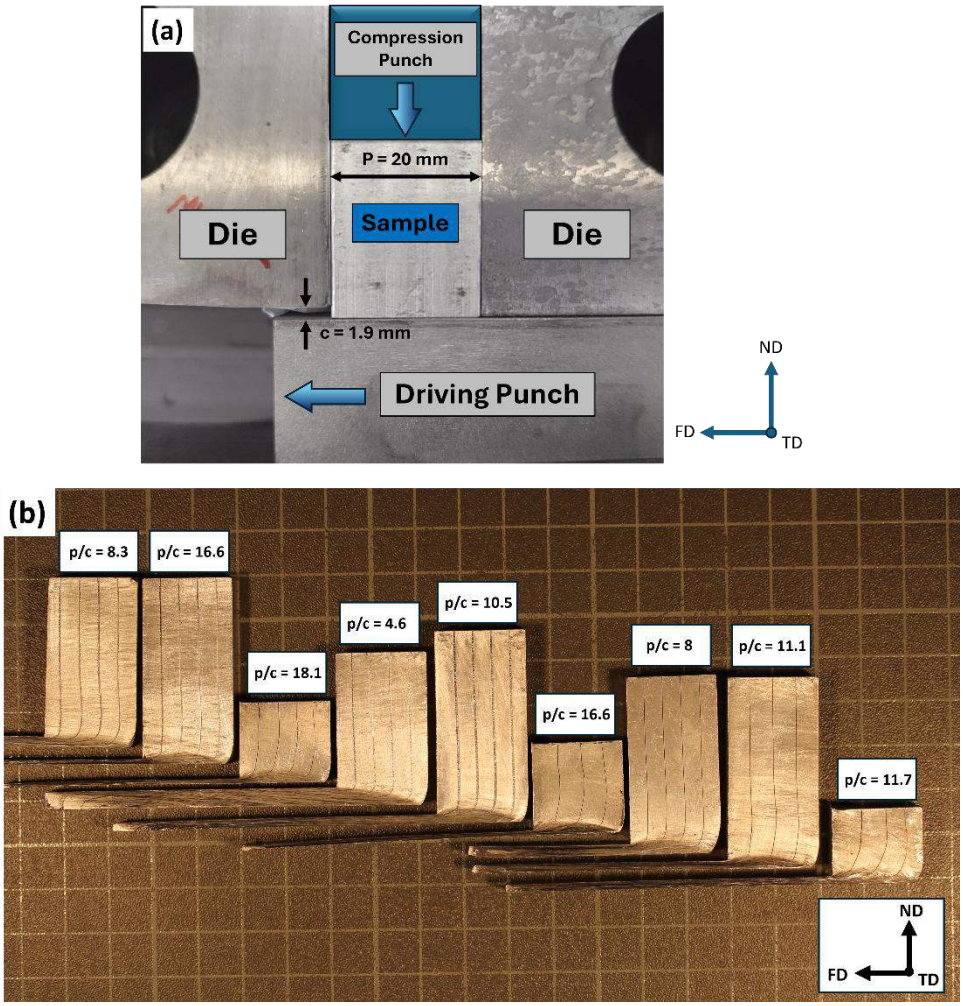

Fig. 12. **(a)** Photo of the FALEP die containing the Al-1050 sample before deformation. **(b)** The marked surface of the samples after FALEP processing at different extrusion ratios (FD = FALEP direction, ND = normal direction, TD = transverse direction).

An unexpected curvature of the flow lines was observed in some specimens, occurring within the ingoing channel region and at locations far from the intersection zone of the two channels. An example of this phenomenon is shown in Fig. 13. Because two separate parts were used for each experiment, the identical dimensions of these parts are critical to ensure uniform deformation of the flow lines. Therefore, such flow line curvature can be attributed to slight dimensional mismatches between the two sample parts, as the sample preparation was done manually. Due to the very large shear strain and the small size of the exit channel in FALEP, a slight variation between the dimensions of the two parts can negatively affect the deformation uniformity. Moreover, the total size of the assembled parts is also important. A small gap in the ingoing channel violates the full constraint condition, allowing material to flow into it under the high imposed pressure, leading to deviations in the flow lines and alternations in the friction forces on different surfaces. This indicates the crucial role of proper sample preparation in flow line analysis for a large deformation technique, like FALEP.

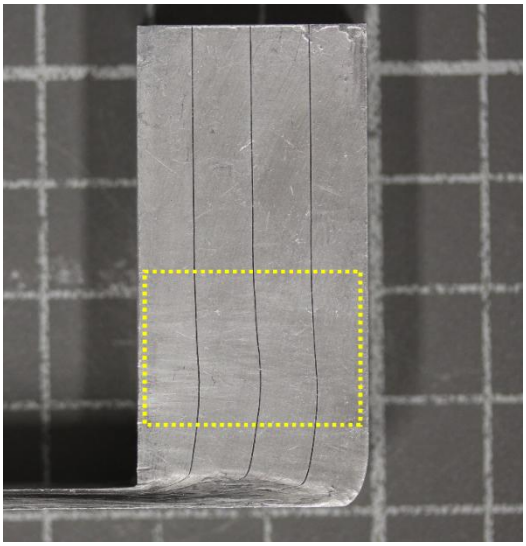

Fig. 13. Unexpected flow line curving far from the deformation zone.

To minimize such undesirable deviations in the flow lines, more precise sample preparation was carried out. Fig. 14 shows the deformation behavior of the flow lines for two FALEP samples processed with extrusion ratios of 4.6 and 10.5. For the specimen deformed with the lower extrusion ratio (Fig. 14a), the flow lines exhibit a uniform and smooth curvature, with the deformation zone confined to the intersection region of the two channels. A similar flow line deformation behavior has been reported for ECAP processes [60, 67], T-ECAP [46], as well as NECAP performed at a relatively low extrusion ratio of 2 [40].

In contrast, when the extrusion ratio increases to 10.5, the trajectory lines display more complex deformation behavior, as illustrated in Fig. 14b. In this case, the deformation is no longer restricted to the intersection zone of the two channels and extends beyond it. Such complex deformation behavior has not been reported in previous studies on channel angular extrusion processes. Given that FALEP is designed to impose large plastic strains within a single processing step, it is crucial to investigate the observed complex deformation behavior for the large strain cases. Consequently, the FALEP sample processed with an extrusion ratio of 10.5 was selected for detailed analysis in the present study.

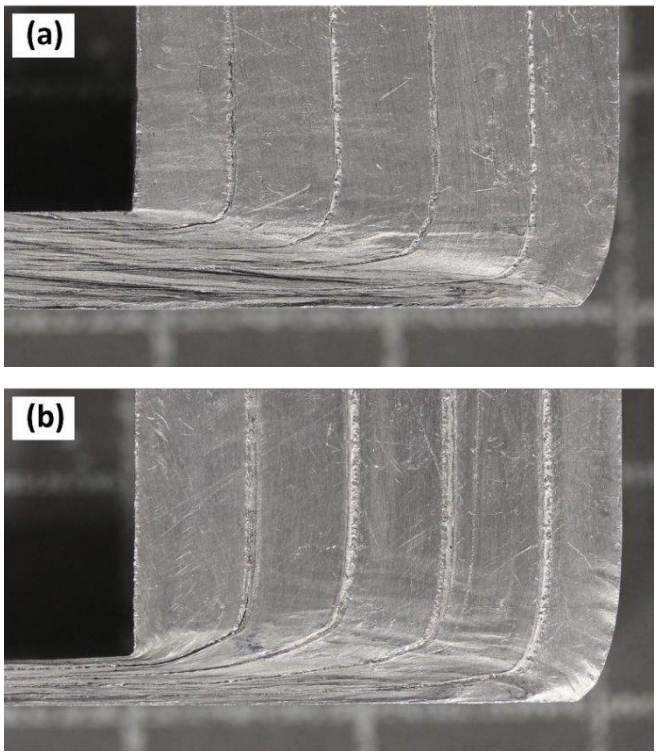

Fig. 14. The deformation behavior of the flow lines for **(a)** extrusion ratio of 4.6 showing uniform curving, **(b)** extrusion ratio of 10.5 showing complex deformation behavior.

1.2.2. Microstructure and Texture of Al-FALEP Sample

The microstructure and crystallographic texture of the aluminum sample after FALEP processing at the extrusion ratio of 10.5 were characterized by the EBSD technique using a JEOL JSM-6500F field-emission gun scanning electron microscope. Two regions on the lateral surface of the produced sheet (FD-ND plane) were examined, one located near the top surface (Line1) and the other near the bottom surface (Line4), as shown in Fig. 15. The EBSD data were analyzed using the ATEX software [80]. The initial microstructure and texture of the material were investigated using optical microscopy and XRD (Bruker D8 Advance Diffractometer), respectively. Furthermore, the texture of the bottom surface (Line4) was also measured by XRD on the FD-TD surface to obtain good statistics.

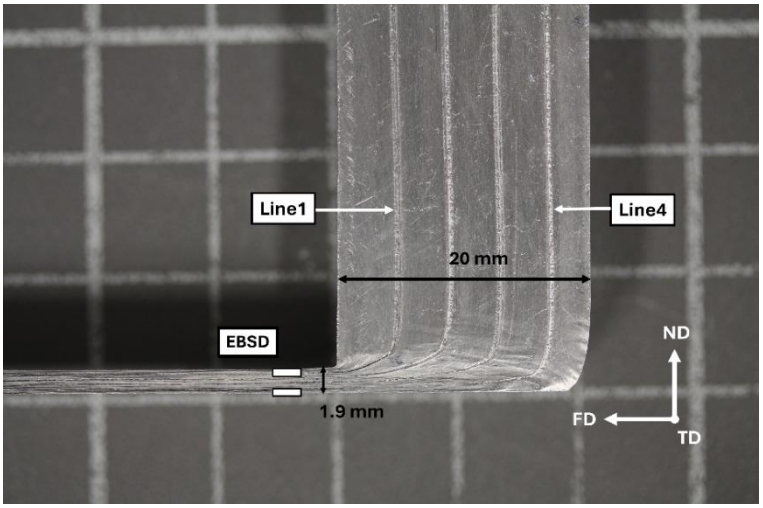

Fig. 15. The marked part of the Al-1050 sample after FALEP processing at an extrusion ratio of 10.5.

The initial microstructure of the Al-1050 sample before the FALEP process is shown in Fig. 16a. The microstructure consisted of coarse grains with an average grain size of approximately 100 µm. During FALEP processing, grain refinement occurred intensively along both the Line1 and Line4 regions. At the end of Line1, a homogeneous and equiaxed grain structure with an average area-weighted grain size of about 720 nm was obtained (Fig. 16b). However, the average grain size at the end of Line4 is significantly larger, reaching approximately 4.2 µm, and the microstructure contains a fraction of relatively coarse grains that are not fully recrystallized, as shown in Fig. 16c.

These results clearly indicate the development of a heterogeneous microstructure across the thickness of the produced sheet, with a finer microstructure obtained near the top surface. However, in a previous study on FALEP processing of Al-1050 alloy, a very homogeneous grain size and morphology was reported [76]. The difference between the two results can be attributed to differences in the imposed shear strain. In the previous study, the exit channel size was 1 mm, corresponding to a higher extrusion ratio of 20, whereas in the present study, the larger exit channel size (1.9 mm) resulted in a lower extrusion ratio of 10.5. These results demonstrate that the p/c ratio in the FALEP process not only affects the final microstructure in terms of grain size and texture but also plays a key role in determining the degree of microstructural homogeneity across the sheet thickness.

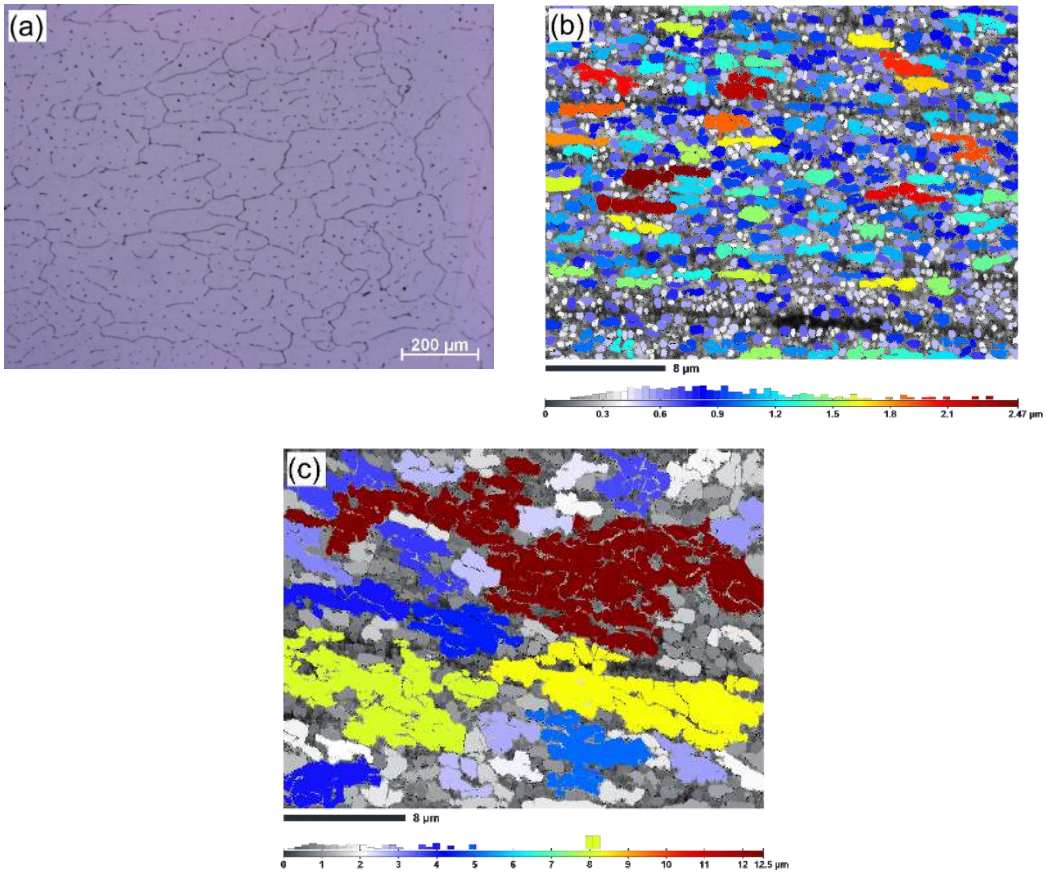

Fig. 16. **(a)** Optical microscopy image of the initial Al-1050 sample microstructure. SEM micrographs of the sample after the FALEP process **(b)** near Line1, and **(c)** near Line4. The grains are colored according to the grain size scale.

Fig. 17 shows the next-neighbor grain disorientation distribution for Line1 and Line4 regions, together with the random distribution (Mackenzie). The percentage fraction of high-angle grain boundaries (HAGB, larger than 15°) was determined by integrating the disorientation distributions. This fraction significantly varies between the Line1 and Line4 regions. For Line1, the HAGB fraction reaches nearly 58%, whereas for Line4, it is limited to only 3%. The considerably higher fraction of HAGBs in Line1 indicates that a larger plastic strain was accumulated in this region compared to Line4. Consequently, CDRX was more pronounced near Line1, which is consistent with the observed UFG and equiaxed microstructure in this region.

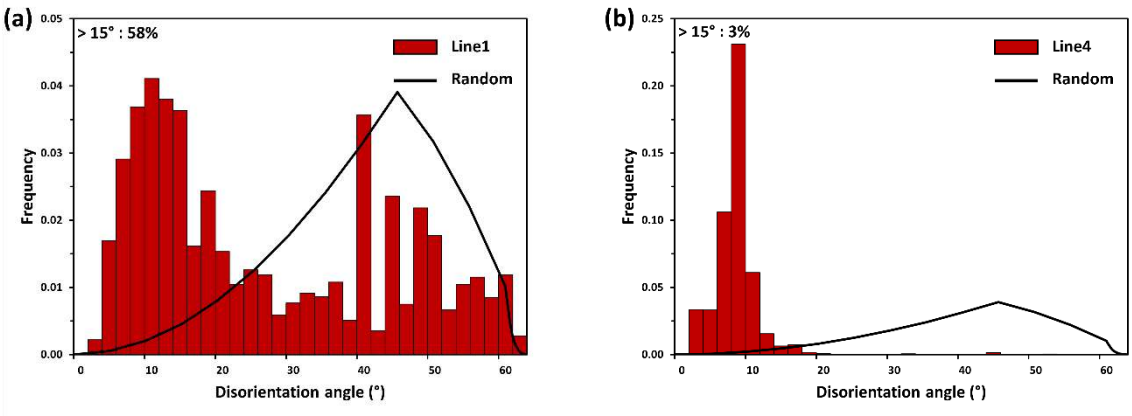

Fig. 17. Next-neighbor grain disorientation distributions for **(a)** Line1, and **(b)** Line4 (bin size = 2°). The black line shows the random Mackenzie distribution.

The crystallographic texture of the initial Al-1050 sample is shown in Fig. 18a, where a rotated cube-type texture is observed. After the FALEP process, the (111) pole figures of Line1 (Fig. 18b) and Line4 (Fig. 18c) show a simple shear type of texture; however, there are notable differences between them. As seen in the pole figures, the strongest component in the Line1 region is the C ({100}<110>) component, whereas the dominant orientation in Line4 is the A_1 ($\{\bar{1}\,\bar{1}\,1\}$<112>) component. In this notation, the first Miller indices refer to the shear plane normal, while the second indices correspond to the shear direction. These directions were identified based on the expected orientation of the texture corresponding to the simple shear model of angular extrusion, in which the deformation is assumed to occur by simple shear along the intersection plane of the two channels. For the present FALEP geometry, this theoretical plane is oriented at an angle of $arctg(p/c) = 5.42°$ with respect to FD. However, as shown in Fig. 18, both experimental textures are rotated by considerably larger angles, approximately 16° for Line1 and 14° for Line4.

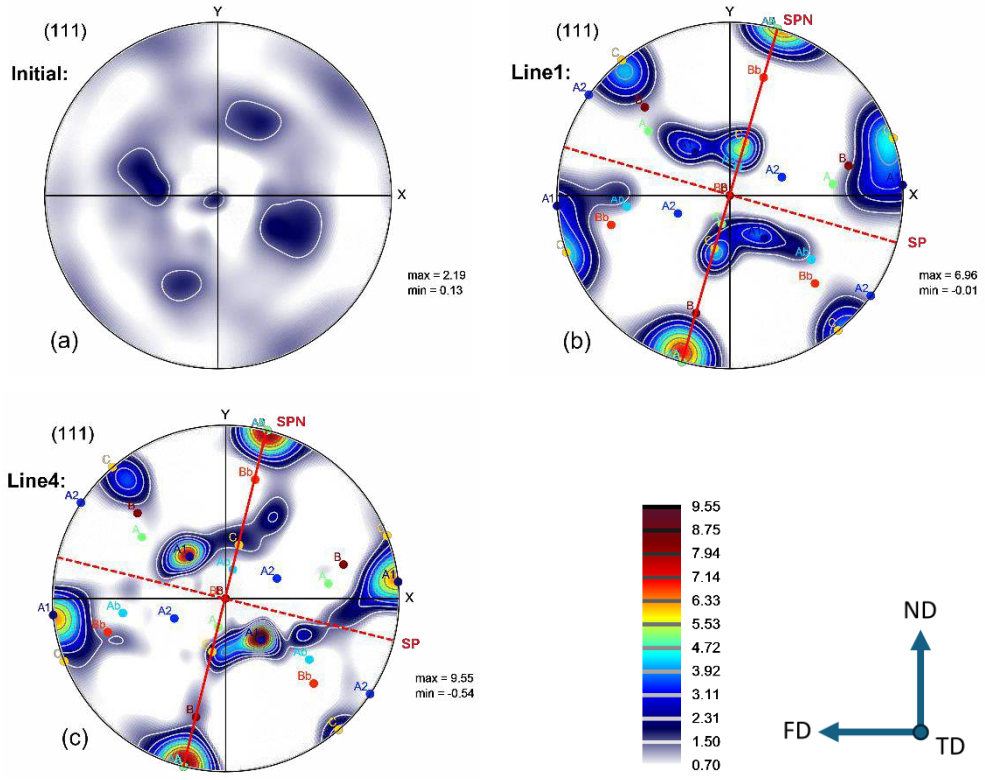

Fig. 18. **(a)** The measured crystallographic texture of the initial sample. The obtained experimental textures after FALEP processing for **(b)** Line1 and **(c)** Line4. The position of the ideal shear components (symbols) is also shown. SP indicates the apparent shear plane, and SPN is the corresponding shear plane normal.

The difference between two different textures can be quantitatively assessed using the direct texture correlation index, which is available in the ATEX software. This index is defined as:

$$D = \frac{\int_g f_A(g) f_B(g) dg^2}{\sqrt{\int_g f_A^2(g) dg^2 . \int_g f_B^2(g) dg^2}} \tag{27}$$

where $f_A(g)$ and $f_B(g)$ represent the orientation distribution functions (ODFs) of the two textures being compared, and g denotes the orientation vector defined by three Euler angles. The value of D ranges between 0 and 1, with $D = 1$ corresponding to two identical textures. In the present study, D is expressed as a percentage, such that 100% corresponds to $D = 1$.

The direct correlation index between the measured textures of Line1 and Line4 was 66.8%, indicating a remarkable difference between the two textures. Together with the microstructural observations, this result clearly demonstrates that deformation during FALEP at this extrusion ratio was non-uniform across the sheet thickness, leading to the development of a gradient

microstructure. The main reason for this non-uniformity must be the differences in the deformation paths, which will be discussed in the next section.

1.3. Theoretical Foundations

1.3.1. Flow Line Kinematics

A closer inspection of the trajectory lines reveals that the deformation zone extends significantly above the intersection zone of the two channels, with its upper boundary outlined by the top white broken line in Fig. 19. Notably, sharp variations are observed in the shape of the flow lines, indicating non-uniform kinematic behavior along the deformation path. Based on these observations, three distinct deformation stages can be identified. In the first stage, the material element undergoes a simple shear deformation before entering the intersection zone, where a pronounced change in flow line direction occurs. It should be noted that this shear zone has a finite, variable thickness. Within this region, uniform simple shear is achievable. A similar approach has previously been proposed for ECAP in Ref. [69] and is adopted here for the FALEP process as well. In fact, the analysis presented in Ref. [69] demonstrated that uniform simple shear is attainable in ECAP even when the flow lines are rounded and the deformation zone is relatively large. It is therefore assumed that a similar condition applies to FALEP.

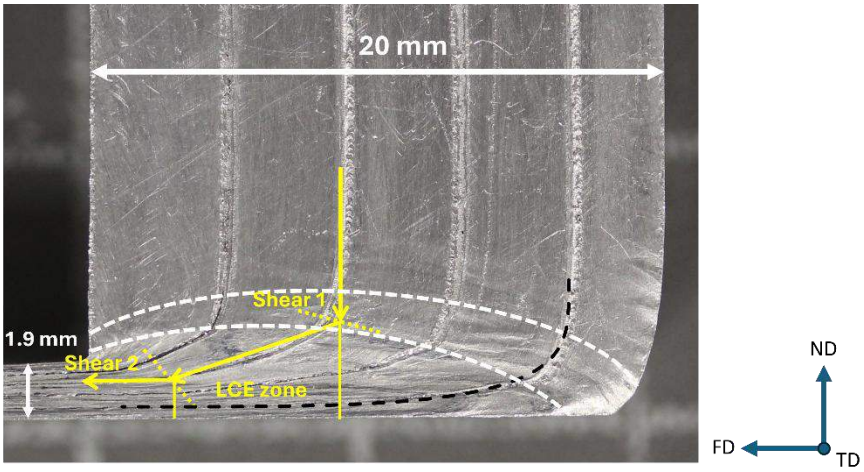

Fig. 19. The three deformation stages along the flow lines (Shear1, linear converging extrusion (LCE) zone, Shear2). The black dashed line represents the fitted flow line obtained from Eq. (28). The zone between the two white dashed lines shows the first shear zone.

Following the first shear deformation, the material element enters a second deformation region in which the trajectory line becomes nearly straight and converging. Finally, a second shear occurs near the exit channel, aligning the line parallel to the exit direction. The relative contribution and sharpness of these three deformation stages become more pronounced by moving from the outer corner (Line4) to the inner corner (Line1).

The second stage, referred to here as linear converging extrusion (LCE), has not been reported in previous studies on equal or non-equal channel angular pressing [40, 46, 73]. Nevertheless, this deformation stage can considerably contribute to the total deformation and the resulting texture evolution within the sample. In the following section, an analytical model is proposed to describe the deformation using the velocity gradient tensor within the LCE zone of the flow line. For the two simple shear stages, the velocity gradient tensor remains constant and can be directly determined from the orientation of the shear plane.

Considering that the three-stage deformation was less pronounced for Line4, it was possible to fit the experimental flow lines with the flow line function (Eq. (26)) proposed in Ref. [46]. In the present study, the sample was extruded in the -x direction. For this case, Eq. (26) can be rewritten as:

$$f = \left(1 - \frac{q(x-p)}{p}\right)^n + m\left(1 - \frac{ky}{c}\right)^n = \left(1 - \frac{q(x_0-p)}{p}\right)^n \tag{28}$$

The fitting was relatively successful for Line4, as shown with a black dashed line in Fig. 19, but was not reasonable for the others. It was obtained using the following parameters: x_0 = 16.75 mm, n = 4, m = 0.7, k = 0.4, and q = 1. The corresponding texture simulation will be presented in Section 1.4.

1.3.2. The Three-Stage Flow Line Model

Fig. 20 presents a schematic illustration of the flow lines, highlighting the three deformation stages and their associated geometrical parameters. For the two simple shear stages, the velocity gradient tensor expressed in the laboratory reference system (x-y-z) is defined as:

$$\underline{\underline{\boldsymbol{L}}} = \dot{\gamma}\begin{pmatrix} sin\,\alpha \cdot cos\,\alpha & -cos^2\alpha & 0 \\ sin^2\alpha & -sin\,\alpha \cdot cos\,\alpha & 0 \\ 0 & 0 & 0 \end{pmatrix} \tag{29}$$

where $\alpha = \alpha_1$ and $\alpha = \alpha_2$ correspond to the first and second simple shear stages, respectively. The magnitudes of the shear strains, both of which are positive, can be obtained from Eq. (20) and are given by:

$$\gamma_1 = ctg(90° - \alpha_1) + ctg(\alpha_1 + \beta) \tag{30a}$$

$$\gamma_2 = ctg(\alpha_2) + ctg(180° - \alpha_2 - \beta) \tag{30b}$$

The polycrystal plasticity code requires the velocity gradient tensor as input and achieves the prescribed finite strain through small increments. In the present simulations, 100 increments

were applied for each of the two simple shear stages, resulting in shear increments of $d\gamma = \gamma/100$. The corresponding time increment was calculated as $dt = d\gamma/\dot{\gamma}$. A shear strain rate of $\dot{\gamma} = 1.0/s$ was employed in all simulations. Note that the value of $\dot{\gamma}$ does not affect the texture evolution, since the latter is independent of the strain rate.

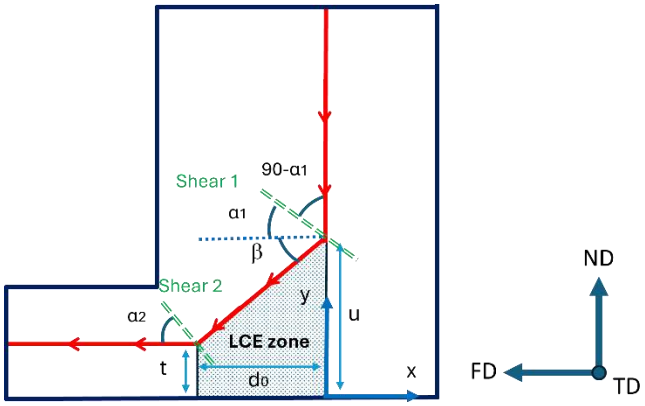

Fig. 20. Schematic view of the proposed three-stage flow line model for FALEP deformation.

Fig. 21 displays a schematic representation of the LCE section of the flow line, in which linear convergent extrusion takes place. In this model, the velocity field is assumed to be radial and directed toward point *D*. The incoming velocity is denoted by v_0. The die length is d_0, while its prolongation projected onto the x-axis is denoted by d. Both quantities are dimensional parameters of the die geometry and therefore take positive values.

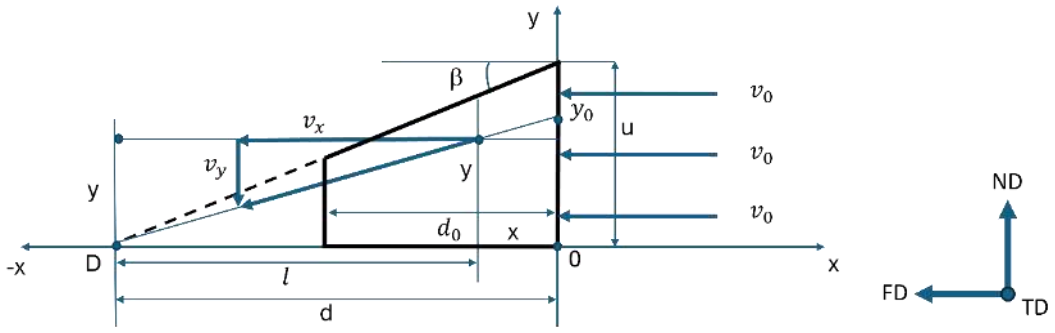

Fig. 21. Schematic of the LCE zone of the flow line (the thick black lines represent the LCE zone of the deformation field).

The equation describing a flow line is as follows:

$$y = y_0 \cdot \left(1 + \frac{x}{d}\right) \tag{31}$$

From this equation, a relatively simple flow function can be established to describe the material flow, following an approach commonly used in fluid mechanics:

$$f(x,y) = \frac{y}{\left(1+\frac{x}{d}\right)} = y_0 \tag{32}$$

Applying the incompressibility condition from two-dimensional fluid mechanics, an admissible velocity field corresponding to the flow function can be derived from the following partial derivatives:

$$v_x = \lambda \frac{\partial f(x,y)}{\partial y} \tag{33a}$$

$$v_y = -\lambda \frac{\partial f(x,y)}{\partial x} \tag{33b}$$

The value of λ is determined from the boundary condition that the entering velocity at $x = 0$ is known: $v_x = -|v_0|$. This leads to $\lambda = -|v_0|$. The velocity field components are therefore given by:

$$v_x = -\frac{|v_0|}{\left(1+\frac{x}{d}\right)} \tag{34a}$$

$$v_y = -\frac{|v_0| \cdot y}{d \cdot \left(1+\frac{x}{d}\right)^2} \tag{34b}$$

The velocity gradient components are obtained by further partial derivation of the velocity field components. Among them, only three components are non-zero:

$$L_{xx} = \frac{\partial v_x}{\partial x} = \frac{|v_0|}{d \cdot \left(1+\frac{x}{d}\right)^2} \tag{35a}$$

$$L_{yy} = \frac{\partial v_y}{\partial y} = -\frac{|v_0|}{d \cdot \left(1+\frac{x}{d}\right)^2} \tag{35b}$$

$$L_{yx} = \frac{\partial v_y}{\partial x} = \frac{2 \cdot |v_0| \cdot y_0}{d^2 \cdot \left(1+\frac{x}{d}\right)^2} \tag{35c}$$

For the normal components of the velocity gradient, $L_{yy} = -L_{xx}$, which is consistent with the volume constancy characteristic of incompressible flow.

The resulting velocity gradient tensor corresponds to a plane strain deformation mode:

$$L = \begin{pmatrix} L_{xx} & 0 & 0 \\ L_{yx} & L_{yy} & 0 \\ 0 & 0 & 0 \end{pmatrix} \tag{36}$$

The strain rate tensor is given by:

$$\dot{\varepsilon} = \begin{pmatrix} L_{xx} & L_{yx}/2 & 0 \\ L_{yx}/2 & L_{yy} & 0 \\ 0 & 0 & 0 \end{pmatrix} \tag{37}$$

The equivalent von Mises strain rate ($\dot{\bar{\varepsilon}}$) can be obtained as:

$$\dot{\bar{\varepsilon}} = |v_0| \cdot \frac{2d}{\sqrt{3} \cdot (d+x)^2} \sqrt{1 + \frac{{y_0}^2}{d^2}} \tag{38}$$

The total equivalent strain is then calculated by integration of $\dot{\bar{\varepsilon}}$ along the flow line:

$$\bar{\varepsilon} = \frac{2}{\sqrt{3}} \cdot \left(ln \frac{d}{d - d_0} \right) \cdot \sqrt{1 + \frac{{y_0}^2}{d^2}} \tag{39}$$

The parameter d can be expressed using the entry position of the flow line u, according to the geometrical relation $d = \frac{u}{tg\beta}$. Substituting this expression into Eq. (39) leads to:

$$\bar{\varepsilon} = \frac{2}{\sqrt{3}} \cdot \left(ln \frac{u}{u - d_0 tg\beta} \right) \cdot \sqrt{1 + \frac{{y_0}^2 \cdot (tg\beta)^2}{u^2}} \tag{40}$$

For implementation of the developed velocity gradient tensor in the polycrystal plasticity code, the deformation along the flow line was discretized into 100 incremental steps. The time increment was determined by dividing the total time by 100: $dt = T/100$. The total time T was obtained by integrating the v_x component of the velocity field along the flow line, which leads to:

$$T = \frac{d_0}{v_0} \left(1 - \frac{d_0 tg\beta}{2u} \right) \tag{41}$$

Using the expressions for the velocity components given in Eqs. (34a) and (34b), the new x and y coordinates of the material point were then calculated after each time increment dt. Once the updated position along the flow line was known, the non-zero components of the velocity gradient tensor were evaluated using Eqs. (35a-c) and subsequently introduced into the polycrystal plasticity code.

The proposed model can be directly applied to the FALEP die geometry, as schematically illustrated in Fig. 20. Each trajectory line is assumed to be located at the edge of the LCE zone ($y_0 = u$). The positions of the two shear planes and the corresponding shear angles are also indicated in Fig. 20, where α_1 and α_2 are model parameters, while the angle β is fixed by the geometry of LCE zone. The imposed velocity gradient is incrementally calculated for a material element as it progresses through the three deformation stages: shear1, LCE, and shear2. The geometrical input parameters of the model were measured directly from the experimentally observed flow lines for Line1 and Line4. These parameters include the LCE angle (β), the initial y coordinate on the flow line (u), and length of the LCE zone (d_0). The only parameters requiring adjustment were α_1 and α_2, which correspond to the angles of the first and the second shear planes with respect to the x-axis. The selected parameters are summarized in Table 2.

Table 2. Data corresponding to flow lines. Data in italics are parameters of modeling.

	Line1	Line4
Extrusion speed (v_0) mm/s	1	1
LCE zone angle (β)	23°	4°
Length of the LCE deformation zone (d_0) mm	3.5	1
Starting y coordinate on the flow line (u) mm	3.12	0.53
Angle between the first shear plane and the x-axis (α_1)	40°	15°
Angle between the second shear plane and the x-axis (α_2)	15°	90°
First shear value	1.34	3.16
Second shear value	2.45	0.07
Equivalent von Mises strains (shear1, LCE, shear2)	0.78, 0.79, 1.41	1.83, 0.16, 0.04
Total Equivalent von Mises strain	2.98	2.03

1.4. Polycrystal Texture Simulations

Texture simulations were carried out using the viscoplastic self-consistent approach (VPSC, version 5, [13]) in a tuned version, in which a scalar parameter ($1/\alpha$ in the VPSC formulation) was incorporated into the interaction equation of the VPSC model. Several values of the $1/\alpha$ parameter were examined, including the limiting case of $1/\alpha = 0$, which corresponds to the classical Taylor assumption of uniform deformation. For clarity and ease of comparison, this limiting case ($1/\alpha = 0$) is hereafter referred to as the Taylor model. In all simulations, the 12 $\{\bar{1}11\}$<110> slip systems were employed with a slip-viscosity exponent of 7 ($1/m = 7$). To assess the effect of the initial texture, two different initial orientation sets were considered: 5000 randomly distributed orientations and 5000 orientations discretized from the

experimentally measured initial texture using the ATEX software. The variable velocity gradient derived from the new flow line model was used as input to the polycrystal model to compute the lattice rotations and, consequently, the texture evolution. Parameters listed in Table 2 were employed to calculate the imposed velocity gradients for Line1 and Line4. Meanwhile, texture simulations were also performed using the classical simple shear model, as well as the flow line model proposed in Ref. [46] (Eq. (28)) for comparison with the new flow line model.

Fig. 22 presents the simulated textures obtained using the classical simple shear model of angular extrusion. The simulations were performed within the Taylor framework, considering both an initially random texture and an initial texture discretized from the experimental measurements. The imposed strain mode was simple shear acting on the theoretical shear plane, which is inclined at 5.43° with respect to FD. The applied shear strain was 10.62, corresponding to the simple shear deformation assumed for NECAP conditions (Eq. (21)). Under the simple shear model, the resulting texture remains constant across all flow lines. Consequently, the simulated texture should be compared to both Line1 and Line4. Fig. 22 reveals two major differences between the simulated and experimental textures: first, the simulated textures exhibit significantly different orientations from the measured ones; second, the simulated textures are considerably weaker in intensity. When the initial cube-type texture is used in the simulation, the resulting texture contains an additional fiber, which appears as a circle in the {111} pole figure (as indicated by the broken line circle in Fig. 22b). This fiber is already present in the initial texture. Indeed, a grain with an exact cube orientation rotates predominantly via the rigid body rotation during simple shear, since its plastic spin is zero, resulting in the observed circle in the pole figure. Quantitative comparison with the experimental textures confirms that the agreement between simulation and experiment is poor. Using the initial random texture, the direct correlation indices were only 61.3% and 24.6% for Line1 and Line4, respectively. No improvement was obtained when the initial discretized texture was employed, for which the correlation indices were 53.5% for Line1 and 24.3% for Line4. Moreover, the simple shear model assumes a uniform shear value and deformation mode along the entire shear plane. As a result, this approach is unable to account for the observed heterogeneity in deformation and texture across the sheet thickness. Further simulations performed using different interaction parameter values in the VPSC polycrystal code did not lead to any improvement in the texture simulation results. Therefore, the simple shear model

failed to properly reproduce the experimental textures for either Line1 or Line4 at this extrusion ratio.

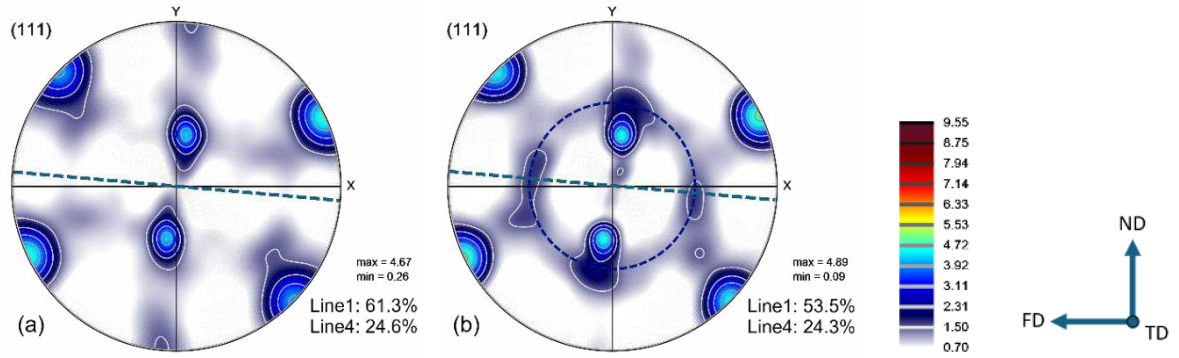

Fig. 22. Pole figures of the simulated textures using the simple shear model for **(a)** initial random texture and **(b)** initial measured texture. The correlation indices between simulation and experiment are written next to the pole figures in % for both Line1 and Line 4. The broken line represents the orientation of the intersection plane of the FALEP channels.

Fig. 23 presents the texture simulation results for Line1 using the proposed flow line model, considering three different cases: (i) the Taylor polycrystal model ($1/\alpha = 0$) with an initially random texture, (ii) the Taylor model with the initially measured and discretized texture, (iii) the self-consistent approach with $1/\alpha = 2.5$ using an initial random texture. The geometrical parameters of the flow line are presented in Table 2. Interestingly, the best agreement with the experimental texture was achieved using the Taylor model ($1/\alpha = 0$) with the initial random texture (Fig. 23a). In this case, almost all major texture components observed in the measured texture (Fig. 18b) were faithfully reproduced in the simulation. The direct correlation index between simulated and measured texture reached a very high value of 86.3%. Increasing the interaction parameter ($1/\alpha$) from 0 to 2.5 (Fig. 23b), which represents a significant deviation from the Taylor uniform strain assumption, resulted in a reduced correlation index of 55.3%. In fact, several previous studies have reported that Taylor-type deformation behavior can become more favorable at very large strains [81, 82]. This is attributed to grain fragmentation, which acts to eliminate heterogeneities in deformation and results in a more uniform strain distribution. During shear-type severe plastic deformation, the microstructure undergoes a significant transformation. The initially coarse grains (≈100 µm in the present study) become highly elongated and flattened, while intense fragmentation occurs. Consequently, new grains with much smaller sizes and significantly reduced aspect ratios are formed. This microstructural evolution is clearly visible in Fig. 16b. At higher strain levels, once a steady state is achieved, the grains can become nearly equiaxed. The underlying grain refinement mechanism is continuous dynamic recrystallization (CDRX), during which new grain

boundaries are progressively formed through the accumulation and rearrangement of geometrically necessary dislocations (GNDs).

Fig. 23c displays the simulated texture for Line1 obtained using the Taylor model with the discretized initial texture, rather than a random initial texture. The resulting direct texture correlation index was 77.5%, which is relatively high but is considerably lower than the 86.3% obtained with the initial random texture. This result can be explained by considering that the texture after FALEP processing was measured for Line1 using the EBSD technique. Because EBSD provides highly localized measurements, the analyzed area may contain grains that originated from only a limited number of initial grains, particularly when the starting grain size is quite large, about 100 µm. A simple geometrical estimation indicates that the final small grains (720 nm), captured within the EBSD scan area, originated from only around 12 initial coarse grains. Such a limited number of grains cannot adequately represent the true macroscopic initial texture of the material. This limitation may explain why the initial random texture produced better results than the actual initial texture.

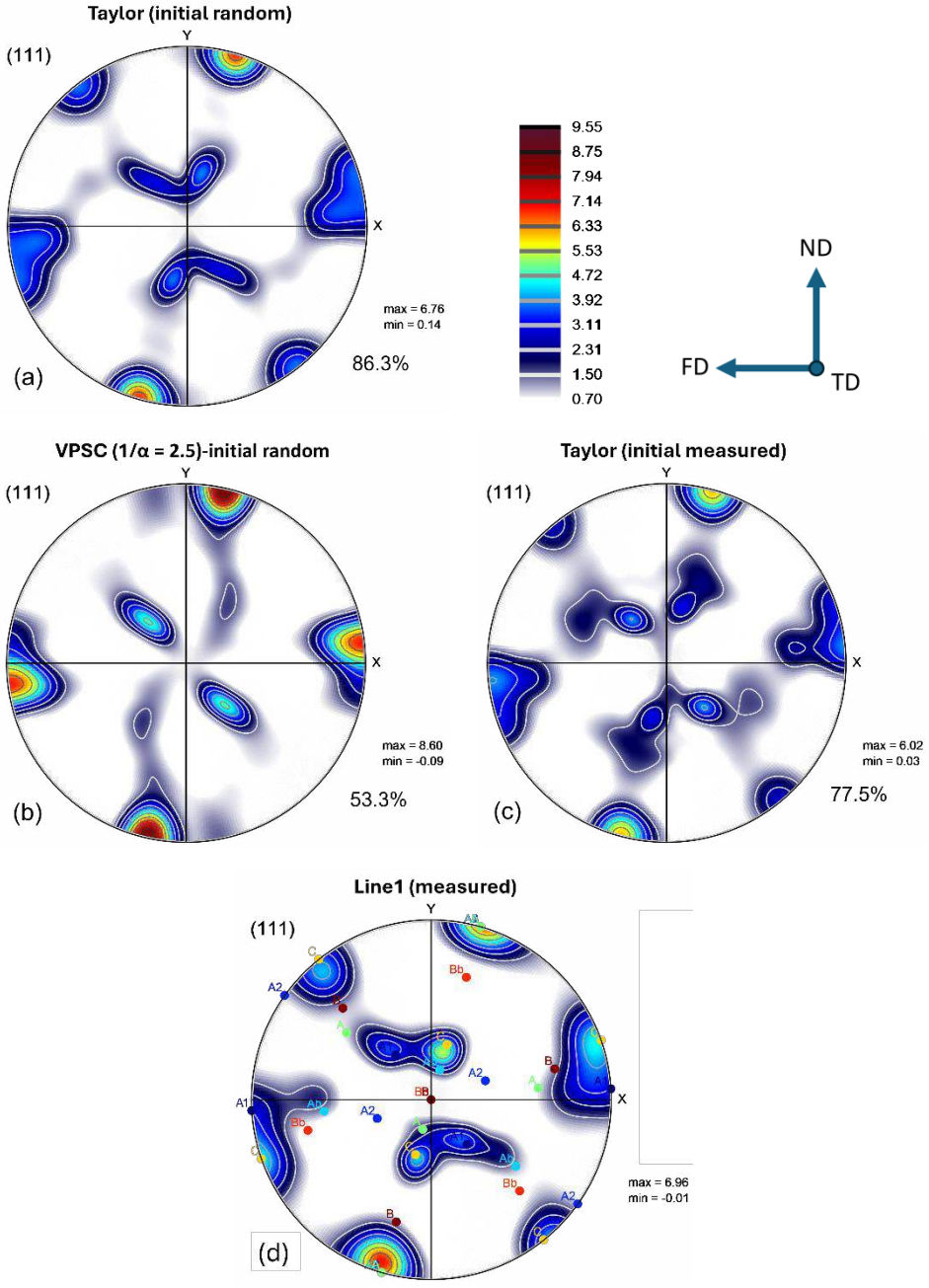

Fig. 23. Pole figures of simulated textures of Line1 using the new flow line model. **(a)** Taylor model with initial random texture. **(b)** Initial random texture with self-consistent model and an interaction parameter of 2.5. **(c)** Taylor model with initial measured texture. **(d)** Experimental texture of Line1.

Fig. 24 shows the texture simulation results for Line4. The highest direct correlation index, 77.3%, was achieved using the self-consistent model with an interaction parameter of $1/\alpha = 7$ and initial orientations discretized from the measured texture (Fig. 24a). Analysis of the flow line deformation behavior in Fig. 19 indicates that the three-stage deformation mode was less pronounced for Line4. In particular, the first shear zone was more extended for Line4, during which the flow line became curved and gradually changed its direction. The best agreement

between simulated and experimental textures was achieved when the contribution of the LCE stage was relatively small (see the parameters in Table 2).

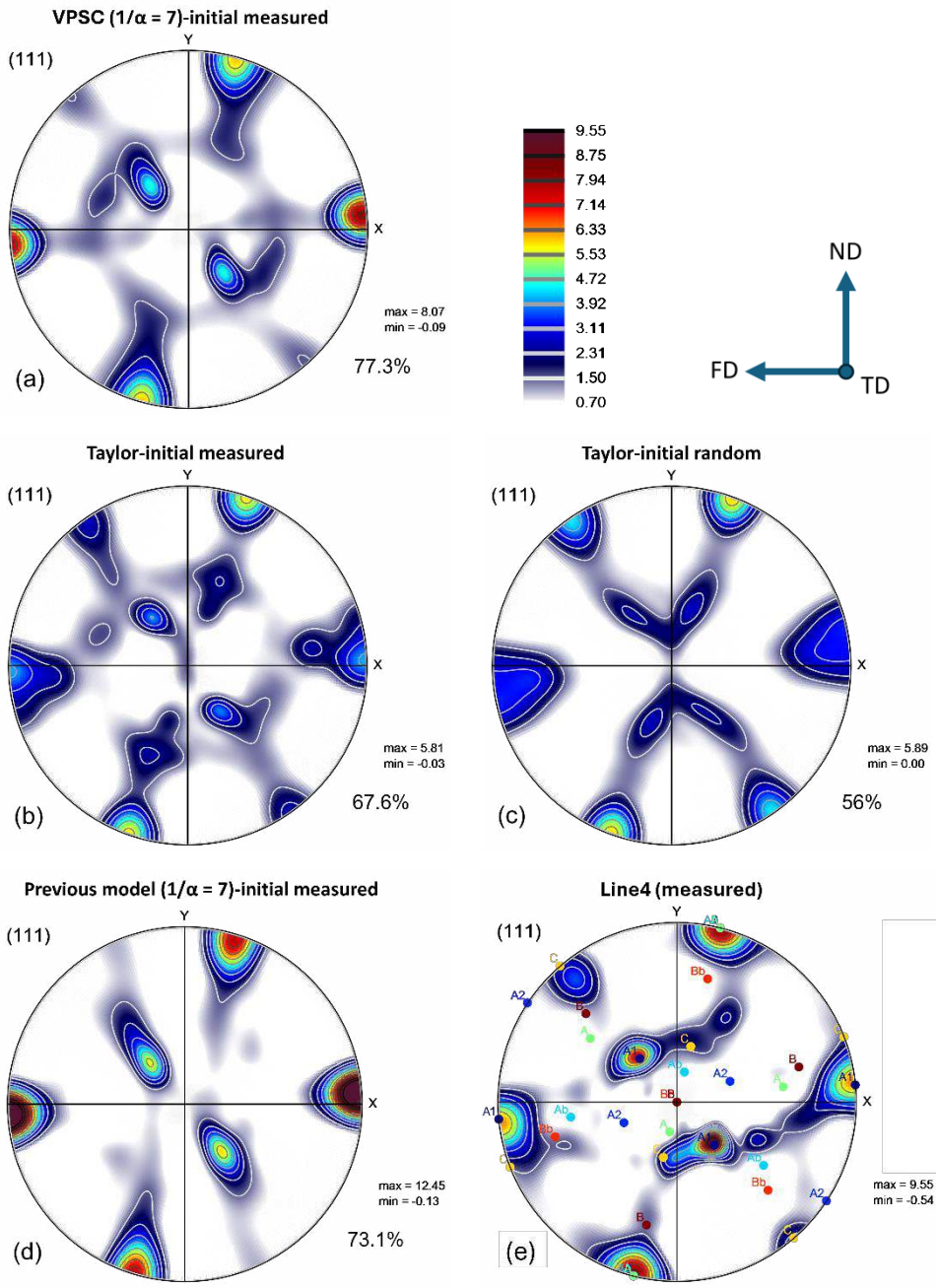

Fig. 24. Pole figures of simulated textures for Line4. **(a)** VPSC model using the initial measured texture with an interaction parameter of 7. **(b)** Taylor model with initial measured texture. **(c)** Taylor model with initial random texture. **(d)** Simulated texture using the previous power-law flow line model (Eq. 28) with the VPSC approach at an interaction parameter of 7 and initial measured texture. **(e)** Experimental texture of Line4.

When the Taylor model with the measured initial texture was employed for Line4, the agreement between the simulated and experimental textures decreased to 67.6% (Fig. 24b). The correlation index was further reduced to 56% when the initial random texture was used

with the Taylor model (Fig. 24c). These results can be explained by the fact that the final texture of Line4 was measured using X-ray. Consequently, the generated polycrystal for the Line4 simulations is more statistically representative of the experimental texture than in the case of Line1, where the texture was obtained by EBSD. Therefore, employing the measured initial texture, rather than a random texture, was well justified.

It remains to be clarified why the VPSC model provided better agreement for Line4, while the Taylor model performed better for Line1. First, the total deformation along Line4 was substantially lower than that for Line1, with equivalent strains of 2.03 and 2.98, respectively (see Table 2). Additionally, grain fragmentation was less pronounced in Line4, where the average grain size remained around 4.2 μm, compared to 0.72 μm in Line1. As a result, the application of the Taylor model was not justified due to insufficient strain and limited grain fragmentation. Therefore, the VPSC model with an interaction parameter of $1/\alpha = 7$ demonstrated a better performance for Line4 than the Taylor model. As previously discussed, increasing the $1/\alpha$ value results in greater deformation heterogeneity among grains, thereby leading to significant deviation from the uniform strain assumption of the Taylor model.

As mentioned earlier, a comparison of the predictive capability of the present model with that of the previous flow line model can be made for Line4, since for this flow line the earlier model provides a relatively good fit to the experimentally observed trajectory (see Fig. 19). The NECAP flow line model, as presented in Eq. (28), was therefore applied to Line4. The velocity gradient tensor was then constructed along the flow line using the analytical formulas reported in Ref. [46], and the corresponding texture evolution was simulated using the VPSC approach. Using this flow line approach, the total equivalent von Mises strain was 2.0, which is very close to the value predicted by the present three-stage flow line model (2.03). The highest texture correlation index was again obtained with the initial measured texture and the VPSC model, using an interaction parameter of $1/\alpha = 7$, yielding a value of 73.1%, as shown in Fig. 24d. When compared to the best value obtained from the new three-stage model (77.3%), these results indicate that the new flow line model is more effective than the previous approach in describing the deformation field for Line4 as well.

It is important to highlight the consequences of the observed heterogeneous deformation for the total plastic strain that can be achieved in the FALEP experiment. According to the classical ideal simple shear model, the von Mises equivalent strain should be 6.16 uniformly across the produced sheet. However, simulations yielded significantly lower values 2.98 and 2.03 for

Line1 and Line4, respectively, which are less than half of the expected strain. This estimation was based on the actual geometry of the flow lines and the reproduction of experimental textures through polycrystal simulations, and was further validated by the measured grain sizes, thereby providing strong support for these findings. The results clearly demonstrate that the material develops a highly heterogeneous flow field during FALEP processing, which leads not only to a pronounced strain gradient across the sheet thickness, but also to a substantial decrease in the total plastic deformation. The lower strain levels obtained from the present analysis, compared to those predicted by the simple shear model, clearly indicate that FALEP can exhibit significant deviations from the commonly accepted simple shear model of angular extrusion processes.

It should be noted, however, that this behavior was observed at an extrusion ratio of 10.5, while it was not reported in previous experiments, which had been performed on the same material at a higher extrusion ratio of 20 [76]. In that earlier study, both the microstructure and the crystallographic texture were found to be homogeneous across the extruded sheet. Furthermore, the next-neighbor disorientation distribution matched that measured at a shear of 20 in a direct simple shear experiment conducted by high-pressure tube twisting [83]. These findings indicate that a uniform simple shear state can be achieved in FALEP at an extrusion ratio of 20, while a gradient structure forms at the lower extrusion ratio of 10.5 due to reduced strain.

1.5. Conclusions

Flow line experiments were conducted on Al-1050 alloy subjected to the FALEP process at different extrusion ratios. The sample processed at an extrusion ratio of 10.5 was selected for further analysis. The microstructure and crystallographic texture after FALEP were characterized using EBSD and XRD at two different locations across the thickness of the produced sheet. Significant differences were observed in both grain size and texture between these regions, indicating a heterogeneous deformation state. Based on direct experimental observations, a new flow line model was developed to describe the deformation field and texture evolution during FALEP processing. The proposed model accounted for the complexity of the observed flow lines, identifying three distinct deformation stages: an initial simple shear, followed by a linear converging extrusion (LCE) stage, and a final simple shear near the exit channel. The velocity gradient for the LCE stage was derived, and polycrystal plasticity simulations were performed using the VPSC model to predict the final textures. Quantitative comparison of experimental and simulated textures validated the new modeling approach. The

accumulated strains were found to be less than half of those predicted by the classical simple shear model of angular extrusion. In addition, it was shown that the Taylor model predicted textures more accurately than the VPSC approach when the strain was sufficiently large and significant grain fragmentation occurred. The main conclusions of this study can be summarized as follows:

1. During FALEP processing of Al-1050 at an extrusion ratio of 10.5, significant grain refinement is observed in the upper region of the sheet, while the lower region exhibits substantially less refinement. Additionally, the crystallographic textures differ between these regions.

2. The material flow along a trajectory line is characterized by a three-stage deformation process, consisting of two simple shear stages separated by a linear converging extrusion (LCE) stage. For this intermediate stage, the velocity gradient tensor was derived using a two-dimensional fluid mechanics-based formulation.

3. The crystallographic texture evolution can be successfully simulated using polycrystal plasticity modeling combined with the proposed three-stage flow line approach. At lower strain levels, the VPSC model with an interaction parameter of 7 performs better, while at sufficiently large strains, the uniform deformation hypothesis corresponding to the Taylor model ($1/\alpha = 0$) yields better agreement with the experimental textures. Using this approach, experimental textures were reproduced with precisions of 86.3% and 77.3% for the upper and lower regions of the sheet, respectively.

4. A pronounced heterogeneity in both strain and grain size has been identified within the sheet, with strain values more than two times lower than those predicted by the classical simple shear model of angular extrusion. This demonstrates that the deformation field in FALEP can deviate significantly from an ideal simple shear state and can be considerably more complex than in other angular extrusion processes. Moreover, the resulting strain gradient is strongly affected by the FALEP geometry, particularly by the p/c ratio, and approaches the simple shear state as the extrusion ratio increases to $p/c = 20$.

Part 2: Theory of Grain Fragmentation and Grain Coalescence

2.1. Literature Review

2.1.1. Grain Refinement in SPD

It is widely accepted that the primary objective of applying SPD techniques is to refine the microstructure down to the ultrafine-grained (UFG) regime, thereby enhancing the material strength through the well-known Hall-Petch law [84, 85]. Therefore, it is essential to explore the mechanisms of grain refinement in plastic deformation. Grain refinement during plastic deformation occurs through dynamic recrystallization (DRX). However, DRX is not limited to SPD processing; it can also occur during conventional deformation techniques such as rolling and forging. Nevertheless, to obtain UFG microstructure, very large strains are required, which makes SPD methods the most suitable candidates for this purpose. DRX mechanisms are generally classified into two categories: continuous dynamic recrystallization (CDRX) and discontinuous dynamic recrystallization (DDRX). A schematic representation of these two mechanisms is shown in Fig. 25. CDRX is the dominant recrystallization mechanism in materials with high stacking fault energy, such as aluminum. During plastic deformation, dislocation annihilation and rearrangement can occur through a recovery process. The rearranged dislocations form dislocation walls with low-angle grain boundaries (LAGBs) within the original grains. The disorientation between subgrains progressively increases during deformation, leading to the transformation of LAGBs into high-angle grain boundaries (HAGBs). Consequently, new grains are formed through the progressive subdivision of the original grains. DDRX, however, is common in low stacking fault energy materials, such as austenitic stainless steels. This mechanism involves the nucleation and growth of small, equiaxed, dislocation-free grains. Therefore, grain boundary migration plays a key role in the DDRX process [86]. In this study, the focus is placed on grain refinement through CDRX, which can be regarded as grain fragmentation. Therefore, the nucleation and growth of new grains associated with DDRX are beyond the scope of this work.

CDRX is primarily driven by the development of internal misorientation inside grains as a result of dislocation rearrangement. Dislocations are typically divided into two categories: statistically stored dislocations (SSDs) and geometrically necessary dislocations (GNDs). While the mutual trapping of SSDs can lead to the formation of low-angle cell boundaries, their long-range lattice curvature cancels out, preventing the development of significant misorientation. In contrast, GNDs accumulate in an organized manner to form geometrically

necessary boundaries (GNBs), across which large misorientations are generated. Therefore, GNDs play the dominant role in grain refinement during CDRX [87, 88].

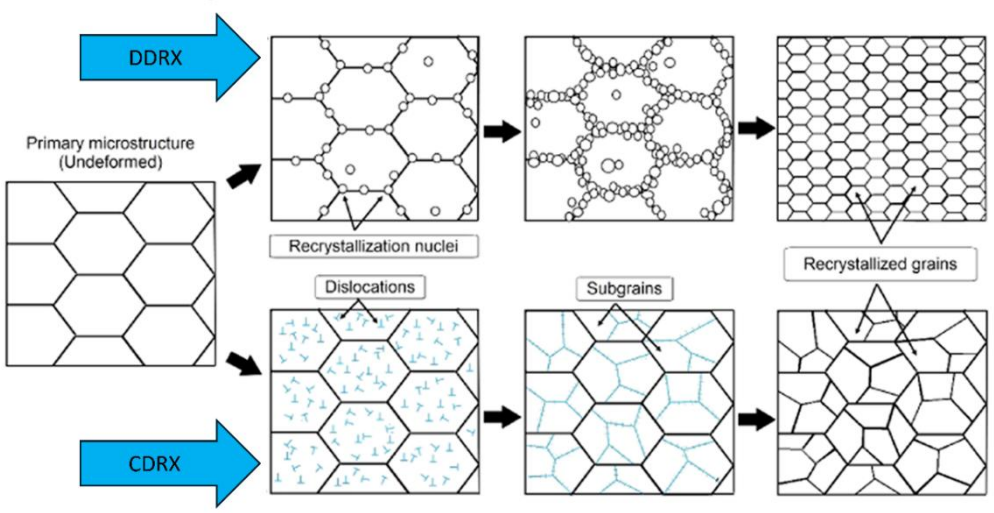

Fig. 25. Schematic illustration of the DDRX and CDRX mechanisms [89].

Suresh et al. [90] investigated the effect of the ECAP process at 250 °C on the microstructure and texture of Al-Cu-Li alloy. CDRX was identified as the main mechanism of grain refinement. The fraction of HAGBs progressively increased with increasing strain, which is evidence for the occurrence of CDRX (Fig. 26). During CDRX, LAGBs gradually transformed into HAGBs, leading to an increase in the fraction of HAGBs relative to LAGBs. Moreover, an overall texture weakening and deviations of the main texture components from their ideal positions were reported, which was attributed to CDRX during ECAP. The orientation of fragmented grains during CDRX differs from that of the original grain due to misorientation development, leading to a decrease in texture sharpness and the formation of an orientation cloud around the original orientation in Euler space. It is generally expected that the fraction of LAGBs increases during the early stages of deformation due to the development of intragranular misorientations associated with dislocation accumulation. However, in this study, the highest fraction of LAGBs was reported for the initial material. Although this observation was not discussed in that work, it can likely be attributed to the prior deformation history of the material. The authors stated that the starting material consisted of rolled rods, and no pre-annealing treatment before ECAP processing was reported. Furthermore, the misorientation distribution of the initial sample exhibited pronounced peaks at low misorientation angles, indicating the presence of a well-developed subgrain structure. It is therefore reasonable to assume that the rolling process introduced a high density of dislocations that rearranged into subgrain boundaries through recovery, resulting in a high fraction of LAGBs in the initial state.

During subsequent ECAP processing, many of these LAGBs gradually transformed into HAGBs through continuous dynamic recrystallization.

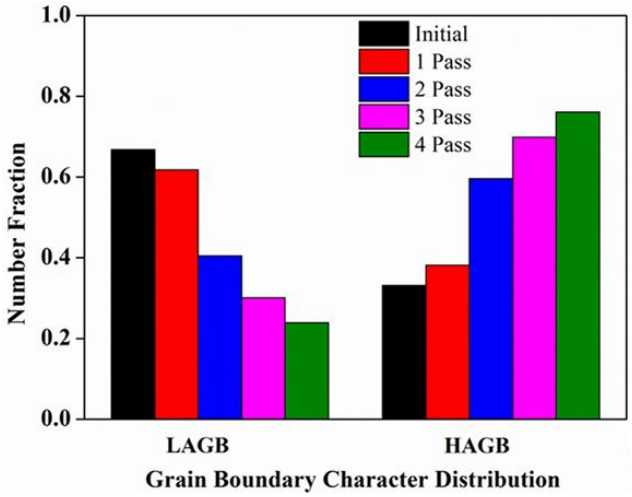

Fig. 26. Grain boundary character distribution for the initial and the ECAP-processed samples [90].

It is well known that grain refinement during SPD processing is saturated at sufficiently large strains, in which further refinement is not applicable, and the grain size stabilizes. The steady-state regime at ambient temperature was reported to occur at equivalent strains of 10-20 [91]. It is believed that a dynamic equilibrium between grain refinement and grain coarsening is established at this stage, preventing a further decrease in the average grain size. Different mechanisms have been proposed for grain coarsening, and their relative contributions are still under debate. On the one hand, a mechanically or stress-driven boundary motion has been suggested as the primary grain growth mechanism in the steady-state regime [92-94]. On the other hand, some studies reported that grain coalescence via the rotation of adjacent grains plays a key role in grain coarsening during the plastic deformation of nanocrystalline materials [95, 96]. At lower temperatures, shear-coupled grain boundary migration, as a conservative boundary motion mechanism, is plausible, with boundaries moving by sequential motion of atomic planes (disconnections) perpendicular to the applied shear stress [97]. However, grain coalescence is fundamentally a different mechanism, governed by the rotation of neighboring grains toward the same orientation and excluding any thermally or mechanically driven atomic exchanges. Once a grain grows above the limiting size via either of the mechanisms mentioned, it can be subdivided via CDRX, resulting in a stabilized grain size.

In-situ transmission electron microscopy (TEM) observations enable the analysis of grain coarsening mechanisms in ultrafine and nano-grained materials [98, 99]. Fig. 27 shows an experimental example of grain growth via grain boundary migration during the nanoindentation

of ultrafine-grained Al at room temperature. During indentation, the small grain (grain 1) is absorbed by its neighboring grains (grain 2 and grain 3), leaving only two grains after deformation.

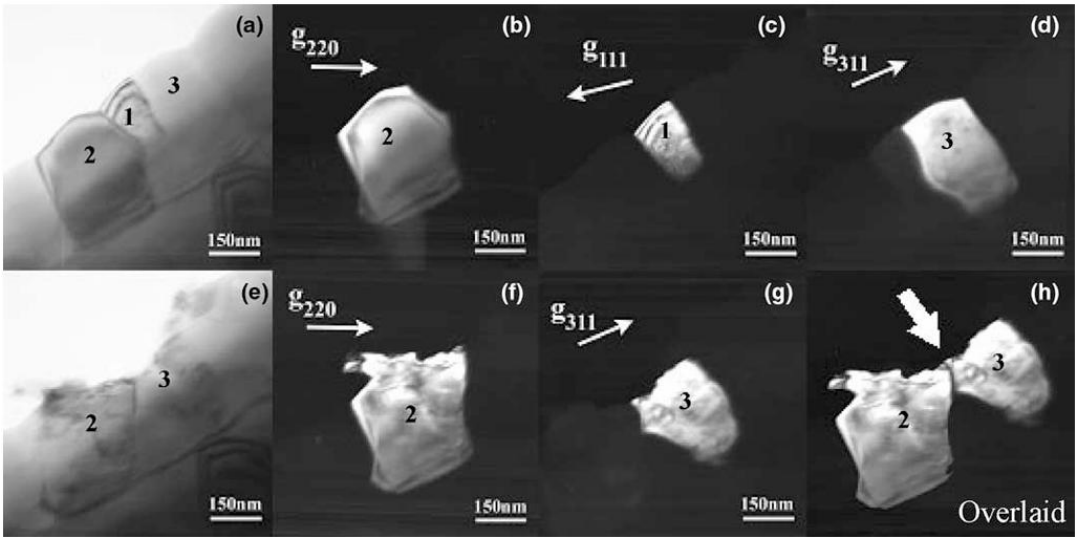

Fig. 27. (a) Bright-field image prior to indentation, displaying three grains labeled 1, 2, and 3. **(b)–(d)** Dark-field images of grain 2, grain 1, and grain 3 before indentation, respectively. **(e)** Bright-field image after indentation. **(f)** and **(g)** Dark-field images of grain 2 and grain 3 after indentation, respectively. **(h)** Overlay of dark-field images **(f)** and **(g)**, illustrating that grain 1, present before indentation, has been eliminated by the adjacent grains [98].

A case of grain coarsening through grain rotation and coalescence for a nanocrystalline aluminum film during in-situ TEM tensile testing is illustrated in Fig. 28. During deformation, grains A and B merge and form a larger grain. The identical contrast of the two grains in the dark-field images confirms that they have nearly the same crystallographic orientation. Their merging during in-situ observation provides clear evidence of orientation alignment followed by grain coalescence.

Most studies have examined dynamic grain coarsening mechanisms only at the steady-state stage of deformation, while the possibility of grain coarsening occurring earlier during deformation remains poorly understood. Therefore, one of the primary objectives of this study is to develop a general theory that explains the possibilities of deformation-induced grain coarsening over a broader range of grain sizes.

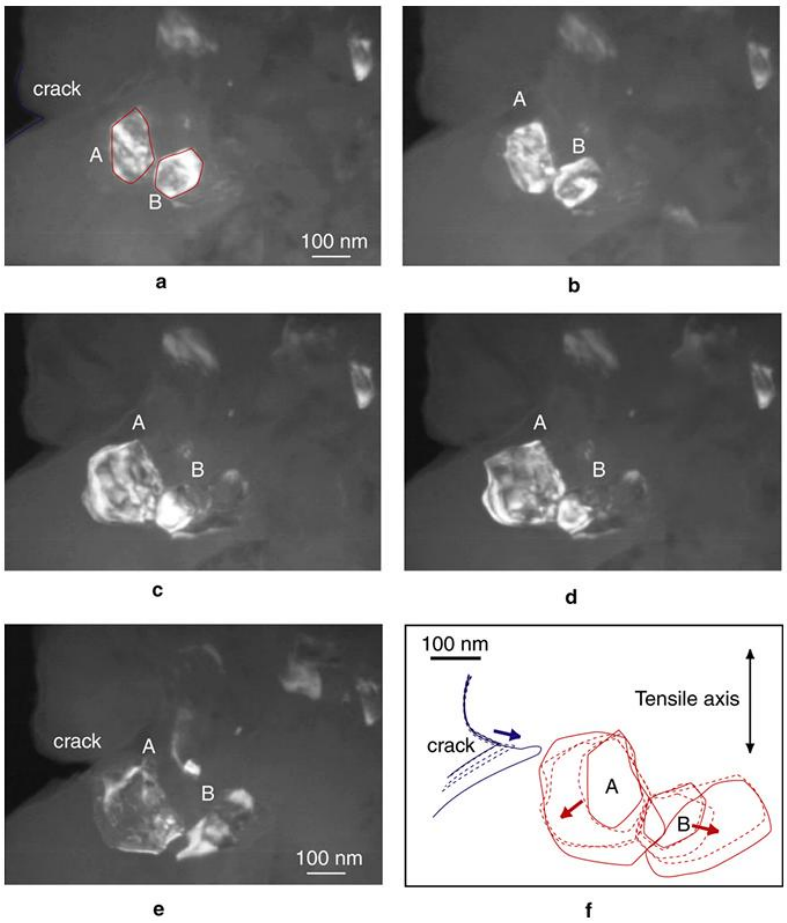

Fig. 28. Grain growth by rotation-induced coalescence of adjacent grains. **(a)** t = 0 s **(b)** 6 s, **(c)** 20 s, **(d)** 22 s, **(e)** 49 s, and **(f)** sketch of the grain shape evolution from **(a)** to **(e)** [99].

A deeper understanding of grain refinement in SPD requires a clear evaluation of the interrelation between the texture and CDRX. Naghdy et al. [100] investigated the microstructure and texture evolution of commercially pure aluminum after HPT processing using 3D EBSD technique. Fig. 29 shows the grain size distribution of ideal and non-ideal orientations after an equivalent strain of 5. Grain fragmentation was found to be less effective for grains in the vicinity of ideal positions. Thus, grains with non-ideal orientations fragmented further and had smaller grain sizes than grains with ideal shear orientations. This trend was explained by the difference in lattice rotation between the two groups. The small lattice rotation of ideal orientations prevented misorientation development inside these grains. As a result, their fragmentation process was delayed.

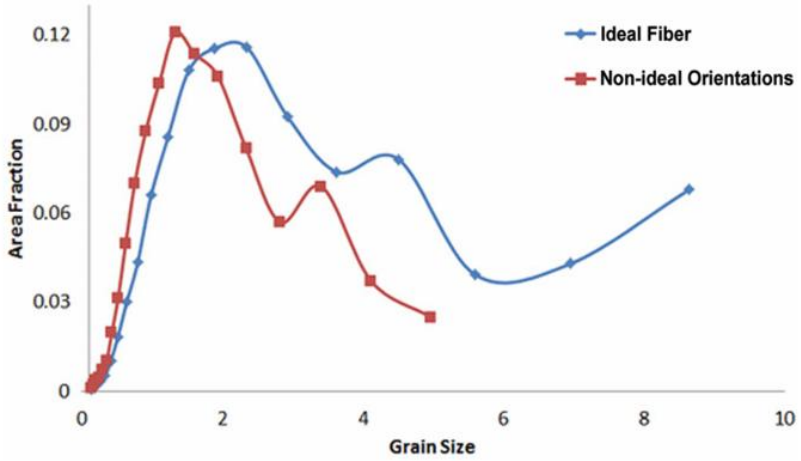

Fig. 29. Grain size distribution at a strain of 5 using a large-area EBSD scan, showing that orientations in the vicinity of ideal fibers have a larger average grain size [100].

Khalfallah et al. [101] reported grain coarsening at an equivalent strain of 10.2 in HPT-processed Al-6061 and attributed this effect to shear-induced boundary migration. However, this mechanism alone cannot explain the observed sharp increase in the intensity of the ideal shear components at this deformation stage. Fig. 30 indicates that some larger grains are formed with a distinct morphology at the ideal shear positions, consistent with texture-assisted grain coalescence rather than migration-driven growth. Although the authors reported stable Goss and Brass components, which are debatable since these are ideal FCC rolling components, not shear, the formation of larger grain sizes with the ideal shear orientation is in agreement with the results of the previous study [100]. However, the larger grains with the ideal shear orientation cannot be attributed to a delay in grain fragmentation, as a fully refined microstructure had already been achieved in the previous deformation stage. This clearly indicates the occurrence of dynamic grain coarsening, which is closely related to texture evolution and can be described as texture-driven grain coalescence. The fundamental principles of this mechanism will be discussed in the following sections.

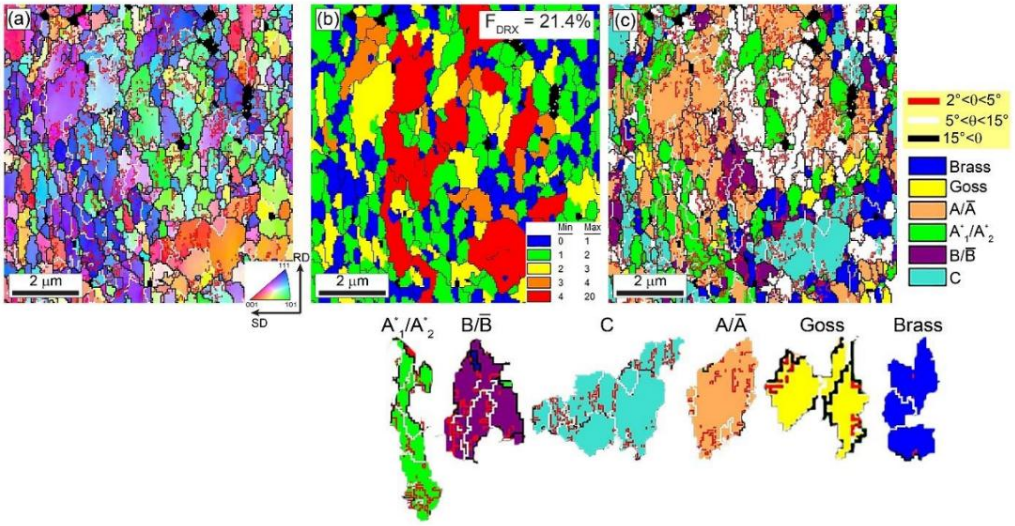

Fig. 30. (a) Inverse pole figure (IPF) map, **(b)** grain orientation spread (GOS) map and **(c)** grain orientation map of selected region from a disc HPT-processed at ε_{eq} = 10.2; examples showing the shapes and the presence of different grain boundary types in A_1^*/A_2^*, $B/\bar{B}$, C, $A/\bar{A}$, Goss and Brass oriented grains [101].

2.1.2. Modeling of Grain Fragmentation

So far, the majority of studies on CDRX and grain fragmentation have relied on experimental observations, while limited attempts have been made to establish physically based models that can capture the essential features of CDRX. Gourdet and Montheillet [102] proposed a physically based CDRX model, in which grain fragmentation is governed by the progressive increase of subgrain misorientation. Once a critical misorientation (~15°) is reached, subgrain boundaries are reclassified as HAGBs, and the corresponding fraction of them is counted as new grains. However, this approach does not account for topological or neighboring conditions when identifying grains. The crystallographic texture effects are also neglected. The lack of geometrical details of grain topology and the local neighbor interactions prevent the application of this model for identifying grain coalescence.

Frydrych et al. [103] proposed a three-scale crystal plasticity model for grain refinement in ECAP of FCC alloys. In this approach, the polycrystalline aggregate is first subdivided into grains (referred to as metagrains). Then, metagrains are further divided into subgrains whose initial orientations are slightly distorted with respect to the nominal metagrain orientation. Taylor and three variants of the VPSC models (secant, tangent, and affine) were applied to the polycrystalline aggregate subjected to multiple ECAP passes. The modeling procedure was carried out in two steps: first, the metagrain-polycrystal transition was analyzed, followed by the subgrain-metagrain transition within each metagrain. Misorientation angles between subgrains were computed with respect to the mean orientation of their parent metagrain.

It should be noted, however, that the model does not include a subgrain-size parameter, and the predefined numbers of grains and subgrains remain constant during deformation. This model actually focuses on the calculation of the misorientation angle between the subgrains of each metagrain rather than on the actual refinement of grain size. Nevertheless, a key conclusion from the results of this study is that fragmentation is more pronounced in grains with a greater number of simultaneously active slip systems. In such grains, the misorientation between the subgrains rapidly increases because different sets of slip systems operate in neighboring subgrains.

In a later study [104], the authors employed a full-field crystal plasticity finite element method (CPFEM) to simulate grain refinement during a single-pass ECAP process. The heterogeneous deformation generated by the die geometry and boundary conditions in the CPFEM framework enabled the development of local misorientations and the formation of new grains. However, the potential occurrence of grain coalescence was not considered in this work. Moreover, the CPFEM simulations are computationally expensive, limiting their application to very large deformation levels.

The cellular automaton (CA) method has also been widely used to simulate dynamic recrystallization [105, 106]. However, most CA-based studies have focused on DDRX rather than CDRX [107]. Azarbarmas et al. [108] proposed a two-dimensional CA framework to simulate CDRX. However, the key characteristic of CDRX, which is the gradual transformation of LAGBs into HAGBs, was not included. In this model, new grains were generated through nucleation, corresponding to a DDRX mechanism rather than fragmentation (CDRX), and only grain boundary migration and heterogeneous nucleation along grain boundaries were restricted. Furthermore, the subgrain size was determined phenomenologically, and the influence of the initial orientations and texture was not taken into account. Similarly, in another study [109] on the three-dimensional frontal cellular automata model of grain refinement during SPD, the grain refinement was governed by the nucleation and propagation of new grains, resembling a DDRX-type process. This model did not incorporate the lattice rotation and subgrain rotation kinetics that are essential to describe the progressive conversion of low-angle to high-angle boundaries during CDRX. Consequently, the model could not capture the underlying physical mechanisms of CDRX related to intragranular misorientation development and orientation-dependent grain size evolution.

A well-recognized grain fragmentation model was proposed by Toth et al. [110] in 2010. In this model, grain fragmentation is attributed to the lattice curvature that develops within grains during plastic deformation. The core idea of this model is that lattice rotation near grain boundaries is retarded by the pinning effect of neighboring grains. Consequently, the lattice rotation of the center region of the grain, which is not affected by adjacent grains, is faster, while the lattice rotation of the outer regions is smaller due to the constraint "friction" effect of grain boundaries. As a result, misorientation between the middle and outer regions of the grain increases, and new grain boundaries can be formed, meaning that grain subdivision takes place. In the numerical software of this model, the grain shape is simplified as a cube with equal size between the grain boundary zone and the middle zone. In this case, an initial grain in 3D is a cube constituted of 27 smaller cubes of the same size (like a Rubik cube), as shown schematically in Fig. 31.

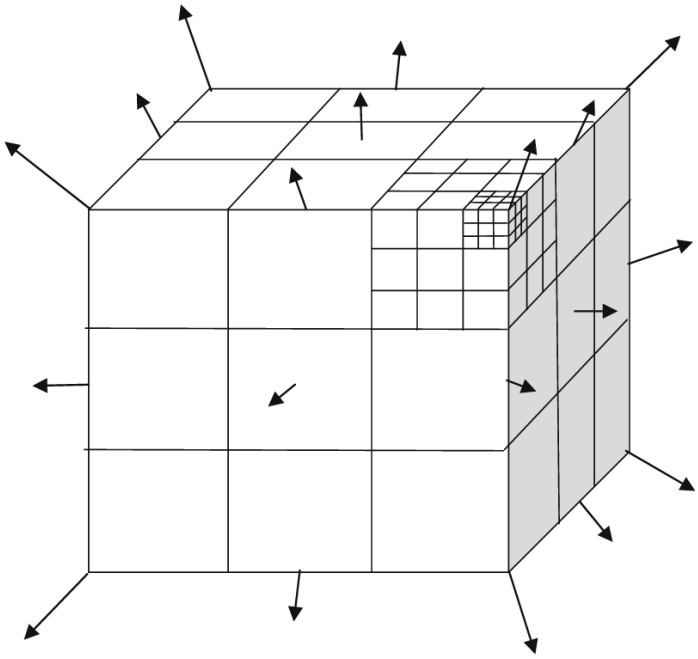

Fig. 31. A cube-shaped grain is subdivided into 27 subgrains, with the resultant misorientation axis indicated for each subgrain. Additionally, next-level subdivision at two smaller scales is illustrated for a corner subgrain [110].

In this configuration, there is only one element in the center, which does not develop misorientation. There are six elements on the faces with one grain boundary, twelve elements on the edges with two grain boundaries, and eight elements on the corners with three grain boundaries. The main parameter of this model is the grain boundary "friction coefficient", which controls the degree of lattice rotation retardation near the grain boundaries. Its value ranges from 0 to 1. The maximum value (1.0) leads to the largest constraint "friction" effect at

grain boundaries, promoting the development of lattice curvature. The tuned value for this parameter was proposed to be 0.5.

The resultant lattice rotation rate of a subgrain depends on four factors: (i) the lattice rotation rate of the parent grain, (ii) the number of grain boundaries, (iii) the boundary friction coefficient, and (iv) the angle between the lattice rotation vector and the resultant grain boundary normal. The model is adapted for three hierarchical subdivision levels. At each level, the parent cube can be subdivided into 27 smaller cubes of equal volume. In this way, the total number of subgrains (smallest cubes) in an initial grain is $27 \times 27 \times 27 = 19683$. Once the orientation difference between a subgrain and its parent grain (the center cube) reaches a critical value (5° in this model), the subgrain is treated as a new grain, and the next level of subdivision is applied to that. Note that when the critical misorientation is achieved for a subgrain, it would be independent of the parent grain and crystal plasticity solution, including slip rates, lattice rotation rate, and strain-hardening, should be calculated for this new grain at each strain increment.

An indirect interpretation of this model is that when the lattice rotation is zero (i.e., ideal orientations), no fragmentation can occur. The necessary misorientation criterion for fragmentation in this model is assumed to be obtained by different lattice rotation rates between the middle and outer parts of the grain. Obviously, for zero lattice rotation, there would be no misorientation inside the grain. Thus, grain fragmentation will be delayed at the ideal orientations.

Compared to other CDRX modeling approaches, this model offers several distinct advantages. First, its geometrical configuration enables the identification of grains based on physical neighborhood relationships. Second, the fractal-type subdivision scheme employed in this model is physically meaningful, as CDRX during plastic deformation proceeds progressively, level by level, from the initial coarse-grain stage to the final steady-state structure. Finally, a unique feature of this model is the intragranular misorientation development mechanism driven by non-uniform lattice rotation rate. As discussed earlier, CDRX occurs through the formation of orientation gradients within grains, followed by the rearrangement of GNDs and the progressive transformation of low-angle to high-angle grain boundaries under the influence of texture evolution [111, 112]. This model successfully incorporates the essential criteria for internal misorientation development in CDRX and reproduces the main microstructural and

mechanical aspects of large plastic deformation, including grain size and disorientation distributions, texture evolution, and strain-hardening behavior.

The theoretical foundation of grain fragmentation induced by lattice curvature and the fractal geometrical configuration of this model is physically sound and provides a strong conceptual link between crystal plasticity and microstructural evolution. In the present work, this model has been improved by incorporating 2D and 3D flooding algorithms for accurate grain detection, accounting for neighborhood relationships at the finest voxel level. This improvement enables a quantitative evaluation of both grain fragmentation and grain coalescence during large plastic deformation. The fundamental principles and implementation details of the modified grain refinement model are presented in Section 2.3.2.

2.1.3. Grain Coalescence

To date, most studies have considered grain refinement a one-way process, in which grain fragmentation occurs progressively during straining up to the saturation regime (minimum grain size). Grain refinement, however, can result from competition between two opposing mechanisms: grain fragmentation and grain coalescence; both are strongly influenced by texture evolution. As mentioned earlier, the possibility of grain coalescence has generally been considered only at the steady-state stage, whereas very few studies (only two reports to date) have addressed its occurrence during ongoing plastic deformation, prior to reaching the saturation regime [113, 114].

The effect of texture evolution on grain coalescence in ECAP was reported for the first time in Ref. [113]. Fig. 32 shows the microstructures before and after the ECAP process. After four passes through a 130° ECAP die, the average grain size increased significantly from 8.96 μm to 24.2 μm (in area fraction). Polycrystal simulations were performed using EBSD data of the initial sample, including grain sizes, grain orientations, and first-neighbor relationships. The simulations reproduced the occurrence of grain coalescence after four passes, although the extent of coalescence was smaller than that observed experimentally. The polycrystal simulations were performed in 2D, whereas coalescence is a 3D process, and grain size can increase in all three dimensions. In that study, grain coalescence was attributed to texture evolution, in which adjacent grains rotated toward the same ideal orientation. As a result, the disorientation between these grains continuously reduced, and HAGBs between them transformed into LAGBs, thereby forming a single larger grain.

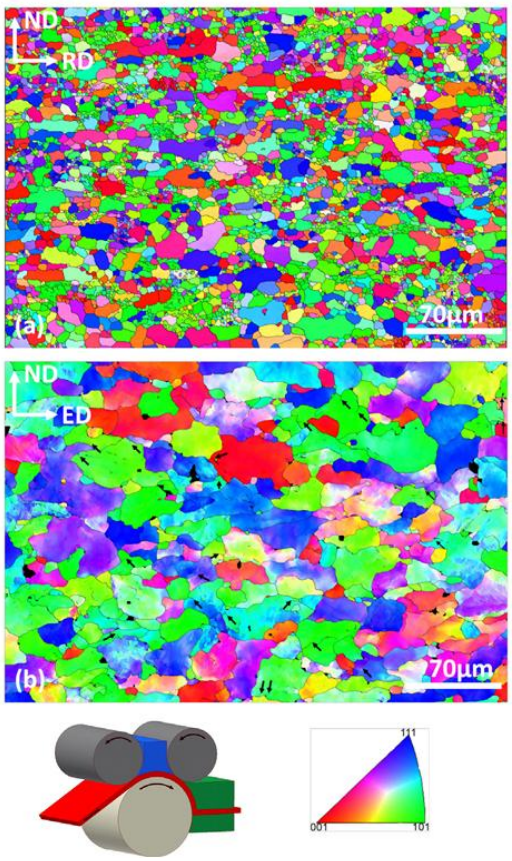

Fig. 32. Inverse pole figure maps of **(a)** as-received low carbon steel; **(b)** four-pass ECAE–Conformed low carbon steel. Grain boundaries with disorientations larger than 5° are depicted by black lines. The color code displays the plane normal (TD) in the crystal reference system. Black arrows in **(b)** indicate disappearing grain boundaries. The schematic of the sheet ECAP processing machine is also shown [113].

Zhang and Toth [114] investigated the texture-induced grain coalescence during SPD using three-dimensional polycrystal simulations. Three-dimensional polycrystalline aggregates were first generated with a cellular automaton approach, followed by texture simulations under simple shear up to a shear strain of 8 using the Taylor polycrystal model. Three different initial textures were examined: random, cube-type, and shear-type. The simulations revealed remarkable coalescence volume fractions: approximately 40% for the initial shear texture, 30% for the random texture, and 20% for the cube-type texture. These results demonstrate that grain coalescence plays a significant role in microstructural evolution and must be considered when studying grain refinement. Fig. 33 illustrates the morphological features of several coalescing grains at a shear strain of 2. The color code is based on the Euler angles. Interestingly, as the number of coalesced grains increases, the resulting grain morphology becomes irregular and complex. In EBSD measurement, only 2D sections of such 3D morphologies are observed. Nevertheless, these particular morphologies of coalesced grains can still be recognized in EBSD maps, as shown in the next section.

It should be noted that the cellular automaton coupled with the polycrystal texture framework employed in Ref. [114] did not account for grain fragmentation. As a result, the grain size in the simulations could remain constant or increase through coalescence, while fragmentation below the initial grain size was not possible. Nevertheless, the primary objective of the study was to address the significance of grain coalescence during plastic deformation, which was successfully achieved.

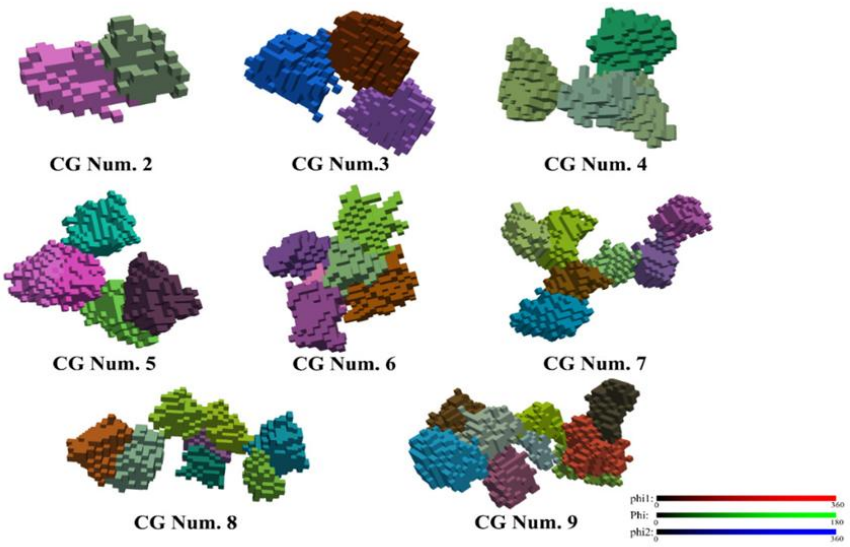

Fig. 33. Typical morphologies for grain coalescence at a shear strain of 2. The deformation-induced grain shape change is not displayed; the grains are represented in their initial form. The colors refer to the Euler angles. CG Num. indicates the number of coalescing initial grains [114].

The use of the term “grain coarsening” in the mentioned studies can be debated. In the context of DDRX, coarsening typically refers to grain growth driven by grain boundary migration. In contrast, boundary migration is not the governing process in grain coalescence. The coalescence mechanism is governed by the convergent nature of the rotation field near the ideal orientations, where disorientation between adjacent grains rotating toward the same ideal orientation gradually decreases. Once the disorientation between these grains falls below the critical detection threshold in the experimental measurements, the grain boundaries disappear, and a larger grain is detected. Therefore, in the following, the term “grain coalescence” is adopted to address this mechanism.

2.2. Experimental Procedures and Results

2.2.1. FALEP of Copper Sample

A commercially pure copper sample was processed via the FALEP technique at room temperature using the FALEP machine at the LEM3 laboratory in Metz. The specimen was a square billet with a cross-section of 20 × 20 mm^2. The entry and exit channel dimensions of the FALEP die were 20 mm and 2.3 mm, respectively, corresponding to an extrusion ratio of 8.8. Microstructural and crystallographic texture analyses were performed by EBSD using a JEOL JSM-6500F field-emission gun scanning electron microscope. EBSD measurements were conducted on the lateral surface (FD-ND plane), and the data were analyzed using the ATEX software [80]. The step size was set to 50 nm to ensure adequate resolution of subgrain structures, and a minimum disorientation angle of 5° between adjacent pixels was used as the threshold for grain boundary detection.

2.2.2. Microstructure and Texture of Cu-FALEP Sample

Fig. 34a presents the EBSD grain size map of the Cu-FALEP sample, in which the coloring is based on the grain size. The area-weighted average grain size is 1.2 μm, confirming that a UFG microstructure was successfully produced. However, the distribution of grain sizes is clearly non-uniform and bimodal, characterized by several relatively larger grains embedded within a matrix of well-refined ultrafine grains. The presence of these larger grains indicates that the microstructure has not reached the steady-state stage at the applied extrusion ratio.

The area fraction grain size distribution (Fig. 34b) indicates that the majority of grains are refined to sizes below 1 μm, as evidenced by several pronounced peaks within this range. Meanwhile, distinct peaks corresponding to larger grains are also present in the distribution. However, their area fractions are significantly lower than those associated with the fine-grain population. This confirms the bimodal nature of the microstructure, in which a small number of larger grains coexist with a dominant fraction of ultrafine grains.

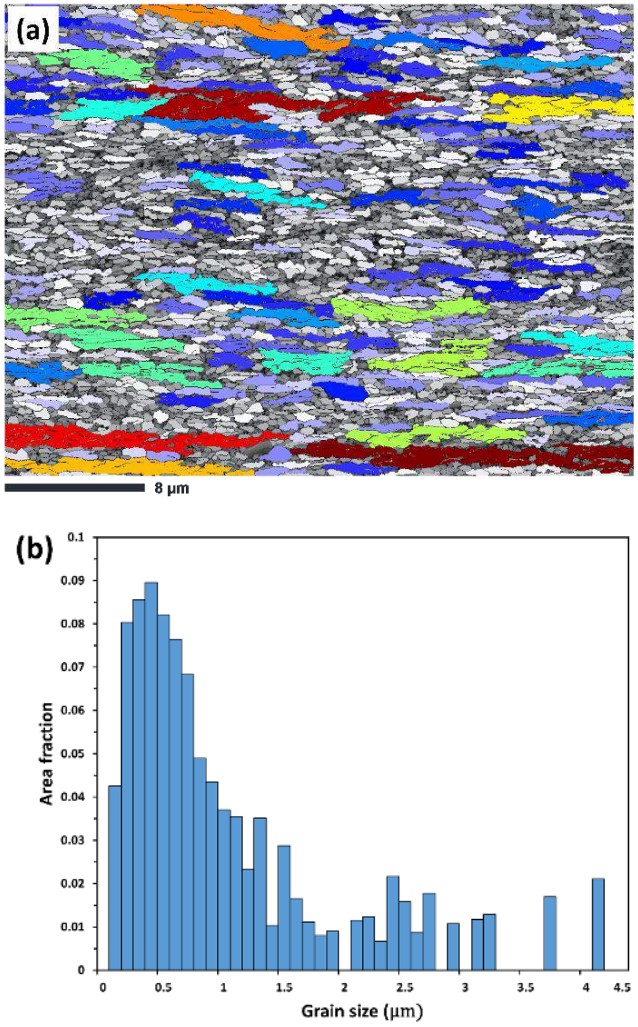

Fig. 34. (a) The microstructure of the Cu sample after the FALEP process with an extrusion ratio of 8.8 (The coloring is based on the grain sizes). **(b)** The corresponding area fraction grain size distribution (bin size = 0.1 µm).

Fig. 35a presents the ODF sections of the measured texture for the Cu-FALEP sample at φ_2 = 0° and 45°. The locations of the ideal shear texture components are also indicated in these sections. These ideal orientations were calculated based on the simple shear model. The position of the shear plane, however, was determined from the ideal shear fibers observed in the measured texture. In this case, the maximum volume fraction of ideal shear components was considered, which was obtained when the shear plane was located 14° away from the x-axis. After the FALEP process, a typical shear texture is observed, with the C component showing the highest intensity, followed by the B and A1 components. Furthermore, some grains rotated along the rotated-cube fiber ($\phi = 0°$), resulting in the appearance of this non-ideal shear fiber. Fig. 35b shows the next-neighbor disorientation distribution of the Cu-FALEP sample. The random Mackenzie distribution is also presented by a solid black line. The disorientation distribution of the Cu-FALEP sample deviates from the random distribution due to the

development of a strong shear texture. Two disorientation angle ranges with high frequencies are observed: below 15° and above 45°. The high disorientation angles correspond to the grains located at different ideal positions, as the ideal shear positions are relatively far from each other in Euler space. The high frequency of lower disorientation angles can be attributed to neighboring grains with the same ideal orientations.

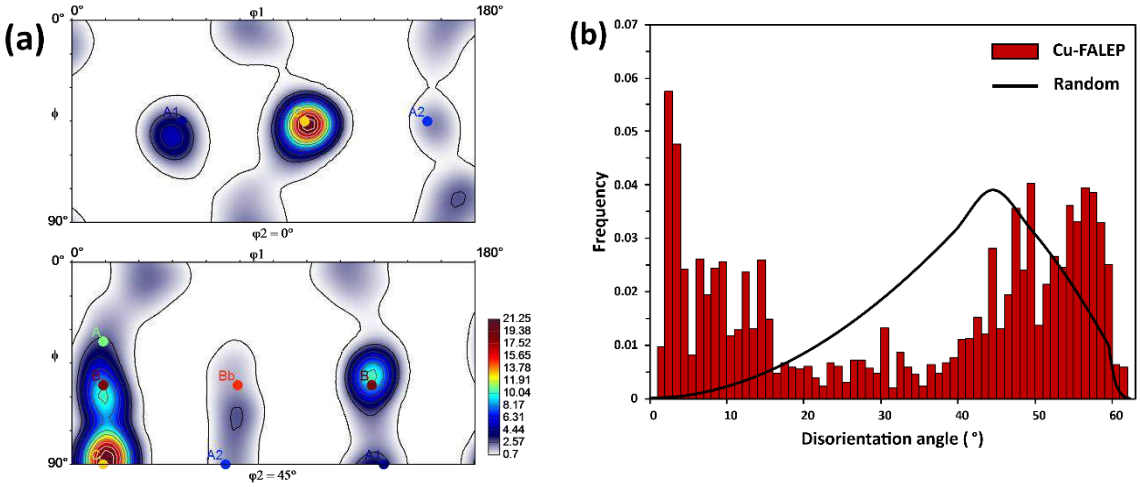

Fig. 35. (a) φ_2 = 0° and 45° ODF sections of the measured texture of the Cu sample after the FALEP process. The symbols correspond to the ideal orientations of FCC shear textures. **(b)** The corresponding next-neighbor disorientation distribution (bin size = 1°). The random Mackenzie distribution is shown by a solid black line.

To examine the relationship between grain size and crystallographic texture, the microstructure has been partitioned into two groups based on the grain size: larger grains and small grains. Grains above 2.15 μm are in the larger grains group (Fig. 36a), while grains below 620 nm are in the small grains group (Fig. 36b). The black regions in the partitioned microstructures are filtered. The larger grains exhibit an irregular morphology. It seems that they are formed by sticking some unpaired fragments. By comparing the morphology of these larger grains with the 3D simulation results in Fig. 33, the same features are observed, suggesting that these larger grains may result from the coalescence of some already fragmented grains. Note that the coalesced grains in the simulation were presented in their initial form, and the shape change corresponding to the shear deformation was not taken into account. By considering the necessary shape change of the grain clusters after shearing, the morphological resemblance between the simulated coalesced grains and the experimental larger grains could be even higher, as shown in Fig. 36c. The small grains exhibit a nearly equiaxed, highly uniform morphology. The homogeneity and lack of elongated or irregular features suggest that these grains are already within, or very close to, the steady-state regime of grain size.

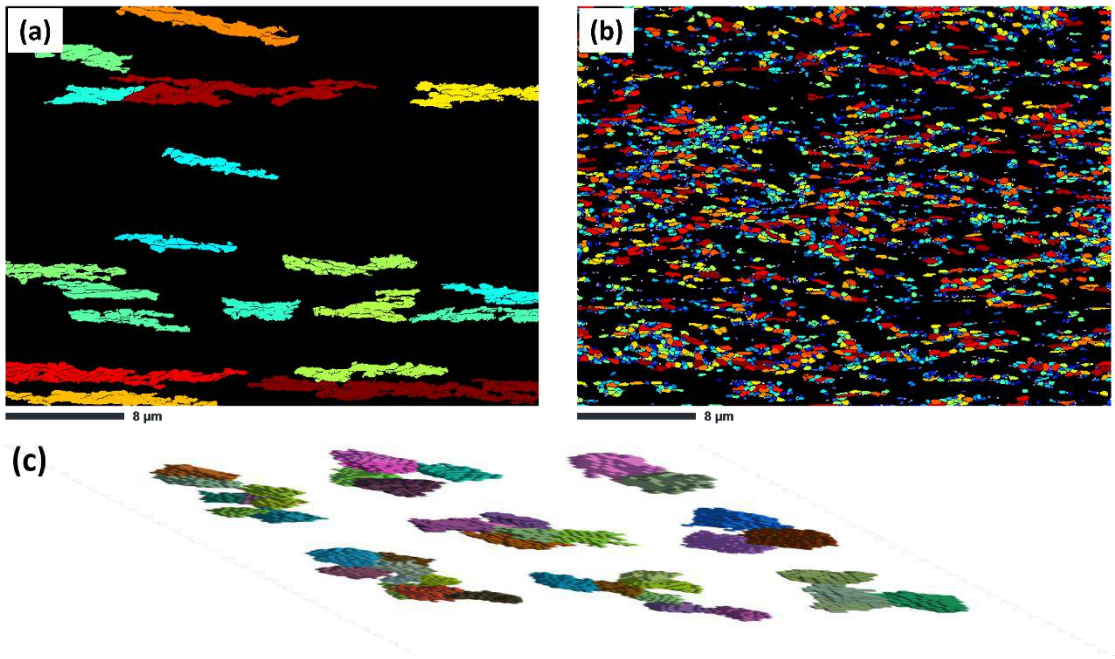

Fig. 36. The microstructure of the Cu-FALEP sample **(a)** larger grains, **(b)** small grains. The dark areas are filtered. The grains are colored according to the grain size scale. **(c)** The simulated coalesced grains in Fig. 9 after imposing the corresponding shape change of shear strain of 2.

Fig. 37 shows the ODF sections at φ_2 = 0° and 45° for larger and small grains groups. By comparing the texture of larger and small grains, a clear and significant trend can be observed. Larger grains are almost always in the vicinity of the ideal shear positions, while small grains are spread out in a wider range of orientation space. Small grains do not always occupy the ideal orientation positions. This trend aligns with previous studies, which showed that grains at ideal orientations were less fragmented than those at non-ideal orientations. Moreover, the maximum texture intensity for larger grains is around 56, which is quite higher than that of small grains (10.8). This is also because the larger grains occupy nearly the same orientations, but the small grains' orientations vary in the orientation space. This weaker texture is characteristic of grains that have been heavily refined and rotated away from the ideal positions during deformation. Meanwhile, several ideal shear components, such as A2, Bb, and A, which appear in the small grains texture, are almost completely absent in the larger grains texture. The texture results show that larger grains preferentially occupy the ideal C position rather than other ideal positions. This suggests that grain refinement during FALEP processing is strongly orientation dependent. Grains with different initial orientations exhibit distinct fragmentation behavior under shear deformation.

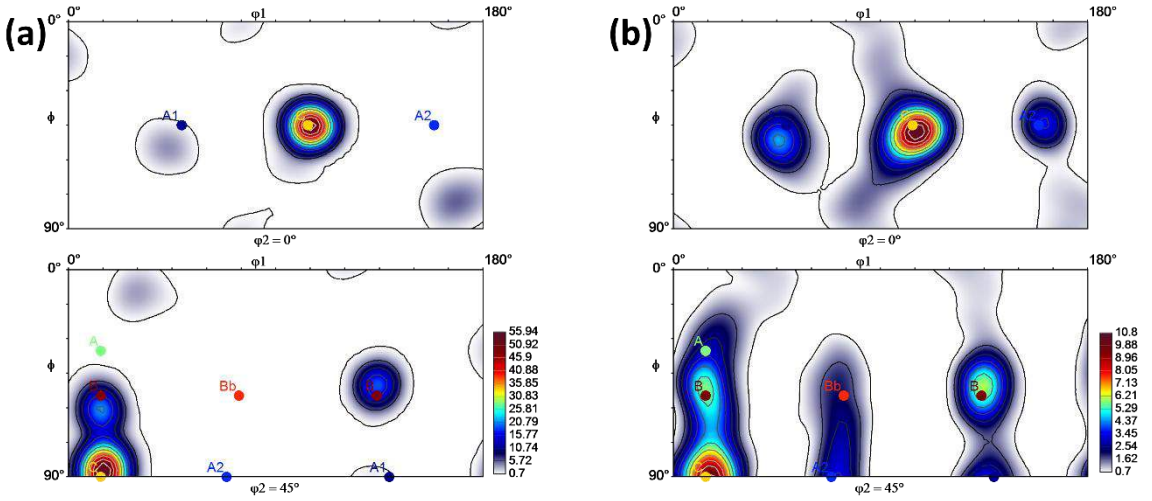

Fig. 37. $\varphi_2 = 0°$ and 45° ODF sections of the Cu-FALEP sample after the microstructure partitioning. **(a)** Larger grains, **(b)** small grains. The symbols correspond to the ideal orientations of FCC shear textures.

A quantitative comparison of the two grain-size groups further highlights their distinct orientation characteristics. The volume fraction of the individual ideal shear components, as well as the combined volume fraction of all ideal components, was calculated using a 20° disorientation threshold around the ideal positions, and the results are presented in Fig. 38. As shown, 90.6% of the large grains are in the vicinity of the ideal positions. For the small grains, this value decreases to 76.6%, indicating that a larger portion of the refined grains occupies non-ideal positions in the orientation space. However, the volume fraction of ideal components for small grains is still high because all grains, whether small or large, undergo the same deformation mode, i.e., the simple shear deformation. Nevertheless, the results show the tendency of larger grains to occupy the ideal shear positions in the orientation space.

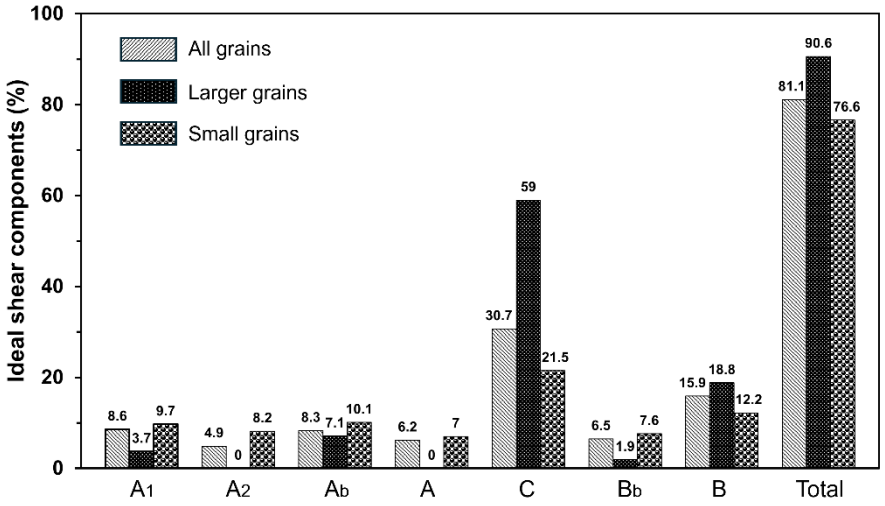

Fig. 38. The volume fractions of the ideal shear components for all grains, larger grains, and small grains.

Fig. 39 presents the grain orientation spread (GOS) and the kernel average misorientation (KAM) maps for larger and small grains. The GOS is defined as the average angular deviation between the orientation of each pixel and the mean orientation of the entire grain [115], thereby capturing long-range intragranular misorientation. In contrast, the KAM reflects a more localized orientation gradient, computed as the average orientation difference between each pixel and its immediate neighbors [116].

The average GOS value of larger grain is 5.6°, which is relatively high. The GOS map clearly illustrates remarkable orientation deviations across different regions within the larger grains. Interestingly, the KAM map of larger grains shows a different trend. The average pixel-to-pixel misorientation is only 0.57°, which is considerably lower than the GOS value. Although KAM values are typically lower due to their localized nature, the magnitude of the difference between GOS and KAM is considerable. The KAM distribution shows that the misorientation within individual subgrains is low, while the highest local misorientations (blue lines) appear along subgrain boundaries. This contrast indicates that the larger grains consist of multiple subgrains that have already fragmented during earlier stages of deformation. For small grains, however, both the GOS and KAM maps exhibit quite low and uniform internal orientation gradients (Fig. 39c and d). The absence of pronounced intragranular misorientation in small grains indicates that these grains are fully recrystallized through CDRX.

The combination of high GOS and low KAM values in the larger grains strongly supports the idea that these grains have formed through grain coalescence. During CDRX, the subgrains generated by fragmentation experience a reduction in their internal GND density, resulting in relatively low intragranular misorientation. As deformation proceeds, many of these subgrains rotate toward the same ideal shear orientation, progressively reducing their disorientation. Once the disorientation between adjacent subgrains falls below the grain-detection threshold (5°) used in the EBSD analysis, they are no longer identified as separate grains and appear as a single large grain. This mechanism explains the irregular morphology of the larger grains.

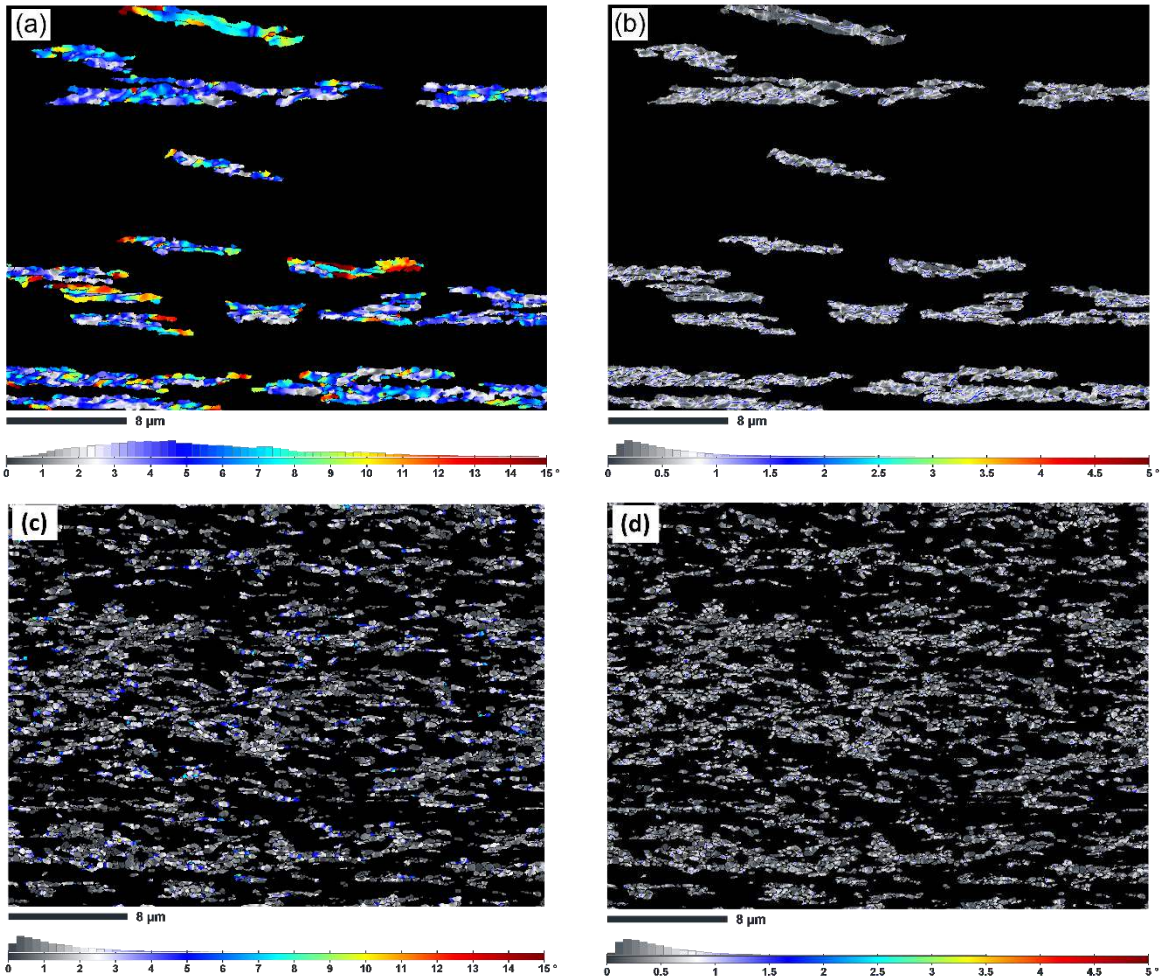

Fig. 39. The average internal misorientation of larger and small grains: **(a)** larger grains GOS map, **(b)** larger grains KAM map, **(c)** small grains GOS map, **(d)** small grains KAM map.

2.3. Theoretical Foundations

2.3.1. Texture Evolution in Shear Deformation

As discussed earlier, grain refinement is strongly governed by the characteristics of texture evolution, which influence both the grain fragmentation and grain coalescence mechanisms. Understanding how orientations rotate during plastic deformation is, therefore, essential for explaining grain refinement. Texture evolution can be examined by analyzing the rotation field of grain orientations in Euler space. This study was conducted by Toth et al. [117] in 1988 for FCC crystals in the torsion test (for positive shear). In the present work, the rotation-field analysis was extended to the case of simple shear with a negative shear sense, which corresponds to the deformation mode in angular channel extrusion processes such as ECAP, NECAP, and FALEP. The velocity gradient for the simple shear deformation in the shear reference system was imposed with $L_{12} = -\dot{\gamma}$ and all other components equal to zero. The φ_2 = 0° section of Euler space was selected, and initial orientations were distributed uniformly

with 5° grid positions in this section. The rotation field vectors were obtained by calculating the lattice rotation rate vector at any point $(\dot{\varphi}_1, \dot{\varphi}, \dot{\varphi}_2)$ and then plotted using the ParaView software [118].

Fig. 40a displays the rotation field in the $\varphi_2 = 0°$ section. The initial orientations are plotted as black points, and the arrows represent the corresponding lattice rotation rate vectors (i.e., velocity vectors in orientation space). The positions of the ideal shear orientations are also indicated on the map. No arrows appear at these ideal orientations because the lattice rotation rate becomes near zero at these points, meaning that the orientations are stable.

As mentioned in Section 1.1.1, the lattice rotation rate $\underline{\dot{\Omega}}$ at any orientation can be expressed as the difference between the rigid body rotation rate $\underline{\dot{\beta}}$ (the rotation of the macroscopic material element) and the plastic spin rate $\underline{\dot{\omega}}$ (the rotation arising from dislocation slips). We recall Eq. (10):

$$\underline{\dot{\Omega}} = \underline{\dot{\beta}} - \underline{\dot{\omega}} \tag{42}$$

Consequently, the rotation field map can be decomposed into the rigid body rotation field and the plastic spin field maps. Fig. 40b illustrates the rigid body rotation field map. As expected, the arrows representing the rigid body rotation vector have identical magnitude and direction for all initial orientations because the rigid body rotation affects the entire material element equally, causing all grains to rotate at the same rate. The plastic spin field map, including the negative sign ($-\underline{\dot{\omega}}$), is shown in Fig. 40c. The plastic spin vectors strongly depend on initial orientation and exhibit significant differences in magnitude and direction across the Euler space. It is evident that at the ideal positions, the plastic spin and rigid body rotation vectors have opposite signs and the same magnitude, meaning they cancel out each other and lead to zero lattice rotation. The maximum lattice rotation is achieved when two vectors are parallel and have the same sign. Another notable feature is that the plastic spin becomes zero near $\varphi = 0°$ and $\varphi = 90°$. In these regions, the lattice rotation is therefore equal to the rigid body rotation, since no compensating plastic spin is generated by slip system activity. These regions in Euler space correspond to the rotated-cube texture, a characteristic orientation for cubic crystal materials subjected to shear deformation. As will be demonstrated in Section 2.4.1, the rotated-cube texture shows a strong tendency to resist rotation toward the ideal shear orientations, making it one of the most stable non-ideal fibers under simple shear deformation. This

resistance has important consequences for the evolution of fragmentation and coalescence during shear deformation.

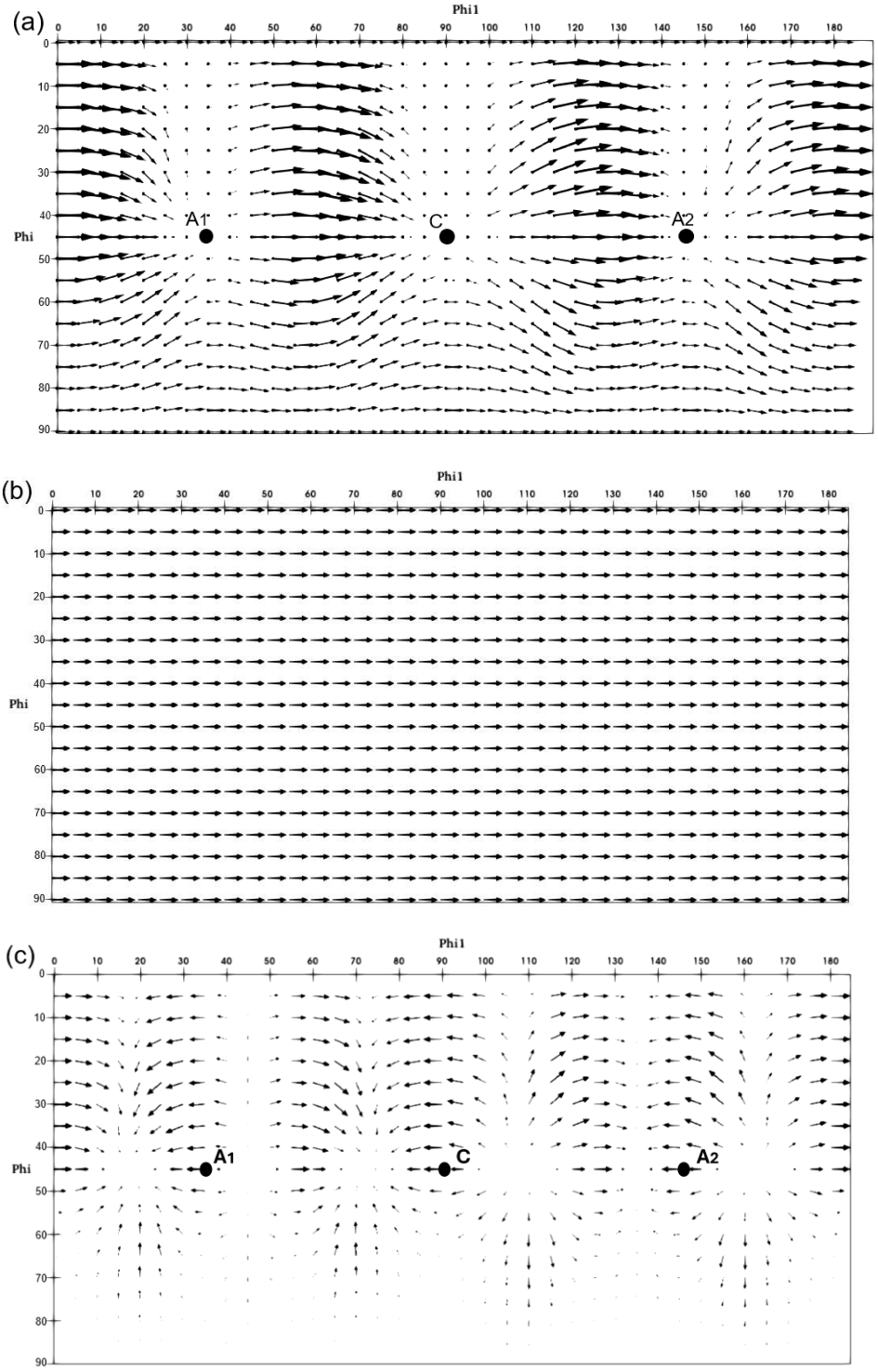

Fig. 40. The rotation field maps for the negative simple shear deformation in the $\varphi_2 = 0°$ section of Euler space: **(a)** the lattice rotation field ($\underline{\dot{\Omega}}$), **(b)** the rigid body rotation field ($\underline{\dot{\beta}}$), **(c)** the negative plastic spin field ($-\underline{\dot{\omega}}$). The shear strain rate is 9 s^{-1}.

The rotation field map clearly indicates that orientation evolution in Euler space is highly non-uniform, with distinct regions where the rotation vectors converge or diverge. To quantify these

features, an isovalue map of the divergence of the rotation field can be used for a better understanding of the nature of orientation evolution. Toth et al. [119] previously examined the divergence values for positive simple shear using an expression based on the partial derivatives of the lattice rotation rates. This equation was later modified in Ref. [120] by including an additional term ($\dot{\varphi}\ cot\ \varphi$), which accounts for the distortion of Euler space. In the present work, we followed the same formulation as Ref. [120], but applied it to the case of negative shear deformation in the shear reference system. The divergence of each orientation is a scalar value, which can be calculated as follows:

$$div\ \dot{R} = \frac{\partial \dot{\varphi}_1}{\partial \varphi_1} + \frac{\partial \dot{\varphi}}{\partial \varphi} + \frac{\partial \dot{\varphi}_2}{\partial \varphi_2} + \dot{\varphi}\cot\varphi \tag{43}$$

The φ_2 = 0° section of Euler space was selected, and the divergence value at points separated by 2° along the φ_1 and ϕ directions was calculated. The divergence map, together with the position of ideal orientations, is presented in Fig. 41. Regions with negative divergence correspond to convergent orientation flow, whereas regions with positive divergence indicate divergent flow. The white contour lines show the locations where divergence is zero. The map displays distinct regions where there are periodic convergence and divergence fields. A unique feature of texture evolution in shear deformation is that all ideal orientations are located at the boundary lines between convergent and divergent regions. It was reported that under the rate-sensitive regime, none of the ideal shear orientations is permanently stable, although the individual grains can remain near the ideal positions over appreciable strains [117]. From the divergence map, it can be concluded that the disorientation between adjacent grains moving in the convergence field progressively decreases. Near the ideal orientations, disorientation can be quite low, allowing grain coalescence. In contrast, small misorientations inside a grain that moves in the divergence field can progressively increase, which facilitates the occurrence of grain fragmentation. Thus, the divergence feature of the rotation field explains why certain orientation paths favor coalescence while others promote fragmentation during shear deformation.

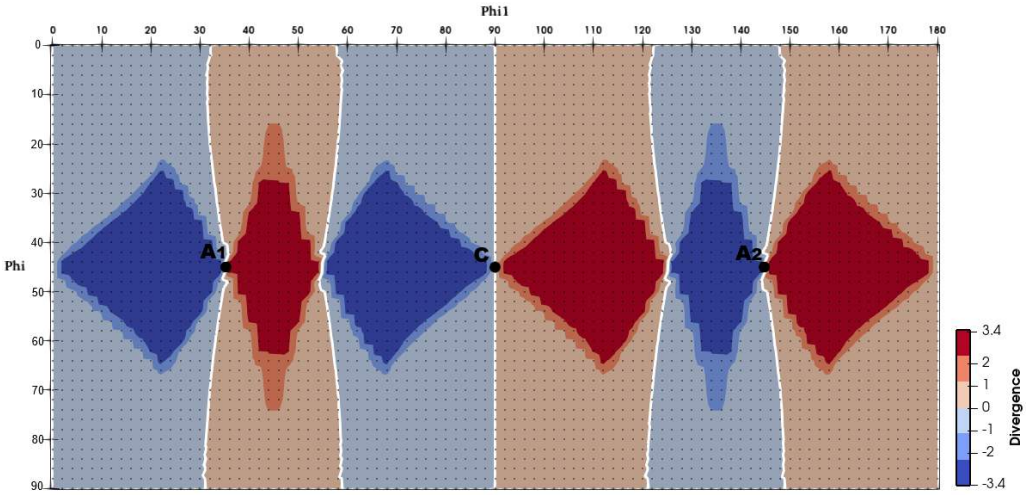

Fig. 41. The isovalue map of the divergence of the rotation field in the $\varphi_2 = 0°$ section of Euler space for the negative simple shear deformation. The negative (blue) and positive (red) divergence values correspond to convergence and divergence, respectively.

The stability of different orientations in Euler space can be examined using the orientation stability parameter [117]:

$$S = \ln\left(\frac{\dot{\bar{\varepsilon}}}{|\dot{\Omega}|}\right) \tag{44}$$

where $\dot{\bar{\varepsilon}}$ is the equivalent von Mises strain rate, and $|\dot{\Omega}|$ is the absolute value of the lattice rotation rate. Higher values of S indicate that the given orientation is more stable during deformation. Therefore, the ideal shear orientations are expected to show the highest stability values. Fig. 42 displays the orientation stability map for the simple shear deformation in the $\varphi_2 = 0°$ section of Euler space, calculated on a 2° grid. The highest S values correspond to the ideal shear orientations, with a maximum for the C component, indicating its particularly strong resistance to rotation during shear. In the vicinity of the ideal positions, grain orientations remain stable over substantial strains. However, this stability is not permanent. With further straining, grains can eventually escape the ideal positions in the orientation space once the plastic spin is not high enough to compensate for the rigid body rotation.

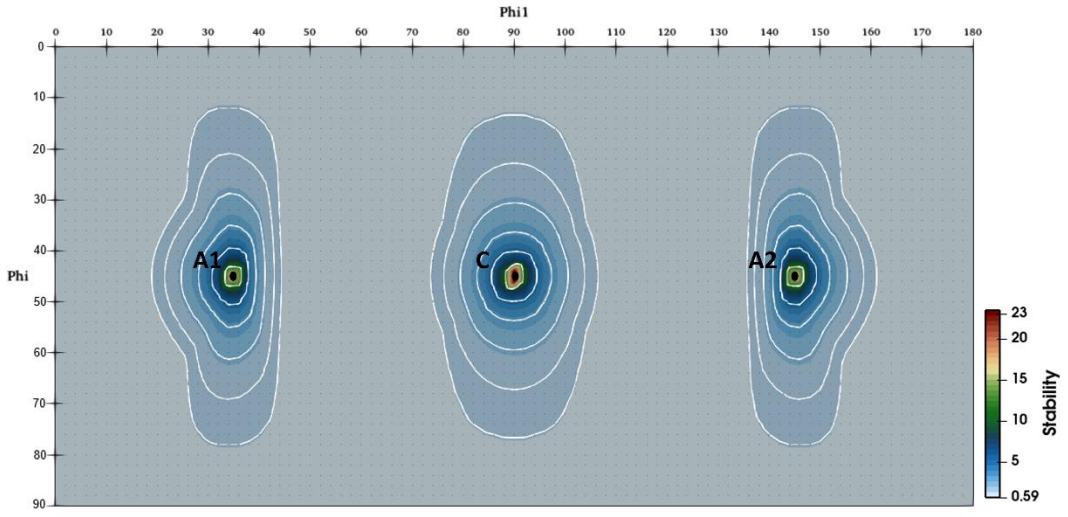

Fig. 42. The orientation stability map in the $\varphi_2 = 0°$ section of Euler space for the negative simple shear deformation.

In addition to the convergent and divergent features of the rotation field, the orientation stability parameter also plays a crucial role in governing the mechanisms of grain fragmentation and coalescence. While regions with negative divergence (convergent flow) promote coalescence by gradually reducing the disorientation between adjacent grains, such convergent regions are relatively extended across orientation space. However, experimental observations show that the larger grains formed by coalescence are near the ideal orientations rather than distributed across all regions of high convergence. This trend can be explained by considering the combined effects of the convergence field and orientation stability. As an orientation cloud, corresponding to a group of neighboring grains, moves through a convergence field of the orientation space, the front part of the cloud reaches the ideal orientation first and tends to remain there because of the high stability of the ideal shear components. Meanwhile, the back part of the orientation cloud continues to move toward the same ideal position and merge with the front part, resulting in grain coalescence and the formation of a larger grain with the ideal orientation. This process explains why experimentally observed coalesced grains form specifically near the ideal shear orientations, even though convergence exists in other parts of Euler space as well.

It is expected that grain coalescence takes place when considerable grain fragmentation has already occurred in the microstructure. It is also obvious that coalescence can occur only between grains that share a common grain boundary, meaning they are neighbors in physical space. Moreover, the neighboring grains that have large orientation differences are not suitable candidates for grain coalescence. Therefore, the neighboring condition should also exist in the orientation space, meaning that the disorientation between the grains is not too sharp. Finally,

coalescence is possible only near the ideal shear orientations, where the rotation field is convergent, and the lattice rotation rate becomes small.

Therefore, grain coalescence can occur only when all the following conditions are satisfied:

- Prior grain fragmentation
- Neighboring in physical space
- Neighboring in orientation space
- Approaching the ideal positions in orientation space

Continuous dynamic recrystallization (CDRX) inherently fulfills the first three conditions as the fragmented grains are physically adjacent and their orientations remain correlated with the parent grain orientation, meaning they are also neighbors in the orientation space. Coalescence is therefore activated only when the fourth condition is reached, i.e., when the grains enter a convergent texture field and reach near the ideal positions. This demonstrates that grain coalescence is an intrinsic stage of the CDRX mechanism, driven fundamentally by the nature of texture evolution during plastic deformation.

2.3.2. Principles of the 4-Level Grain Refinement Model

The grain refinement model introduced in Ref. [110] has been further developed and applied in the present study to simulate the mechanisms of grain fragmentation and coalescence. Fig. 43 presents a two-dimensional schematic of lattice curvature near grain boundary regions, projected along the lattice rotation vector. The initially undistorted lattice plane is depicted as a straight line. In the central region of the grain, where the lattice rotation is not influenced by boundary constraints, the lattice rotation is equal to the imposed lattice rotation of Ω_G. In the grain boundary zone, however, the lattice plane becomes curved, and the intersection with the grain boundary shifts from point B to point C. The angle between AC and AB segments is denoted by $\mu\Omega_G$. As discussed previously, μ is the key parameter of the model that governs the degree of lattice curvature, with its value ranging between 0 and 1.

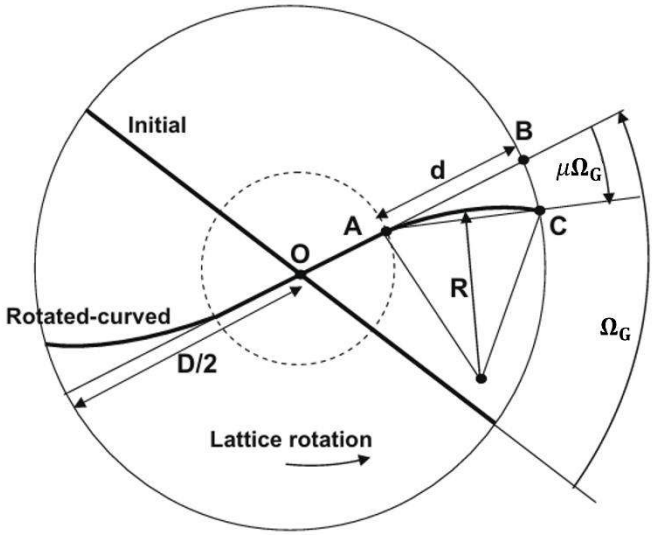

Fig. 43. 2D schematic illustration of lattice curvature near grain boundary regions. The projection direction is parallel to the lattice rotation vector [110].

By considering equal size between the grain boundary zone and the middle zone, the geometric configuration of a grain becomes identical to a Rubik cube in 3D, as shown in Fig. 31. In this model, the grain boundary zone is treated as a subgrain. The number of grain boundaries for each subgrain can be 1, 2, or 3. In this case, the "resultant grain boundary normal" for each subgrain is defined by:

$$\underline{n}_{GB}^{(res)} = \sum_{i=1}^{k} \underline{n}_{GB}^{(i)}, \quad k = 1, 2, or\ 3 \tag{45}$$

The rotation distortion induced by all grain boundaries of a given element (subgrain) is represented by the rotation around the resultant grain boundary normal of that element. Accordingly, the portion of the lattice rotation rate that arises from grain boundary effects is expressed as:

$$\dot{\underline{\Omega}}_{SG}^{GB} = -sign\left[\dot{\underline{\Omega}}_G \underline{n}_{GB}^{(res)}\right] |\sin\alpha| \left|\mu\dot{\underline{\Omega}}_G\right| \frac{\underline{n}_{GB}^{(res)}}{\left|\underline{n}_{GB}^{(res)}\right|} \tag{46}$$

Here, α is the angle between the resultant grain boundary normal of the subgrain $\underline{n}_{GB}^{(res)}$ and the lattice rotation rate vector of the parent grain $\dot{\underline{\Omega}}_G$. During plastic deformation, this angle evolves because the directions of both vectors change continuously. The grain boundary induced lattice rotation rate of the subgrain $\dot{\underline{\Omega}}_{SG}^{GB}$ is then superimposed on the lattice rotation rate of the parent grain. The overall lattice rotation rate of the subgrain is thus:

$$\dot{\underline{\Omega}}_{SG} = \dot{\underline{\Omega}}_{G} + \dot{\underline{\Omega}}_{SG}^{GB} \tag{47}$$

From Eq. (47), the orientation of the subgrains can be updated during plastic deformation in each strain increment and at each fragmentation level. Once the orientation difference of a subgrain and the center element exceeds a critical misorientation value of 5°, the subgrain is treated as a new parent grain, and the next level of fragmentation is initiated for that. In the current study, a 4-level grain refinement scheme is employed. Under this configuration, the maximum number of possible subdivisions originating from a single initial grain is $27 \times 27 \times 27 \times 27 = 531441$. A schematic representation of the 4-level grain refinement approach is shown in Fig. 44. The smallest element (the white cube) corresponds to a voxel, which represents the minimum attainable grain size in this configuration. To each voxel, the position coordinates (x, y, and z) and a set of Euler angles (φ_1, ϕ, and φ_2) are assigned. In this way, the geometrically neighboring conditions and misorientation variations, which are necessary for analyzing grain fragmentation and coalescence, can be investigated at the voxel level.

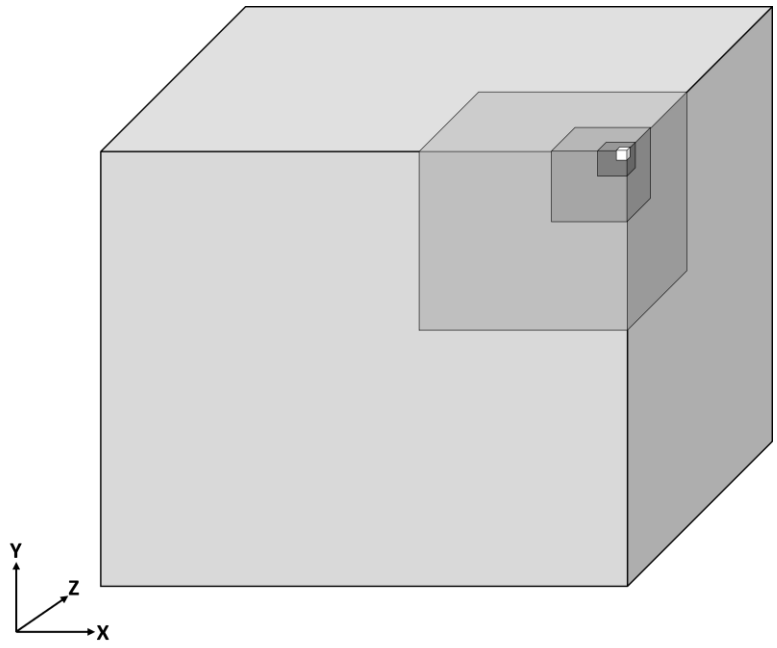

Fig. 44. Schematic of the 4-level grain fragmentation approach. The small white cube is the minimum attainable grain size (voxel). For better visualization, the sub-cubes' sizes relative to the parent cube are enlarged.

In this model, the fractal approach implies that grain fragmentation proceeds level by level, from the first level up to the fourth. At each level, the grain is subdivided into 27 elements. If a parent element at level i has not fragmented, meaning that its orientation difference relative to the center element at the same level remains below the critical misorientation of 5°, then all 27 corresponding elements at level $i+1$ inherit the same orientation. In the fractal geometry

applied here, each voxel is uniquely identified by four ID numbers, corresponding to the four possible fragmentation levels, with each ID ranging from 1 to 27. A customized indexing scheme is used to assign these identifiers to the 27 elements at each level; a schematic representation of this method is shown in Fig. 45.

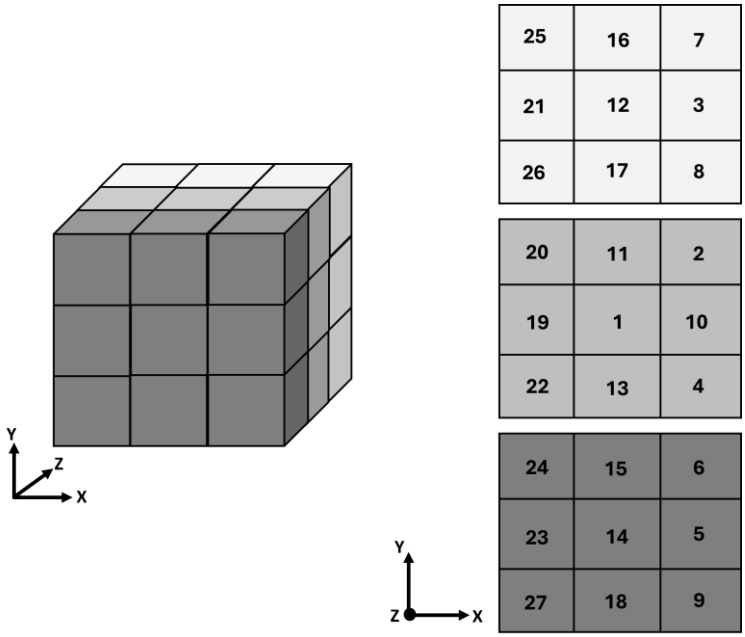

Fig. 45. The implemented indexing order for 27 elements at each subdivision level.

At each level, three-digit numbers corresponding to the x-y-z coordinates are assigned to the center of each element. By considering the zero coordinates reference for the center element, the possible coordinate values in each direction are -1, 0, or 1. Accordingly, the spatial coordinates of the center point of individual voxels can be calculated as follows:

$$x = 27.x_{c1} + 9.x_{c2} + 3.x_{c3} + x_{c4} + 41 \quad (48a)$$

$$y = 27.y_{c1} + 9.y_{c2} + 3.y_{c3} + y_{c4} + 41 \quad (48b)$$

$$z = 27.z_{c1} + 9.z_{c2} + 3.z_{c3} + z_{c4} + 41 \quad (48c)$$

where c1 to c4 correspond to the first through fourth levels of fragmentation. Using this convention, the coordinates of the white voxel shown in Fig. 44 are x = 81, y =81, and z = 1.

The presented technique allows for assigning a unique set of coordinates to each of the 531,441 voxels. It is then possible to evaluate neighboring conditions at the voxel level, which is essential for accurately analyzing grain size evolution during plastic deformation. To achieve this, a 3D flooding grain detection algorithm was incorporated into the original grain

fragmentation program. A 6-neighbor connectivity scheme (shared voxel facets) was used for identifying grain boundaries. The critical misorientation angle, above which a boundary is detected, was set to 5°. The algorithm starts with an initial voxel and examines the misorientation between that voxel and its six adjacent voxels. If the misorientation of a candidate voxel relative to any adjacent voxel already belonging to a grain is less than the critical value, the candidate voxel is added to that grain. Otherwise, the candidate voxel is considered a new grain, and the same scanning procedure is applied to that. Through this approach, it becomes possible to determine both the number of grains and the average grain size in 3D at each strain increment during deformation. Subsequently, the equivalent spherical diameter of a detected grain is calculated as:

$$d_i = \sqrt[3]{\frac{6 \, . \, V_i}{\pi}} \tag{49}$$

where V_i is the volume of grain *i*, determined from the number of voxels associated with that grain. The volume-weighted average grain size (d_v) in 3D is therefore given by:

$$d_v = \frac{\sum_{i=1}^{N} d_i \, . \, V_i}{\sum_{i=1}^{N} V_i} \tag{50}$$

Nevertheless, the majority of grain size measurements obtained from characterization techniques such as EBSD are evaluated in 2D rather than 3D due to practical limitations in three-dimensional grain reconstruction. Therefore, a 2D flooding grain detection algorithm was also implemented to estimate grain sizes on planar sections. In this approach, the 2D grain detection is performed on all 81 sections along the z-direction, where each voxel is represented as a 2D pixel. For boundary identification, a 4-neighbor connectivity criterion (shared pixel edges) was applied, and the same scanning logic used in the 3D flooding algorithm was employed to detect grain boundaries in 2D. The equivalent circular diameter of a grain in 2D is defined as:

$$d_i = \sqrt[2]{\frac{4 \, . \, A_i}{\pi}} \tag{51}$$

where A_i is the area of grain *i*. The area-weighted average grain size on each 2D section along the z-direction is:

$$d_a = \frac{\sum_{i=1}^{N} d_i \,.\, A_i}{\sum_{i=1}^{N} A_i} \tag{52}$$

The overall area-weighted average grain size is then obtained by averaging the area-weighted grain sizes calculated on all 81 sections.

It is noteworthy that the 2D grain size estimation systematically yields smaller grain sizes than the corresponding 3D grain size calculation. For a single cubic grain, the 2D/3D grain size ratio is approximately 0.9, meaning that the above formulas, which are frequently used in various studies, result in a smaller 2D grain size compared to the true 3D grain size. More importantly, 2D grain size measurements ignore possible connections between neighboring grains in the third dimension. It is reasonable to assume that some of the closed boundary loops detected in an EBSD map are not actually closed in three dimensions. In such cases, the two regions located on either side of the apparent boundary would belong to the same grain when evaluated in 3D. Although several 3D EBSD characterization techniques have been proposed [121, 122], their practical feasibility remains limited due to experimental complexity, serial sectioning challenges, and data reconstruction constraints. The proposed model, however, can be used to evaluate how the grain size estimations vary when obtained in 2D versus 3D. In the next section, this issue is examined by analyzing grain refinement simulation results.

The geometrical configuration of the proposed model permits evaluating the number of fragmented and coalesced boundaries at the voxel level. The approach is based on calculating the orientation difference between neighboring voxels at each strain increment and comparing it with the corresponding value at the previous increment. Under these conditions, four possible transition states can occur between two adjacent voxels during a strain increment:

A) Fragmentation: the orientation difference between the two voxels was below the critical misorientation at the previous increment and exceeded the critical value at the new increment.

B) Coalescence: the orientation difference was above the critical misorientation at the previous increment and fell below the critical value at the new increment.

C) No change in state: the orientation difference remained below the critical misorientation angle.

D) No change in state: the orientation difference remained above the critical misorientation angle.

These four evolution states can be quantified directly using the 4-level grain refinement model, providing detailed insight into the interactions between grain fragmentation and coalescence during deformation. The rotation field analysis indicates that fragmentation events are likely to occur in the divergence field, while coalescence events are promoted in regions where the rotation field converges toward the ideal shear orientations.

2.4. Polycrystal Plasticity Simulations

2.4.1. Never Passing Ideal Shear Positions

The divergence field map for simple shear deformation (Fig. 41) revealed that convergent and divergent regions are most pronounced in the vicinity of the ideal shear orientations. As a result, orientation evolution near these positions is strongly governed by the imposed rotation field. It is therefore of interest to evaluate the tendency of different orientations to rotate toward the ideal shear positions. To this end, crystal plasticity simulations without incorporating grain refinement were performed. The Taylor model with a viscosity parameter of $1/m = 8$ was employed under the simple shear deformation up to an equivalent von Mises strain of 20. This approach allows examination of intrinsic orientation stability and rotation behavior, independent of fragmentation and coalescence mechanisms. The $\varphi_2 = 0°$ and 45° sections, which contain all ideal shear components, were selected for this analysis. Initial orientations were uniformly distributed in these sections at 2° intervals. The regions with $|\dot{\Omega}| < 0.1|\dot{\Omega}_{max}|$ were considered the ideal shear positions, where the absolute lattice rotation rate is small, and the orientation stability is high. Fig. 46a and c illustrate the initial orientations of grains that never pass through the ideal shear positions during deformation up to $\varepsilon_{eq} = 20$. The fraction of such grains is remarkably high: about 60 % in the $\varphi_2 = 0°$ section, and nearly 25 % in the $\varphi_2 = 45°$ section. The lower fraction of these grains in the $\varphi_2 = 45°$ section is due to the more extended regions corresponding to ideal shear orientations in this section of Euler space.

In reality, however, a smaller fraction of grains is expected to never reach the ideal positions. This is because CDRX introduces internal misorientations and orientation fluctuations within grains, promoting deviations in Euler space and increasing the chance that grains enter convergent rotation fields and migrate toward the ideal shear orientations. Nevertheless, the rotated-cube fiber represents an extreme case among orientations that resist rotation toward the ideal shear components, as it is located far from the ideal positions in Euler space. The corresponding final orientations of these grains after $\varepsilon_{eq} = 20$ are presented in Fig. 46b and d. Notably, the intensity of the rotated-cube fiber remains relatively high, even during very large

deformation (ε_{eq} = 20). Although the rotated-cube fiber is not an ideal shear fiber, it exhibits a certain degree of relative stability under simple shear deformation. It should be emphasized that no individual orientation along the rotated-cube fiber is stable, as the stability remains low due to the dominant contribution of the rigid body rotation. However, when the whole fiber is considered, a form of relative stability appears, since the orientation evolution is restricted to occur along this fiber, rather than diverging toward other regions of Euler space. Near the rotated-cube fiber, the effect of the imposed divergence and convergence fields is minimal. As a result, no significant deviation in the lattice rotation vectors occurs, and orientations evolve in a relatively narrow zone in Euler space. This mechanism allows the rotated-cube fiber to remain semi-stable during shear deformation, though the stability parameter is quite low in this region due to the high rigid body rotation rate of shear deformation. Another unique feature of the rotated-cube fiber in shear deformation is that its evolution is independent of the strain rate sensitivity of materials. On the exact ϕ = 0° plane, the plastic spin is zero, and the lattice rotation is equal to the rigid body rotation (Eq. (42)). Considering that the strain rate sensitivity does not affect rigid body rotation, the orientation evolution on the ϕ = 0° plane (rotated-cube fiber) remains independent of strain rate sensitivity. It is not, however, the same case for other orientations, especially ideal shear components. As the strain rate sensitivity increases, the stability of the ideal shear components decreases [117].

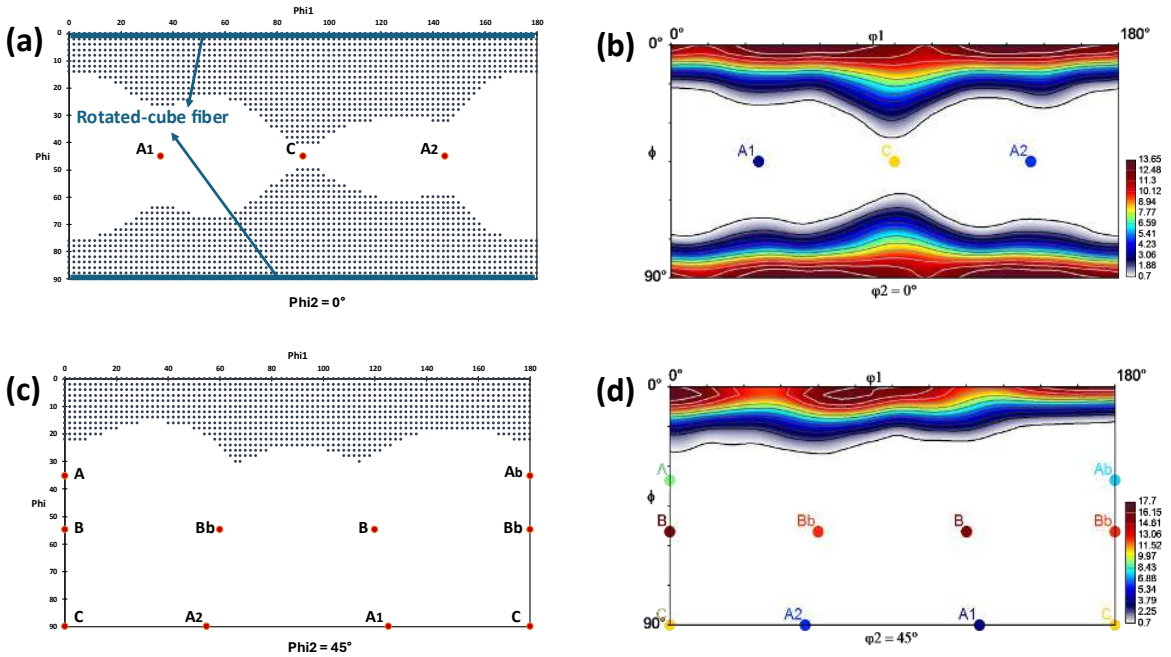

Fig. 46. The initial orientation (black points) of grains never passing through the ideal shear positions during deformation up to ε_{eq} = 20 at **(a)** φ_2 = 0° and **(c)** φ_2 = 45° ODF sections. **(b)** and **(d)** the corresponding final orientations of **(a)** and **(c)** at ε_{eq} = 20, respectively.

2.4.2. Grain Refinement

The 4-level grain refinement model has been employed to simulate the evolution of the grain structure during simple shear deformation. Three different initial orientations were selected for analysis, and their corresponding Euler angles are listed in Table 3. Each orientation was assigned an identical initial volume fraction, meaning that the starting 2D and 3D grain sizes were the same for all cases. For polycrystal plasticity calculations, the Taylor model was used, with the only non-zero velocity gradient component of $L_{12} = -\dot{\gamma}$, corresponding to the negative simple shear in the shear reference system. For all simulations, the 12 $\{\bar{1}\ 11\}\langle 110\rangle$ slip systems were used with the slip-viscosity parameter of *1/m* = 8. The lattice curvature coefficient (μ) was set to 0.5 in all following simulations.

Table 3. The Euler angles and grain sizes of three initial grains used in the grain refinement simulation.

Grain ID	Euler angles (°)			Volume fraction	Grain size 2D (μm)	Grain size 3D (μm)
	φ_1	Φ	φ_2			
Grain A	5	45	0			
Grain B	95	45	0	14420	27.46	30.19
Grain C	0	0	0			

Fig. 47 presents the 2D and 3D grain size evolution of Grain A during the deformation up to an equivalent strain of 4.61 (shear strain of 8). The volume-weighted average grain size significantly decreased from 30.19 μm to 9.1 μm up to ε_{eq} = 3.6 through successive grain fragmentation events. Interestingly, upon further deformation, the average 3D grain size remarkably increases to 21.14 μm at an equivalent strain of 4.61. This increase indicates that grain coalescence becomes dominant beyond a strain of approximately 3.6, demonstrating that coalescence plays a significant role in the grain refinement behavior of Grain A at higher strains. A similar trend can be observed in the evolution of 2D grain size. The smallest area-weighted average grain size of 5.2 μm is achieved at ε_{eq} = 4, after which the grain size increases to 9 μm at ε_{eq} = 4.61. However, the 2D grain size results exhibit a sharp drop in grain size at a strain of 0.37, followed by a gradual increase up to ε_{eq} = 1. This fluctuation is absent in the 3D grain size evolution diagram. As noted earlier, the 3D grain detection method yields larger grain sizes because grain connections in the third dimension are considered. As a result, no significant grain fragmentation is detected at a relatively low strain of 0.37 using 3D grain

detection. Without sufficient fragmentation at this early stage, grain coalescence cannot occur, since prior fragmentation is a fundamental requirement for coalescence.

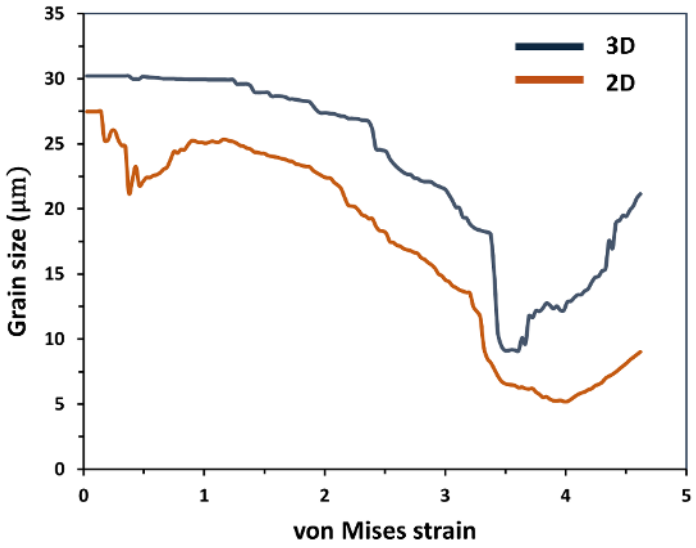

Fig. 47. The 2D and 3D grain size evolutions of Grain A simulation during simple shear deformation up to ε_{eq} = 4.61.

Fig. 48 depicts the evolution of the normalized number of fragmented and coalesced boundaries at the voxel level as a function of strain. The number of fragmented boundaries shows a decreasing trend beyond ε_{eq} = 4, indicating a gradual reduction in new boundary formation at high strain. In contrast, the number of coalesced boundaries shows an increasing trend from a strain of 2 to the final strain of 4.61. At the final deformation increment, the number of coalesced boundaries exceeds the number of fragmented boundaries by a factor of approximately four, meaning that grain coalescence becomes the dominant mechanism at this stage of deformation.

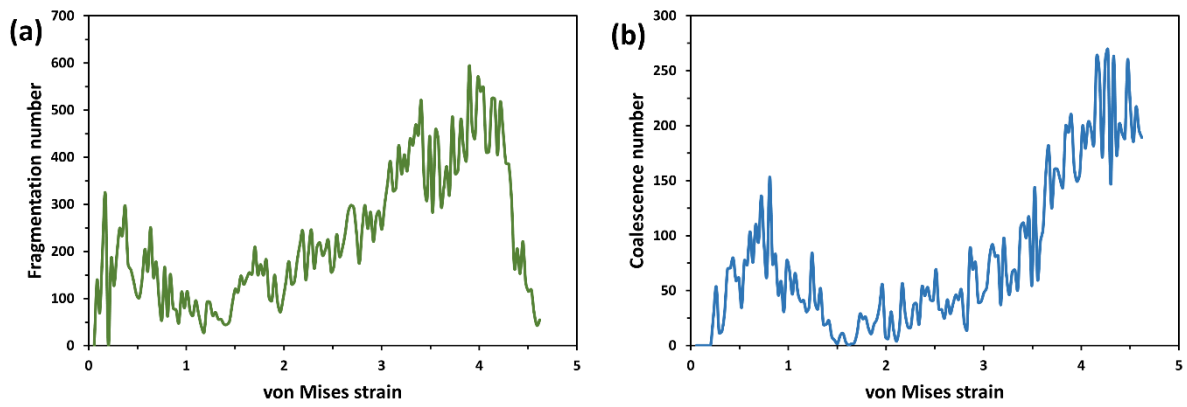

Fig. 48. The evolution of the number of **(a)** fragmented and **(b)** coalesced boundaries between neighboring voxels of Grain A during simple shear deformation up to ε_{eq} = 4.61.

To evaluate the statistical grain size distribution, the final strain increment was used, and 2D grain sizes were calculated for all 81 sections along the z-direction. Fig. 49 displays the number fraction and the area fraction grain size distributions for Grain A at ε_{eq} = 4.61. The number fraction grain size distribution shows a sharp peak at very small grain sizes, indicating that a large population of grains reached the final fragmentation level. For better visualization, the distribution of larger grains (above 4 µm) is shown in an enlarged view. Because the small grains vastly outnumber the larger ones, the number fraction distribution appears unimodal, dominated by the fine grains' population. In contrast, the area fraction distribution (Fig. 49b) provides a more comprehensive representation of the overall microstructure, as it accounts for the large area occupied by the larger grains. When plotted in terms of area fraction, the grain size distribution becomes broader and more uniform, reflecting the coexistence of numerous fine grains and fewer large grains.

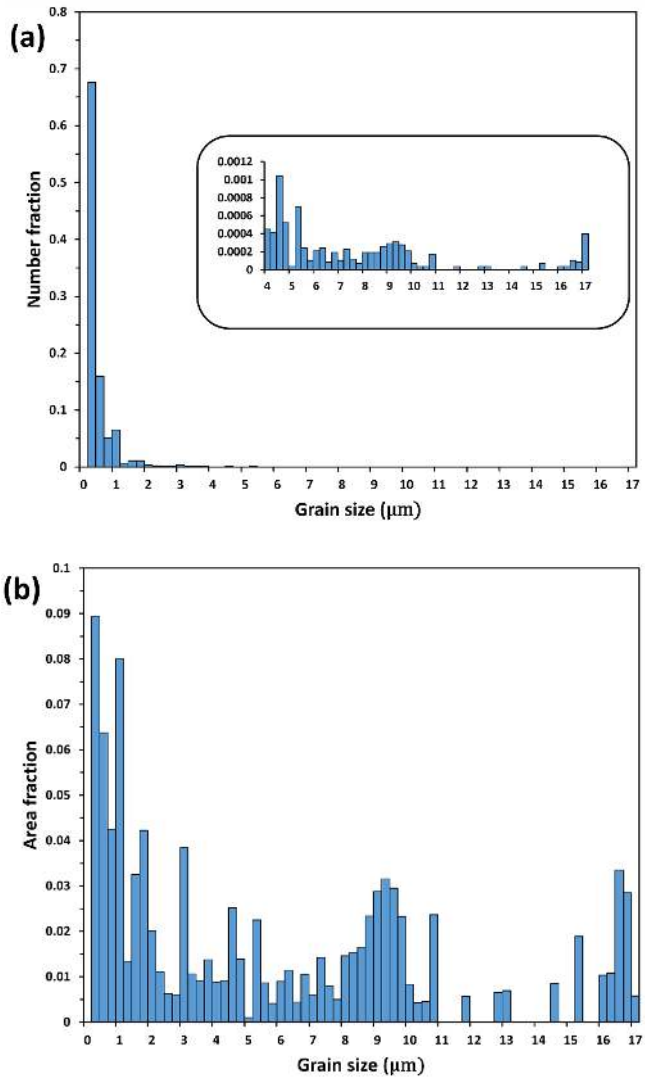

Fig. 49. (a) The number fraction and **(b)** the area fraction grain size distributions of Grain A at ε_{eq} = 4.61 obtained from all 2D sections along the z-direction (bin size = 0.25 µm).

Another important output of the present model is the crystallographic texture. To evaluate the influence of texture evolution on the fragmentation and coalescence behavior of Grain A, two deformation stages were examined: $\varepsilon_{eq} = 4$ (Fig. 50a), where the fragmentation rate has begun to decrease, and $\varepsilon_{eq} = 4.61$ (Fig. 50b), where significant grain coalescence has occurred. The $\varphi_2 = 0°$ and 45° sections of Euler space are presented, as these contain all ideal shear components. At $\varepsilon_{eq} = 4$, two distinct orientation clouds are observed: one located after the A1 component and another with a higher intensity before the C component. When the strain increases to 4.61, the two orientation clouds merge and form a single cloud with a very high intensity at the ideal C orientation. For negative shear, the orientation evolution proceeds in the direction of increasing φ_1. In this case, the front cloud moves into the convergence field before the C position and reaches this ideal position, where the lattice rotation rate becomes very small, and the orientation cloud is effectively stabilized. Meanwhile, the back cloud moves through the narrow divergence field located after the A1 position and subsequently enters the convergence field before the C component. Finally, the back cloud joins the front one at the ideal C position, generating a single orientation cloud with a high intensity. As a result, the disorientation between adjacent grains decreases, and larger grains form through grain coalescence, leading to an increase in the average grain size observed at the higher strain. The texture analysis clearly confirms the theory of grain coalescence at the ideal orientations driven by the convergent rotation field.

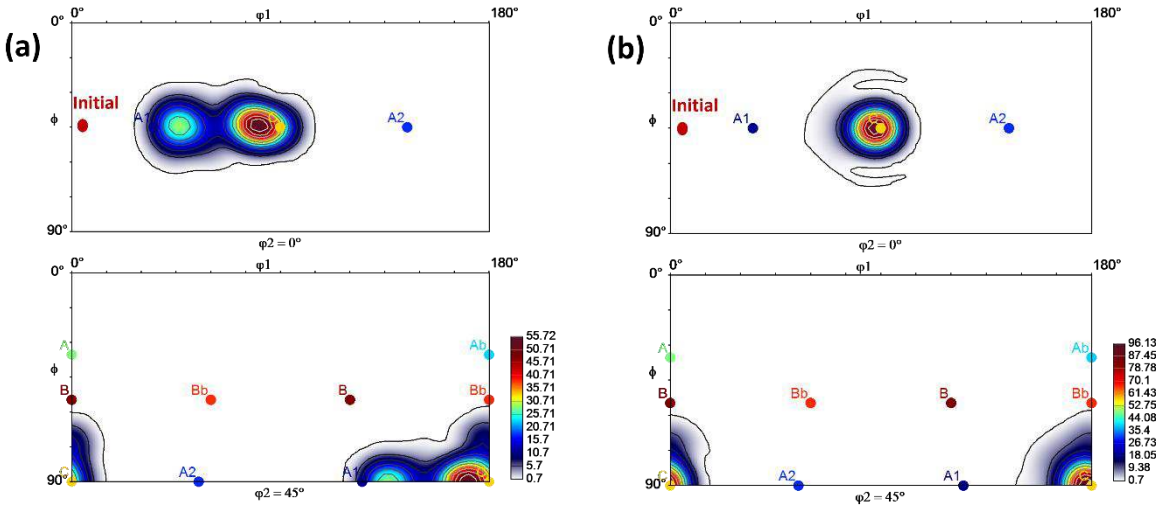

Fig. 50. $\varphi_2 = 0°$ and 45° ODF sections of the simulated textures of Grain A at **(a)** $\varepsilon_{eq} = 4$, and **(b)** $\varepsilon_{eq} = 4.61$.

The next-neighbor disorientation distribution of Grain A after an equivalent strain of 4.61 is presented in Fig. 51. To calculate the next-neighbor disorientation distribution, all 2D sections along the z-direction were evaluated. The representative orientation of each grain was calculated by averaging the orientation of all voxels belonging to that grain. Then, the

orientation differences between neighboring grains were determined and plotted using a bin size of 1°. A pronounced deviation from the random Mackenzie distribution (solid black line) can be observed with sharp peaks at low disorientation angles, particularly between 5° and 20°. At this deformation stage, a strong texture around the ideal C orientation is developed. Consequently, the disorientation between the grains with nearly similar orientation is decreased, and strong peaks appear at lower disorientation angles. This behavior demonstrates that grain coalescence contributes to a systematic shift of the disorientation distribution toward lower angles.

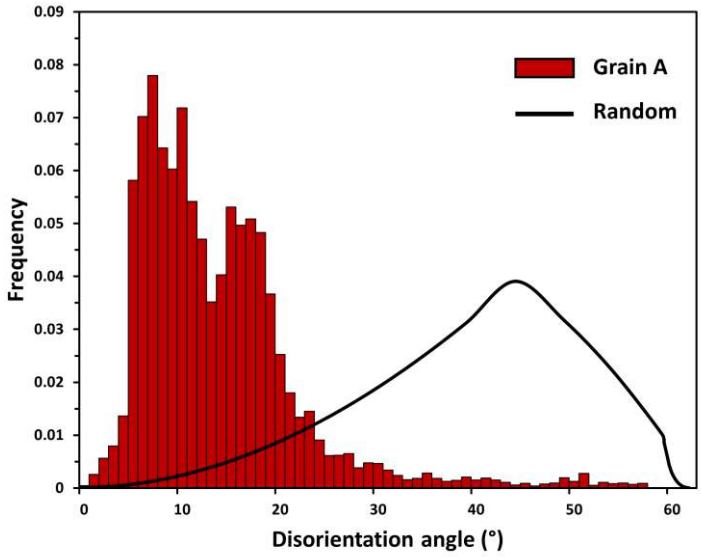

Fig. 51. The next-neighbor disorientation distribution of Grain A at $\varepsilon_{eq} = 4.61$ obtained from all 2D sections along the z-direction (bin size = 1°). The black line shows the random Mackenzie distribution.

In the proposed model, each voxel is assigned a unique set of Euler angles and spatial coordinates, enabling the reconstruction and visualization of the simulated microstructure on any 2D section of the full 3D configuration. For comparison with the texture and grain size evolution results, a constant z-section was selected at two deformation stages: $\varepsilon_{eq} = 4$ and $\varepsilon_{eq} = 4.61$. The corresponding virtual microstructures, plotted using the ATEX software, are shown in Fig. 52. After deformation to $\varepsilon_{eq} = 4.61$, distinct regions where grain coalescence occurred, can be observed. Analyzing the ideal shear orientations within these regions reveals a transition from the A1 component to the C component within the coalesced grains. This evolution is consistent with the texture simulation results, which also show the merging of the two orientation clouds into a single cluster at the ideal C orientation at $\varepsilon_{eq} = 4.61$.

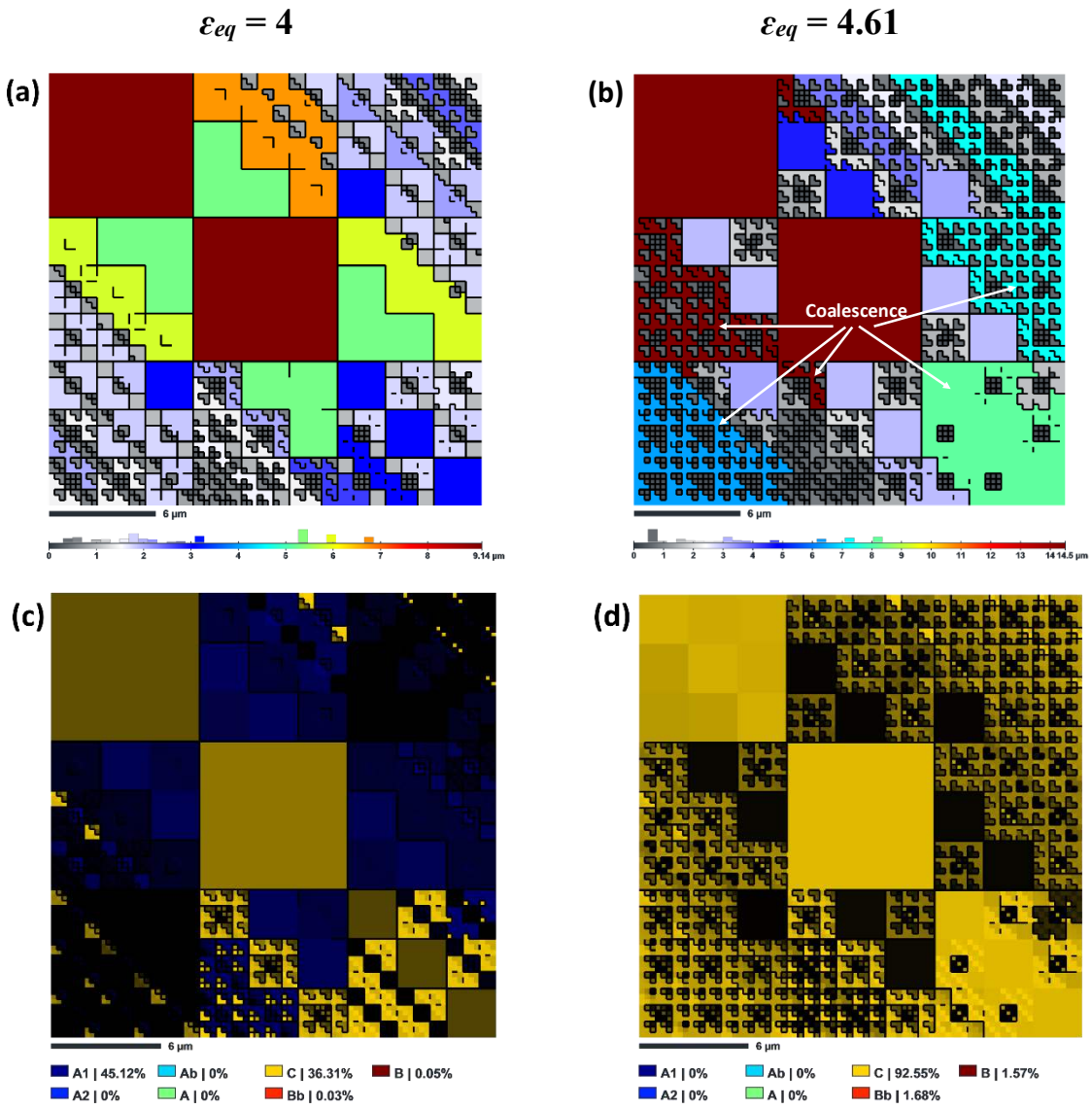

Fig. 52. The simulated microstructure of Grain A projected on a constant z-section for **(a)** $\varepsilon_{eq} = 4$, and **(b)** $\varepsilon_{eq} = 4.61$ (coloring is based on the grain size). The corresponding ideal orientations map for **(c)** $\varepsilon_{eq} = 4$, and **(d)** $\varepsilon_{eq} = 4.61$ (coloring is based on the ideal shear components).

The grain size evolution of Grain B during deformation up to $\varepsilon_{eq} = 4.61$ is shown in Fig. 53. The 3D grain size evolution exhibits a sharp decrease at $\varepsilon_{eq} = 0.8$, followed by a rapid increase in grain size at $\varepsilon_{eq} = 0.9$. The 2D grain size curve also shows a pronounced reduction in grain size at low strains. However, the extent of coalescence captured in the 2D analysis is less significant than in the 3D case, resulting in a sharp difference in grain size between the two representations near $\varepsilon_{eq} = 1$. By further straining up to $\varepsilon_{eq} = 4.61$, both the 2D and 3D analyses show a continuous decrease in grain size. At higher strain levels, limited grain coalescence occurs and acts as a compensation mechanism for grain fragmentation, locally reducing the rate of grain size decline. Unlike Grain A, however, no considerable grain size increase is

observed for Grain B at high strains. This indicates that grain coalescence has a limited influence on Grain B, and grain fragmentation remains the dominant mechanism throughout the deformation. Consequently, both 2D and 3D grain sizes continue to decrease and ultimately become very similar at the final deformation stage, indicating that a uniform microstructure forms in Grain B in all spatial directions due to extensive fragmentation. As all simulation parameters were identical for Grains A and B, the significantly different grain size evolutions arise primarily from their different initial orientations. For a given strain, different orientations follow distinct trajectories in Euler space, where the convergence and divergence rotation fields, together with the lattice rotation rate, govern the extent of fragmentation and coalescence and therefore the final grain size.

Grain B is initially located in the divergence field after the ideal C orientation. At early deformation stages, Grain B passes through this divergence field, promoting grain fragmentation. The sharp drop in 3D grain size at low strain suggests that several elements have been fragmented at the first level of refinement. Following that, the fragmented subgrains enter a convergent region located before the ideal A2 orientation. As a result, their disorientation falls below the critical 5° angle due to grain coalescence. Further straining enables the subgrains of Grain B to leave the ideal A2 position via lattice rotation and enter the well-extended divergent region after this ideal component, leading to increased disorientation and promoting grain fragmentation.

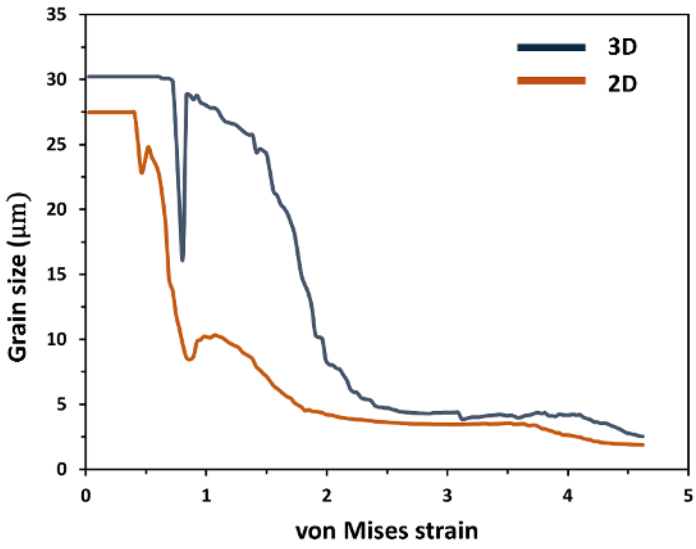

Fig. 53. The 2D and 3D grain size evolutions of Grain B simulation during simple shear deformation up to ε_{eq} = 4.61.

The normalized number of fragmented and coalesced boundaries between each voxel pair for Grain B is presented in Fig. 54. A pronounced peak close to $\varepsilon_{eq} \approx 1$ appears in both fragmentation and coalescence curves, corresponding directly to the strong decrease and subsequent increase in the 3D grain size observed in Fig. 53. Throughout most of the deformation, the number of fragmented boundaries significantly exceeds the number of coalesced boundaries, indicating that fragmentation dominates the microstructural evolution of Grain B. An exception occurs near $\varepsilon_{eq} \approx 3.5$, where the number of coalesced boundaries slightly exceeds the fragmented ones. This local increase in coalescence corresponds to the slight increase in grain size observed in the 3D analysis curve. With further straining, however, the number of fragmented boundaries again becomes dominant, confirming that grain fragmentation remains the primary mechanism controlling grain refinement in Grain B.

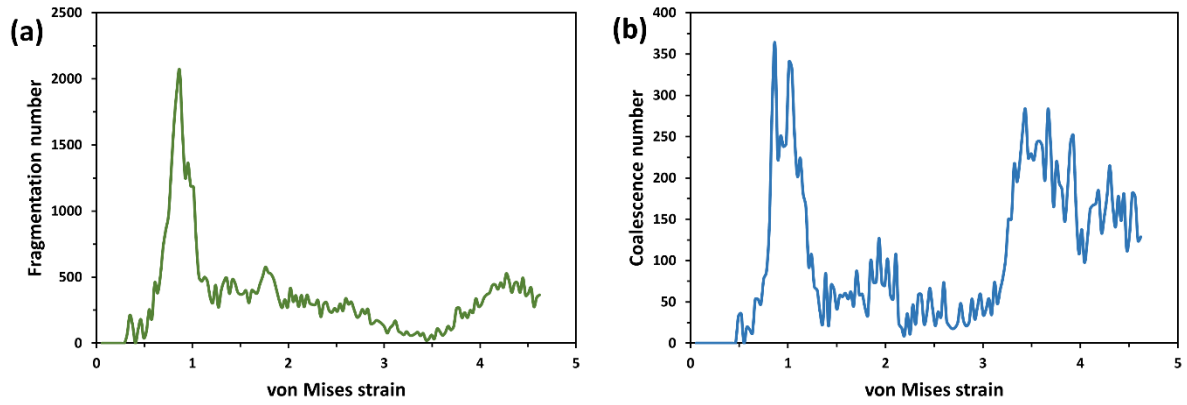

Fig. 54. The evolution of the number of **(a)** fragmented and **(b)** coalesced boundaries between neighboring voxels of Grain B during simple shear deformation up to $\varepsilon_{eq} = 4.61$.

The number fraction and area fraction grain size distributions of Grain B after $\varepsilon_{eq} = 4.61$ are shown in Fig. 55. The number fraction distribution shows a very strong peak at grain sizes below 0.5 µm. The intensity of this peak is even higher than that of Grain A (Fig. 49a). The frequency of larger grains (above 4 µm) is also much lower for Grain B compared to Grain A. Furthermore, the maximum 2D grain size detected in Grain B is approximately 11 µm, whereas Grain A contains grains exceeding 17 µm, indicating its stronger coalescence tendency. Although the area fraction grain size distribution of Grain B (Fig. 55b) covers a wider range of grain sizes, the peak intensity for larger grain sizes is much weaker than for Grain A. These results clearly indicate that grain fragmentation is significantly more extensive in Grain B at this deformation level. The difference between the two grains comes entirely from their different initial orientations, leading to different balances between fragmentation and coalescence during deformation.

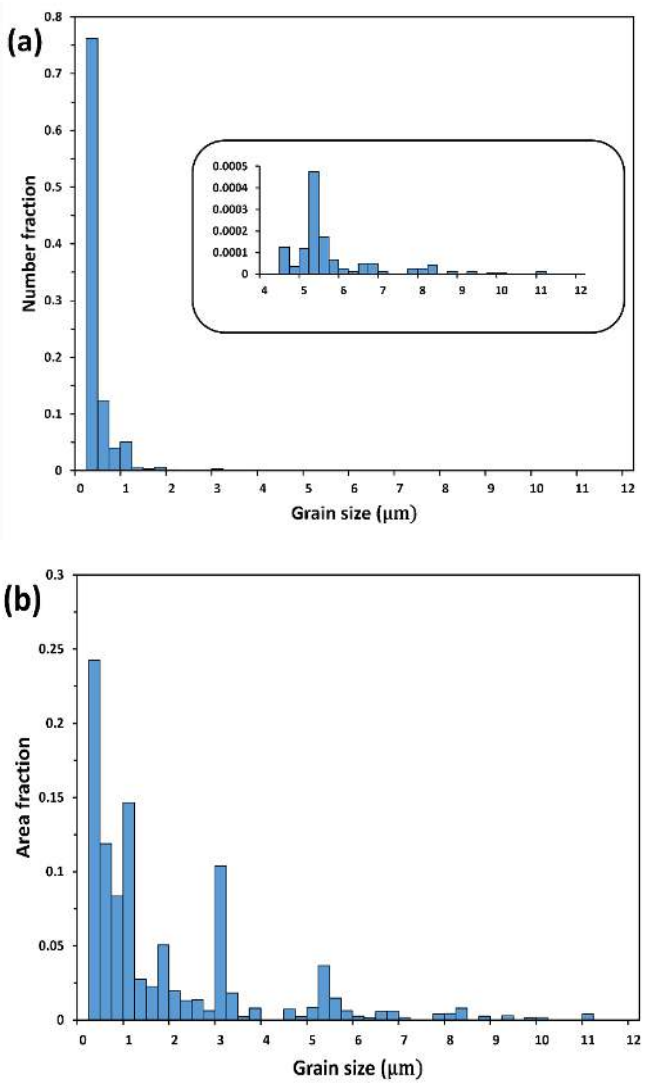

Fig. 55. (a) The number fraction and **(b)** the area fraction grain size distributions of Grain B at ε_{eq} = 4.61 obtained from all 2D sections along the z-direction (bin size = 0.25 µm).

The φ_2 = 0° and 45° sections of the simulated texture for Grain B after ε_{eq} = 4.61 are shown in Fig. 56. Several distinct orientation clusters are observed at this deformation level, forming around the ideal A1, C, A, and Ab orientations. Additionally, a number of grains rotated toward rotated-cube orientations during deformation, leading to the formation of this fiber. In contrast to Grain A, which exhibited a strong and sharply localized C component at this deformation level, the texture of Grain B is distributed over a much wider region of Euler space. The maximum texture intensity of Grain B is also considerably lower than that of Grain A. The texture simulation results demonstrate that grain coalescence was ineffective in Grain B, as fragmented grains rotated to different orientations under the influence of divergence fields, preventing the formation of large, coalesced grains and leading instead to a more uniform fragmented microstructure.

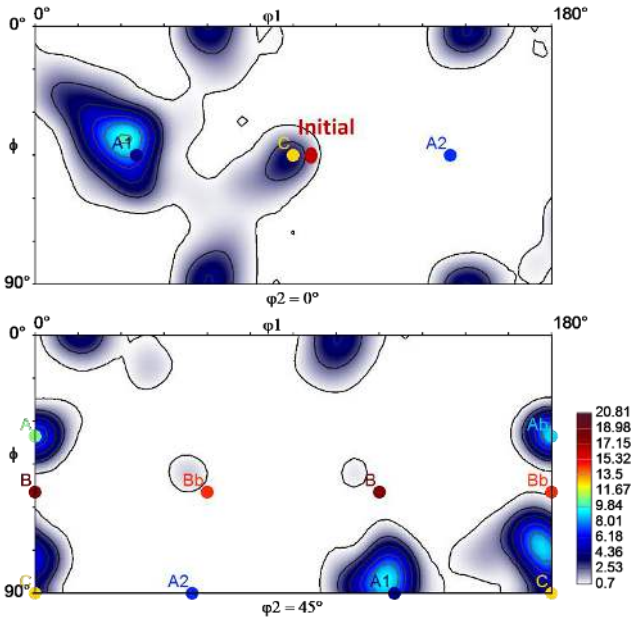

Fig. 56. $\varphi_2 = 0°$ and 45° ODF sections of the simulated textures of Grain B at $\varepsilon_{eq} = 4.61$.

Fig. 57 displays the next-neighbor disorientation distribution of Grain B at $\varepsilon_{eq} = 4.61$. The same procedure used for Grain A was applied here: all z-sections were examined, the representative orientation of each grain was calculated, and the disorientation between neighboring grains was determined using a 1° bin size. Compared with Grain A, the disorientation distribution of Grain B is closer to the random Mackenzie distribution, as a larger portion of the distribution shifts toward higher disorientation angles. Although the highest frequency still occurs at relatively low misorientation angles, the peak intensity is significantly lower than that of Grain A. The enhanced frequency of higher disorientation angles can be attributed to the development of ideal shear components and rotated-cube orientations in Grain B, which are positioned far apart in Euler space. As a result, neighboring grains that belong to different orientation clusters exhibit large disorientation values. The peaks at low disorientation angles arise from neighboring grains that remain within the same orientation cloud and therefore maintain relatively small orientation differences. Overall, the distribution analysis confirms that grain coalescence was limited in Grain B, consistent with the more dispersed texture observed at this strain level.

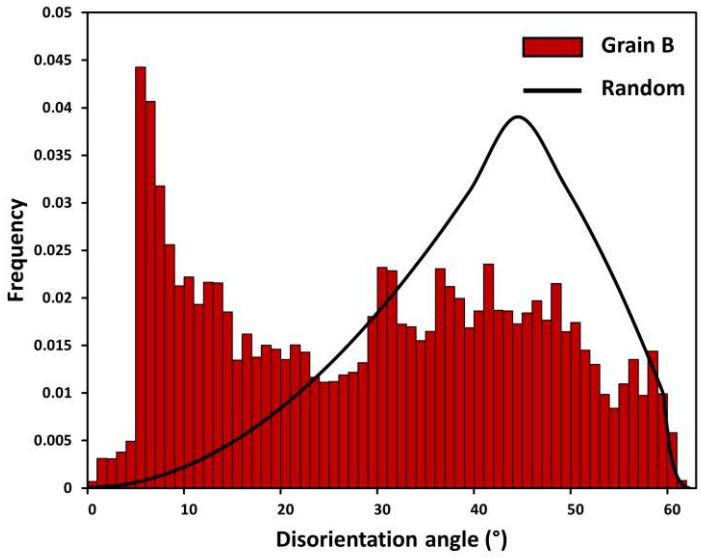

Fig. 57. The next-neighbor disorientation distribution of Grain B at $\varepsilon_{eq} = 4.61$ obtained from all 2D sections along the z-direction (bin size = 1°). The black line shows the random Mackenzie distribution.

The 2D and 3D grain size evolutions of Grain C during deformation up to $\varepsilon_{eq} = 4.61$ are shown in Fig. 58. The 3D grain size evolution displays different stages, in which significant grain coalescence occurs. This trend can also be observed in 2D grain size analysis, but with lower intensity. At first glance, the occurrence of grain coalescence for an initial cube orientation may appear unexpected, since this orientation is known to resist rotation toward the ideal shear positions, where coalescence is typically activated. To understand this phenomenon, the mechanism of internal misorientation development in the grain refinement model must be considered. Notably, the method of subgrain lattice rotation calculation in the present model (Eqs. 46 and 47) not only changes the absolute value of the lattice rotation rate of the subgrain relative to the parent grain but also changes the form of the lattice rotation rate tensor itself. As a result, the lattice rotation vector of the subgrain deviates from that of its parent grain in orientation space. This deviation introduces a local divergence field superimposed on the global rotation field. The presence of this local divergence allows subgrains to escape the rotated-cube fiber, even though the parent orientation remains on this fiber. Through successive fragmentation, a fraction of the resulting subgrains can therefore migrate toward regions close to the ideal shear orientations, leading to grain coalescence. However, the texture simulation results indicate that most grains remain concentrated near the rotated-cube fiber, which is consistent with its semi-stable nature. Therefore, an additional mechanism is required to account for the pronounced grain coalescence occurring around the rotated-cube fiber, as evidenced by the remarkable increase in the 3D grain size observed in simulations.

Based on the grain refinement theory, the contribution of a local convergence field to orientation evolution is possible. This local convergence can develop only between neighboring elements originating from different parent grains. While the parent grains follow the macroscopic lattice rotation rate dictated by the global rotation field, these elements experience distinct lattice rotation rates due to the boundary friction contributions. As a result, some neighboring elements may rotate toward the same position in Euler space, generating a local convergence field. Once this occurs, coalescence is no longer restricted to a single pair of elements; instead, the merging of these elements can lead to the coalescence of their respective parent families, ultimately forming one larger grain. Meanwhile, the region of orientation evolution for the rotated-cube fiber is relatively narrow, owing to the minimal external divergence field in this area, which further increases the possibility of grain coalescence.

In 3D, this mechanism can result in a significant increase in grain size, whereas in 2D analyses, grain coalescence appears much less pronounced. As discussed earlier, the 2D grain size evaluation was performed on the successive z-planes. For orientations located on the rotated-cube fiber, the lattice rotation rate is equal to the rigid body rotation rate, since the plastic spin is zero. In negative simple shear, the rigid body rotation acts in the direction of increasing φ_1, corresponding to a pure rotation around the z-axis. Within the geometrical framework of the present model, misorientation between neighboring elements along the rotated-cube fiber therefore develops predominantly through rotation about the z-axis, thereby promoting the formation of elongated grains parallel to this direction. As the 2D grain size is evaluated on the z-sections, more grain boundaries and a smaller grain size can be observed. Meanwhile, grain coalescence at the rotated-cube fiber requires a rotation around the x-axis in order to change the ϕ angle of fragmented grains to drive them back to the rotated-cube fiber. This rotation could favor grain coalescence parallel to the z-direction, which is captured in 3D analyses but only partially represented in 2D sectioning. As a result, grain coalescence appears significantly stronger in 3D than in 2D for Grain C. An example illustrating these effects is presented in the following section using the simulated microstructures.

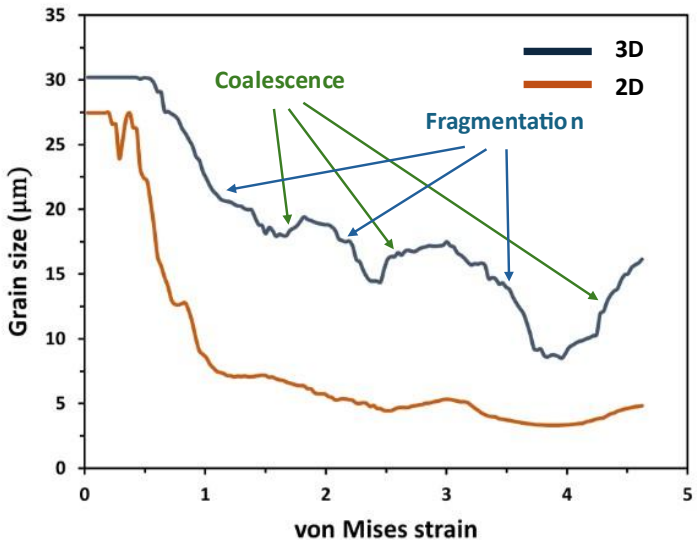

Fig. 58. The 2D and 3D grain size evolutions of Grain C simulation during simple shear deformation up to ε_{eq} = 4.61.

Fig. 59 presents the simulated textures of Grain C at two different strains, ε_{eq} = 3.8 and ε_{eq} = 4.61, corresponding to states before and after the final coalescence stage, respectively. At ε_{eq} = 3.8, the initial cube orientation appears to have completed a full cycle of rotation along the rotated-cube fiber, returning to the cube position. During fragmentation, however, a fraction of grains deviates from the rotated-cube fiber due to the local divergence field introduced by CDRX. This allows them to reach regions close to several ideal shear orientations, such as A1, B, and Bb. With further straining up to ε_{eq} = 4.61, some grains rotate toward the ideal C orientation. At the same time, the intensity of ideal A1, B, and Bb components decreases. Nevertheless, the rotated-cube texture remains the dominant component at both deformation stages. Moreover, the maximum texture intensity increases to 83 at the final strain level, and the orientation cloud near the rotated-cube fiber becomes more localized. These observations indicate that the increase in grain size of Grain C at ε_{eq} = 4.61 is driven predominantly by grain coalescence around the rotated-cube fiber, rather than by coalescence occurring near the ideal shear orientations. This behavior is consistent with the semi-stable nature of the rotated-cube fiber and the local convergence mechanisms enabled by the grain refinement model.

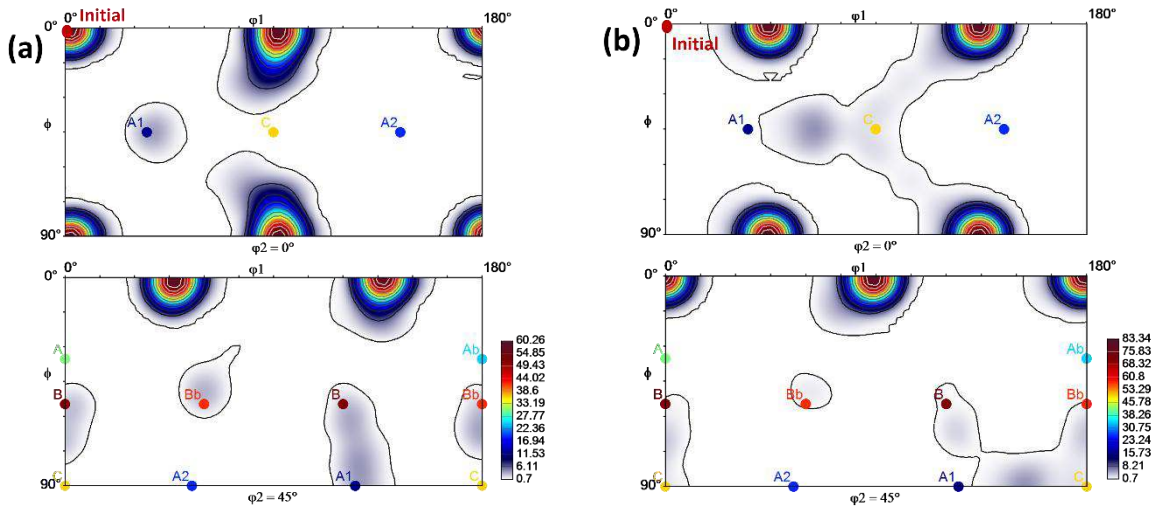

Fig. 59. $\varphi_2 = 0°$ and 45° ODF sections of the simulated textures of Grain C at **(a)** $\varepsilon_{eq} = 3.8$, and **(b)** $\varepsilon_{eq} = 4.61$.

The simulated microstructures of Grain C for two strains of $\varepsilon_{eq} = 3.8$ and $\varepsilon_{eq} = 4.61$ are presented in Fig. 60. To investigate the anisotropic nature of grain fragmentation and coalescence in the rotated-cube fiber, the microstructures were projected on both the x and z planes. As deformation increases from $\varepsilon_{eq} = 3.8$ to $\varepsilon_{eq} = 4.61$, several regions, where grain coalescence occurred, can be detected on the z-section projection. The corresponding microstructures projected on the x-section are shown in Fig. 60c and d. Notably, a number of grains appear elongated along the z-direction, with a particularly pronounced example observed in the central region of the microstructure. As mentioned, for orientations lying on the rotated-cube fiber, the lattice rotation is dominated by rigid body rotation, resulting in a pure rotation around the z-axis. This rotation leads to enhanced grain boundary formation parallel to the z-direction than in other spatial directions, which explains the formation of elongated grains in the z-direction. It should be emphasized that grain shape evolution is not accounted for in the current grain refinement model, and all elements retain cubic geometry throughout deformation. Therefore, the term "elongated grains" does not imply any deformation-induced grain elongation. Indeed, the appearance of such elongated grains is purely driven by the anisotropic nature of grain fragmentation and coalescence in the vicinity of the rotated-cube fiber.

Compared with the z-section microstructure projection, which shows that grain coalescence promotes the formation of relatively elongated grains in the diagonal direction (Fig. 60b), grain coalescence on the x-section preferably takes place along the z-direction, followed by the y-direction. Fig. 60e and f display the fraction of grains with orientations close to the rotated-cube fiber, defined using a 20° disorientation threshold around this fiber, on the same x-section shown in Fig. 60c and d. These maps clearly demonstrate that grain coalescence occurs

predominantly at the rotated-cube fiber, rather than near the ideal shear orientations. This observation confirms that the rotated-cube texture represents an exceptional case in simple shear deformation with respect to grain fragmentation and coalescence behavior. For grain coalescence to occur at the rotated-cube fiber, the fragmented grains must rotate back toward the $\phi = 0°$ or 90° region. Considering that orientation evolutions for such grains happen in a relatively narrow region around the rotated-cube fiber, the corresponding rotation can be approximated as a rotation around the x-axis of the sample, or the x-axis of the original grain in the present geometrical configuration. This rotation primarily facilitates grain coalescence along the z and y directions, consistent with the elongated grain morphologies observed in the simulated microstructure (Fig. 60d).

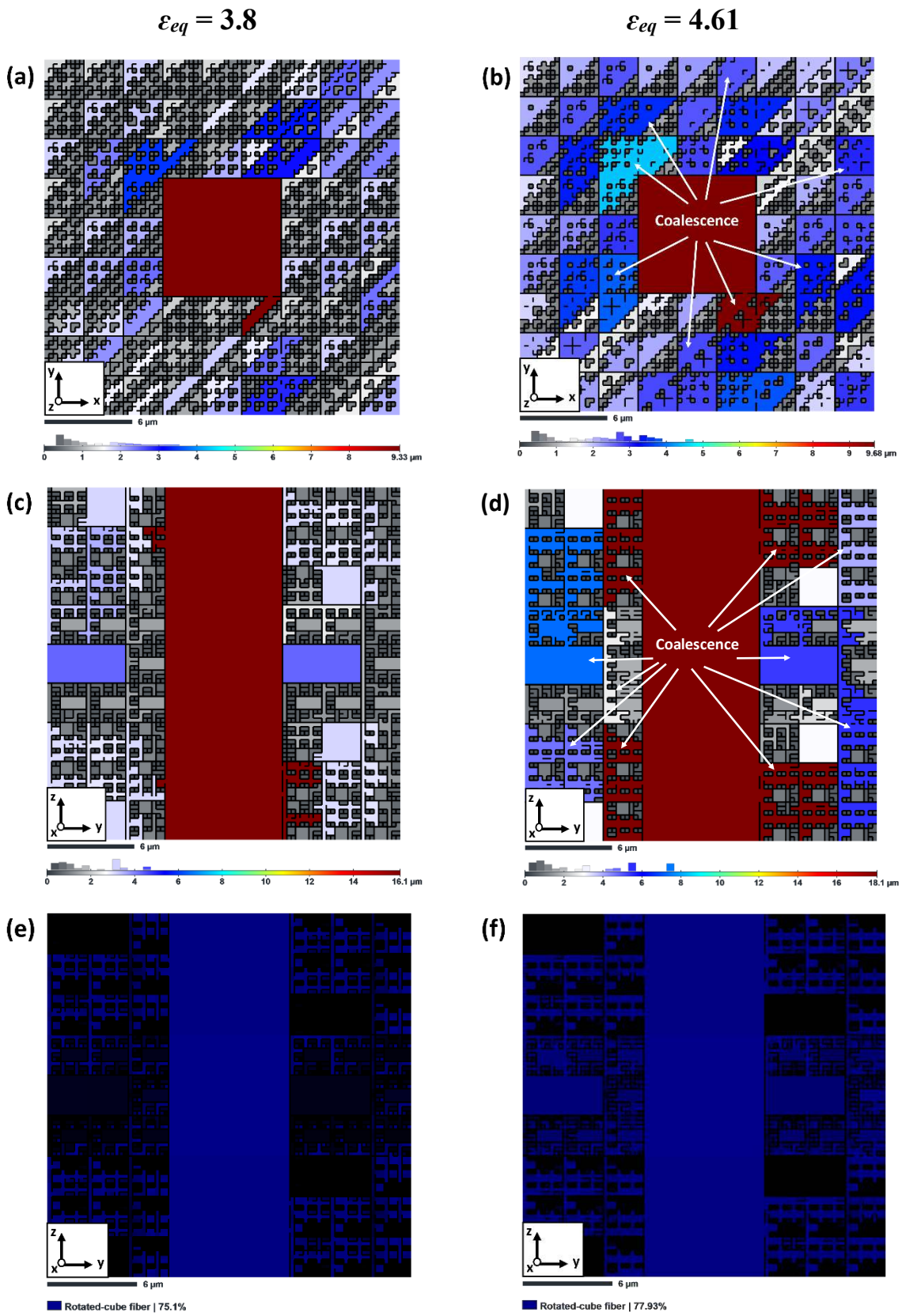

Fig. 60. The simulated microstructure of Grain C projected on a constant z-section for **(a)** ε_{eq} = 3.8, and **(b)** ε_{eq} = 4.61. The simulated microstructure on a constant x-section for **(c)** ε_{eq} = 3.8, and **(d)** ε_{eq} = 4.61 (coloring is based on the grain size). **(e)** and **(f)** the corresponding orientation maps of **(c)** and **(d)**, respectively (The blue color corresponds to grains with the rotated-cube orientation).

Overall, the grain refinement simulations demonstrate that grain fragmentation and coalescence along the rotated-cube fiber follow a distinct mechanism, in which coalescence occurs preferentially near the rotated-cube fiber rather than at the ideal shear positions. This behavior is driven by the local convergent fields resulting from the development of internal misorientations. The local convergent/divergent fields play a critical role in controlling grain refinement along the rotated-cube fiber. However, for orientations near the ideal shear components, these local fields have less impact, as the global convergent/divergent fields are dominant in these regions.

The three initial orientations analyzed using the 4-level grain refinement model correspond to distinct grain refinement behaviors: pronounced grain coalescence (Grain A), extensive grain fragmentation (Grain B), and the rotated-cube fiber as a special case (Grain C). Although these cases provide valuable insights, a comprehensive analysis across the orientation space is required to systematically investigate the dependency of grain refinement on initial orientation and texture evolution. To this end, the $\varphi_2 = 0°$ section of Euler space was selected, and the initial orientations were uniformly distributed with 15° intervals across this section. Simple shear deformation with negative shear sense was imposed up to $\varepsilon_{eq} = 4.61$ (shear strain of 8), using the same model parameters as in the previous simulations. The resulting area-weighted (2D) and volume-weighted (3D) average grain sizes for each orientation at the final strain were used to construct isovalue maps, referred to here as grain refinement maps (Fig. 61). It should be noted that these maps are specific to simple shear deformation at an equivalent strain of 4.61. Nevertheless, the same approach can be applied to other deformation modes and strain levels to generate corresponding grain refinement maps.

Fig. 61a presents the 2D grain refinement map for the $\varphi_2 = 0°$ section. Significant differences in the final grain size are observed across different initial orientations, indicating that grain fragmentation and coalescence are strongly influenced by crystallographic orientation. The largest final 2D grain sizes are obtained for initial orientations located near the A1 and A2 components. In contrast, orientations near the C component result in smaller final grain sizes. The smallest 2D grain sizes correspond to the initial orientations located between the ideal shear components and the rotated-cube fiber.

A relatively similar trend is observed for 3D grain sizes (Fig. 61b). However, the largest 3D grain sizes are obtained for initial orientations located in the region before the A1 component rather than the A2 component. The initial orientation of Grain A, which showed a significant

grain coalescence, corresponds to this region. Moreover, the cube orientation (Grain C) shows a relatively large 3D grain size, reflecting the occurrence of grain coalescence for this grain at the rotated-cube fiber.

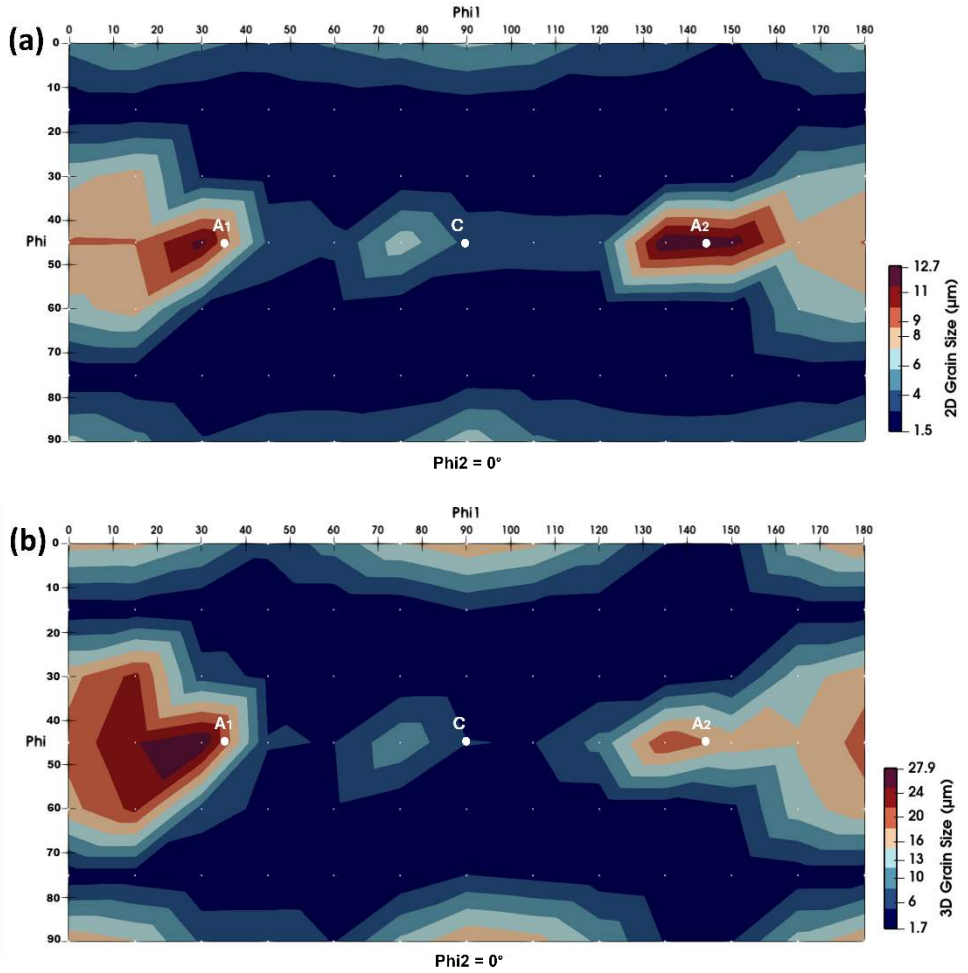

Fig. 61. $\varphi_2 = 0°$ section of the grain refinement map for the negative simple shear at $\varepsilon_{eq} = 4.61$ represented by **(a)** the final 2D, and **(b)** the final 3D grain sizes.

Such grain refinement maps provide a powerful tool for guiding future studies of grain refinement under shear deformation. By illustrating the critical role of texture evolution in controlling grain fragmentation and coalescence, these maps enable the design of targeted microstructures through the appropriate selection of initial orientations and deformation conditions. Depending on the imposed shear strain, it becomes possible to tailor either uniformly refined microstructures or deliberately engineer bimodal microstructures. As an example, for shear deformation up to $\varepsilon_{eq} = 4.61$, an initial shear texture containing high volume fractions of the A1 and C components is expected to promote the formation of a bimodal microstructure, since these two orientations exhibit significantly different grain refinement behaviors.

2.5. Conclusions

A commercially pure copper sample was subjected to severe plastic deformation using the FALEP technique with an extrusion ratio of 8.8. The microstructure and texture after the FALEP process were investigated using the EBSD technique. The FALEP process led to extensive grain refinement through continuous dynamic recrystallization (CDRX). To establish the interrelation between texture evolution and grain refinement in shear deformation, the rotation field and its convergent/divergent characteristics across Euler space, especially in the vicinity of the ideal shear orientations, were analyzed. An existing grain refinement model was further developed by incorporating new algorithms for grain detection and for calculating 2D and 3D average grain sizes at each strain increment. Using this model, the grain refinement behavior across different orientations was examined to highlight the crucial roles of initial orientation and texture evolution in determining the final grain size. Based on the combined experimental observations and simulation results, the following main conclusions can be drawn:

1. After FALEP processing with an extrusion ratio of 8.8, a bimodal microstructure consisting of relatively larger grains embedded within a matrix of well-refined grains was obtained. The larger grains were predominantly located near the ideal shear orientations, whereas the smaller grains were distributed over a broader region of orientation space.
2. The larger grains formed through grain coalescence near the ideal shear orientations, indicating that an increase in grain size by plastic deformation is not limited to the steady-state regime but also occurs actively during CDRX.
3. The divergence and convergence nature of the rotation field plays a crucial role in grain fragmentation and coalescence during CDRX. Divergent fields promote grain fragmentation, while convergent fields facilitate grain coalescence, particularly in the vicinity of ideal shear orientations.
4. The grain refinement simulations revealed that different initial orientations exhibit significantly different fragmentation and coalescence levels, thereby initial orientation is a key factor in determining the final grain size.
5. The rotated-cube fiber represents a special case in grain coalescence theory, as coalescence occurs far from the ideal shear orientations. In this case, grain coalescence is primarily driven by the local convergence field, arising from internal orientation gradients. As the influence of global convergence/divergence fields along the rotated-

cube fiber is minimal, the orientation evolution occurs in a relatively narrow region in Euler space, enhancing the role of local convergence and divergence fields in grain fragmentation and coalescence.

Claims

1. **Gradient microstructure formation in FALEP**

   It has been experimentally demonstrated that FALEP processing of Al-1050 alloy can produce a gradient microstructure across the sheet thickness at almost half (10.5) the previously published extrusion ratio (20). EBSD results show an average grain size of 720 nm near the top surface and 4.2 μm near the bottom surface, with distinct crystallographic textures in the two regions.

2. **Deformation field and texture analysis in FALEP using a new three-stage flow line model**

2.1. The deformation behaviour of the experimental flow lines after the FALEP process at an extrusion ratio of 10.5 exhibits some sharp variations. Three deformation stages can be identified, including two simple shears and a linear convergent extrusion stage in between. This complexity in flow line deformation was not observed in previous studies of other channel angular extrusion processes, such as ECAP and NECAP. Using 2D fluid mechanics kinematics, a new three-stage flow line model has been developed to compute local velocity gradient tensors. When coupled with a polycrystal plasticity framework, the model successfully reproduces experimentally measured textures with accuracies of 86.3 % (upper region) and 77.3 % (bottom region). This confirms that the proposed model can accurately describe the deformation mode and predict the resulting texture evolution in FALEP.

2.2. At larger strains (near equivalent von Mises strain of 3 in the present study), the Taylor model performs better than the self-consistent approach. The Taylor model assumes a uniform deformation mode throughout the polycrystal, meaning all grains deform in the same manner. When the applied strain is considerably large, extensive dynamic recrystallization occurs through the formation of new grain boundaries by the rearrangement of geometrically necessary dislocations (GNDs). Consequently, heterogeneities in deformation are removed, making the deformation more uniform. As the microstructure near the top part of the extruded sheet is more refined and a nearly

equiaxed morphology is obtained, the Taylor model reproduces the experimental texture more accurately. However, near the bottom region of the sheet, where the strain is lower (approximately equivalent von Mises strain of 2), grain fragmentation is less pronounced, and deformation heterogeneity persists. Consequently, the uniform strain assumption becomes less valid, and the self-consistent model provides a better description of the texture evolution.

2.3. The classic simple shear model of angular extrusion fails to predict the strain and deformation field in the FALEP process at an extrusion ratio of 10.5. The simple shear model assumes uniform deformation across the sheet thickness, which makes it impractical for modeling gradient microstructures. While the simple shear model approaches reasonably well at higher extrusion ratios (20), it overestimates the strain at lower extrusion ratios (10.5). The equivalent von Mises strain obtained by the simple shear model for this die geometry is 6.13, which is more than twice that predicted by the new flow line model: 2.98 and 2.03 for the top and bottom regions, respectively. The higher strain in the top region obtained from the new model is consistent with the microstructure evaluation, as the final grain size is considerably smaller in that region. Moreover, the simulated textures generated by the simple shear model are in poor agreement with the measured textures for both the top and bottom regions. Therefore, the simple shear approximation is only applicable at high extrusion ratios (≈20), but becomes invalid at lower ratios, where deformation heterogeneity and gradient microstructure develop.

3. The critical role of texture evolution in grain refinement: fragmentation vs coalescence

3.1. Grain refinement during plastic deformation is not a one-way process. Indeed, the final grain size results from two competing mechanisms: grain fragmentation and grain coalescence; both are strongly dependent on texture evolution. A commercially pure copper sample after the FALEP process exhibited a bimodal microstructure consisting of larger and smaller grains. Larger grains were formed through dynamic grain coalescence and showed ideal shear orientations. The driving force of grain coalescence is the convergence field of texture evolution in which the disorientation between neighboring grains gradually decreases. In the vicinity of ideal orientations, the orientation difference can be smaller than the grain boundary detection angle. Therefore, the grain boundary disappears, and the grains are merged. In contrast, the

divergence field of texture evolution increases the misorientation between the adjacent subgrains, promoting their transformation into new high-angle boundaries and thus grain fragmentation.

3.2. In the context of continuous dynamic recrystallization during severe plastic deformation, grain coalescence is expected to occur when the following conditions are satisfied:

- Prior grain fragmentation
- Neighboring in physical space
- Neighboring in orientation space
- Approaching the ideal positions in orientation space

It is expected that grain coalescence takes place when considerable grain fragmentation has already occurred in the microstructure. Obviously, coalescence is possible for those grains that have common grain boundaries, meaning that they are neighbors. Moreover, the neighboring grains that have large orientation differences are not suitable candidates for grain coalescence. Therefore, the neighboring condition should also exist in the orientation space, meaning that the disorientation between the grains is not too sharp. Furthermore, coalescence is only permitted near the ideal orientations, where the rotation field is convergent, and the lattice rotation rate is low. Continuous dynamic recrystallization (CDRX) inherently satisfies the first three conditions as the fragmented grains are physically adjacent and their orientations are correlated with the original grain orientation, meaning they are also neighbors in the orientation space. Coalescence is therefore activated only when the fourth condition is reached, i.e., when the grains enter a convergent rotation field and reach near the ideal positions. This demonstrates that grain coalescence is an intrinsic stage of the CDRX mechanism driven by texture evolution.

3.3. The rotated-cube fiber is an exception in grain coalescence theory. Although no individual orientation along this fiber is stable, when the whole fiber is considered, it exhibits a form of relative stability during simple shear deformation. Despite being located far from the ideal shear positions in Euler space, grain coalescence can still occur along the rotated-cube fiber. The driving force for grain coalescence along the rotated-cube fiber is the local convergence fields generated by internal misorientation gradients. The weak external convergence/divergence fields along the rotated-cube

fiber keep the orientation evolutions within a narrow Euler space zone. As a result, the role of local convergence/divergence fields in grain fragmentation and coalescence along the rotated-cube fiber becomes pronounced.

4. **Fully quantitative 3D and 2D grain fragmentation and grain coalescence analyses by an optimized 4-level grain refinement model**

   An existing 4-level grain subdivision model was extended by implementing 3D and 2D grain detection algorithms. For the first time, the model enables the detection of grains and the determination of grain size in both 2D and 3D at each strain level by considering the topological connections between grains in physical space. From the outputs of this model, the following analyses can be done:

   - Number of grains in 3D
   - Average grain size in 2D and 3D
   - Grain size distribution
   - Number of fragmented and coalesced boundaries
   - Deformation texture
   - Disorientation distribution
   - Microstructure simulation

   The simulation results reveal that the 3D grain size is systematically larger than its 2D projection because neighboring grains may remain connected in the third direction, a factor typically neglected in EBSD-based 2D characterizations. Using the new model, quantitative analysis of grain fragmentation and grain coalescence is possible. The simulation results show that grain coalescence occurs near the ideal orientations, where the rotation field is convergent, and the lattice rotation rate is minimal, with the exception of the rotated-cube fiber. Moreover, the initial orientation plays a critical role in the level of grain fragmentation and grain coalescence. Under the same deformation conditions, different initial orientations can result in significantly different final grain sizes, indicating that the nature of texture evolution is a crucial factor in grain refinement.

Claims Practical Applications

The findings of the first part of this study provide important insights into the deformation mode and material flow during the FALEP process, which is a promising technique for the industrial production of large-scale ultrafine-grained alloys. In this work, the deformation field, texture evolution, and microstructure development during FALEP processing were systematically investigated using a combination of experimental characterization and polycrystal plasticity simulations. Because FALEP is a relatively new SPD technique, only limited studies have addressed its deformation mechanics and microstructure evolution. The present study, therefore, provides a detailed analysis of several key aspects of the FALEP process, including the influence of extrusion ratio on strain distribution, microstructure homogeneity, and crystallographic texture evolution. The results offer practical guidance for future applications of FALEP, particularly for designing either uniform or gradient microstructures by selecting appropriate processing parameters.

The second part of this study focuses on the fundamental mechanisms governing grain refinement during severe plastic deformation. Based on experimental observations of copper samples processed by FALEP, a four-level fractal grain refinement model was optimized to analyze microstructure evolution during large shear deformation. This model, for the first time, enables the simultaneous detection of both grain fragmentation and grain coalescence at each strain increment. Furthermore, the study systematically demonstrates the significant role of crystallographic texture in controlling grain size evolution. The results, including the grain refinement map developed in this work, provide a practical tool for future studies aiming to design either bimodal or uniformly refined microstructures through appropriate selection of the initial texture. This approach can significantly reduce the time and energy required for microstructure design by minimizing the need for repeated large-scale simulations and costly experimental trials.

Publications and Presentations

1. **Amininejad, A**., Toth, L. S., Sepsi, M., Szucs, M., Kumaran, S. N., and Mertinger, V. (2025). Deformation field and texture analysis in friction-assisted lateral extrusion of aluminum. *Materials Characterization*, 223, 114920.

2. **Amininejad, A**., Toth, L., and Mertinger, V. (2025). Modeling of deformation mode in ECAP variant techniques. *Doktorandusz Almanach*, vol. 1.

3. **OATK 2023**, Modeling of deformation field in the friction-assisted lateral extrusion process. **Amininejad, A**., Sepsi, M., Szucs, M., Toth, L. S., and Mertinger, V. Poster Presentation.

4. **ICOTOM 2024**, A new flow line approach for modeling the deformation field and texture in FALEP. **Amininejad, A**., Toth, L. S., Mertinger, V., Szucs, M., and Sepsi, M. Oral Presentation.

5. **ISCAME 2024**, On the role of crystallographic texture in grain fragmentation during severe plastic deformation. **Amininejad, A**., Szucs, M., Toth, L. S., and Mertinger, V. Oral Presentation.

AI Usage Statement

I, the undersigned Ali Amininejad, declare that the results presented in the report are based on my own work. If I used artificial intelligence to write the report, I always indicated in a footnote what kind of tool I used and for what purpose.

Miskolc, 2026.03.17

References

[1] U. Kocks, The relation between polycrystal deformation and single-crystal deformation, Metallurgical Transactions 1(5) (1970) 1121-1143.
[2] D. Kuhlmann-Wilsdorf, The theory of dislocation-based crystal plasticity, Philosophical Magazine A 79(4) (1999) 955-1008.
[3] J. Chakrabarty, Theory of plasticity, Elsevier (2012).
[4] R. Asaro, V. Lubarda, Mechanics of solids and materials, Cambridge University Press (2006).
[5] G.I. Taylor, Plastic strain in metals, J. Inst. Metals 62 (1938) 307-324.
[6] R. Armstrong, S. Walley, High strain rate properties of metals and alloys, International Materials Reviews 53(3) (2008) 105-128.
[7] Y. Cao, B. Karlsson, J. Ahlström, Temperature and strain rate effects on the mechanical behavior of dual phase steel, Materials Science and Engineering: A 636 (2015) 124-132.
[8] J.W. Hutchinson, Bounds and self-consistent estimates for creep of polycrystalline materials, Proceedings of the Royal Society of London. A. Mathematical and Physical Sciences 348(1652) (1976) 101-127.
[9] G. Canova, C. Fressengeas, A. Molinari, U. Kocks, Effect of rate sensitivity on slip system activity and lattice rotation, Acta Metallurgica 36(8) (1988) 1961-1970.
[10] G. Sachs, Zur ableitung einer fliessbedingung, Z. Ver, Dtsch. Ing. 72 (1928) 734-736.
[11] R. Hill, Continuum micro-mechanics of elastoplastic polycrystals, Journal of the Mechanics and Physics of Solids 13(2) (1965) 89-101.
[12] P. Van Houtte, Simulation of the rolling and shear texture of brass by the Taylor theory adapted for mechanical twinning, Acta Metallurgica 26(4) (1978) 591-604.
[13] R.A. Lebensohn, C.N. Tomé, A self-consistent anisotropic approach for the simulation of plastic deformation and texture development of polycrystals: application to zirconium alloys, Acta metallurgica et materialia 41(9) (1993) 2611-2624.
[14] A. Molinari, G. Canova, S. Ahzi, A self consistent approach of the large deformation polycrystal viscoplasticity, Acta Metallurgica 35(12) (1987) 2983-2994.
[15] A. Molinari, L. Tóth, Tuning a self consistent viscoplastic model by finite element results—I. Modeling, Acta Metallurgica et Materialia 42(7) (1994) 2453-2458.
[16] R.Z. Valiev, Y. Estrin, Z. Horita, T.G. Langdon, M.J. Zechetbauer, Y.T. Zhu, Producing bulk ultrafine-grained materials by severe plastic deformation, Jom 58(4) (2006) 33-39.
[17] K. Edalati, A. Bachmaier, V.A. Beloshenko, Y. Beygelzimer, V.D. Blank, W.J. Botta, K. Bryła, J. Čížek, S. Divinski, N.A. Enikeev, Nanomaterials by severe plastic deformation: review of historical developments and recent advances, Materials Research Letters 10(4) (2022) 163-256.
[18] T.G. Langdon, Twenty-five years of ultrafine-grained materials: Achieving exceptional properties through grain refinement, Acta Materialia 61(19) (2013) 7035-7059.
[19] R.Z. Valiev, Superior strength in ultrafine-grained materials produced by SPD processing, Materials Transactions 55(1) (2014) 13-18.
[20] K. Edalati, Review on recent advancements in severe plastic deformation of oxides by high-pressure torsion (HPT), Advanced Engineering Materials 21(1) (2019) 1800272.
[21] N. Boucharat, R. Hebert, H. Rösner, R. Valiev, G. Wilde, Synthesis routes for controlling the microstructure in nanostructured Al88Y7Fe5 alloys, Journal of alloys and compounds 434 (2007) 252-254.
[22] A. Zharov, Reactivity of monomers and other organic compounds in the solid state under high pressure and shear deformation, Polymer science. Series B 46(9-10) (2004) 268-287.
[23] Y. Ikoma, T. Yamasaki, T. Masuda, Y. Tange, Y. Higo, Y. Ohishi, M.R. McCartney, D.J. Smith, Z. Horita, Synchrotron X-ray diffraction observation of phase transformation during annealing of Si processed by high-pressure torsion, Philosophical Magazine Letters 101(6) (2021) 223-231.
[24] P.W. Bridgman, Effects of high shearing stress combined with high hydrostatic pressure, Physical review 48(10) (1935) 825.
[25] K. Edalati, Metallurgical alchemy by ultra-severe plastic deformation via high-pressure torsion process, Materials Transactions 60(7) (2019) 1221-1229.
[26] L. Tóth, M. Arzaghi, J. Fundenberger, B. Beausir, O. Bouaziz, R. Arruffat-Massion, Severe plastic deformation of metals by high-pressure tube twisting, Scripta Materialia 60(3) (2009) 175-177.

[27] M. Arzaghi, J. Fundenberger, L. Toth, R. Arruffat, L. Faure, B. Beausir, X. Sauvage, Microstructure, texture and mechanical properties of aluminum processed by high-pressure tube twisting, Acta materialia 60(11) (2012) 4393-4408.
[28] C. Xu, Z. Horita, T.G. Langdon, The evolution of homogeneity in an aluminum alloy processed using high-pressure torsion, Acta materialia 56(18) (2008) 5168-5176.
[29] V. Segal, Methods of stress-strain analysis in metalforming, Physical Technical Institute Academy of Sciences of Buelorussia, Minsk, Russia (1974)
[30] V. Segal, Materials preparation for following processing, USSR Invention Certificate 575 (1977) 892.
[31] R. Valiev, A. Korznikov, R. Mulyukov, Structure and properties of ultrafine-grained materials produced by severe plastic deformation, Materials Science and Engineering: A 168(2) (1993) 141-148.
[32] T.C. Lowe, R.Z. Valiev, Investigations and applications of severe plastic deformation, Springer Science & Business Media (2000).
[33] R.Z. Valiev, T.G. Langdon, Principles of equal-channel angular pressing as a processing tool for grain refinement, Progress in materials science 51(7) (2006) 881-981.
[34] V. Segal, Slip line solutions, deformation mode and loading history during equal channel angular extrusion, Materials Science and Engineering: A 345(1-2) (2003) 36-46.
[35] W. Skrotzki, N. Scheerbaum, C. Oertel, H.G. Brokmeier, S. Suwas, L.S. Tóth, Oblique cube texture formation in high purity aluminum during equal channel angular pressing, Solid State Phenomena 105 (2005) 351-356.
[36] W. Skrotzki, Deformation heterogeneities in equal channel angular pressing, Materials transactions 60(7) (2019) 1331-1343.
[37] R.Y. Lapovok, The role of back-pressure in equal channel angular extrusion, Journal of materials science 40(2) (2005) 341-346.
[38] P.W.J. Mckenzie, R. Lapovok, Y. Estrin, The influence of back pressure on ECAP processed AA 6016: Modeling and experiment, Acta Materialia 55(9) (2007) 2985-2993.
[39] G.J. Raab, R.Z. Valiev, T.C. Lowe, Y.T. Zhu, Continuous processing of ultrafine grained Al by ECAP–Conform, Materials Science and Engineering: A 382(1-2) (2004) 30-34.
[40] L.S. Tóth, R. Lapovok, A. Hasani, C. Gu, Non-equal channel angular pressing of aluminum alloy, Scripta Materialia 61(12) (2009) 1121-1124.
[41] C. Gu, L.S. Toth, Texture development and grain refinement in non-equal-channel angular-pressed Al, Scripta Materialia 67(1) (2012) 33-36.
[42] H.S. Kim, Finite element analysis of deformation behaviour of metals during equal channel multi-angular pressing, Materials Science and Engineering: A 328(1-2) (2002) 317-323.
[43] Y. Nishida, H. Arima, J.-C. Kim, T. Ando, Rotary-die equal-channel angular pressing of an Al–7 mass% Si–0.35 mass% Mg alloy, Scripta materialia 45(3) (2001) 261-266.
[44] C.-Y. Chou, S.-L. Lee, J.-C. Lin, C.-M. Hsu, Effects of cross-channel extrusion on the microstructures and superplasticity of a Zn–22 wt.% Al eutectoid alloy, Scripta Materialia 57(10) (2007) 972-975.
[45] V.S. Rao, B. Kashyap, N. Prabhu, P. Hodgson, T-shaped equi-channel angular pressing of Pb–Sn eutectic and its tensile properties, Materials Science and Engineering: A 486(1-2) (2008) 341-349.
[46] A. Hasani, M. Sepsi, S. Feyzi, L. Toth, Deformation field and texture analysis in T-ECAP using a flow function, Materials Characterization 173 (2021) 110912.
[47] K. Edalati, A.Q. Ahmed, S. Akrami, K. Ameyama, V. Aptukov, R.N. Asfandiyarov, M. Ashida, V. Astanin, A. Bachmaier, V. Beloshenko, Severe plastic deformation for producing superfunctional ultrafine-grained and heterostructured materials: an interdisciplinary review, Journal of Alloys and Compounds 1002 (2024) 174667.
[48] P.B. Berbon, M. Furukawa, Z. Horita, M. Nemoto, T.G. Langdon, Influence of pressing speed on microstructural development in equal-channel angular pressing, Metallurgical and Materials Transactions A 30(8) (1999) 1989-1997.
[49] V. Segal, Materials processing by simple shear, Materials Science and Engineering: A 197(2) (1995) 157-164.
[50] V. Segal, Equal channel angular extrusion: from macromechanics to structure formation, Materials Science and Engineering: A 271(1-2) (1999) 322-333.

[51] Y. Iwahashi, Z. Horita, M. Nemoto, J. Wang, T.G. Langdon, Principle of equal-channel angular pressing for the processing of ultra-fine grained materials, Scripta materialia 35(2) (1996)
[52] L.S. Tóth, R.A. Massion, L. Germain, S.C. Baik, S. Suwas, Analysis of texture evolution in equal channel angular extrusion of copper using a new flow field, Acta Materialia 52(7) (2004) 1885-1898.
[53] D.N. Lee, An upper-bound solution of channel angular deformation, Scripta materialia 43(2) (2000) 115-118.
[54] A. Hasani, L.S. Tóth, B. Beausir, Principles of nonequal channel angular pressing, (2010)
[55] I.J. Beyerlein, L.S. Tóth, Texture evolution in equal-channel angular extrusion, Progress in Materials Science 54(4) (2009) 427-510.
[56] S. Li, I.J. Beyerlein, M.A. Bourke, Texture formation during equal channel angular extrusion of fcc and bcc materials: comparison with simple shear, Materials Science and Engineering: A 394(1-2) (2005) 66-77.
[57] I. Beyerlein, R. Lebensohn, C. Tomé, Modeling texture and microstructural evolution in the equal channel angular extrusion process, Materials Science and Engineering: A 345(1-2) (2003) 122-138.
[58] C. Zhu, F. Du, Q. Jiao, X. Wang, A. Chen, F. Liu, D. Pan, Microstructure and strength of pure Cu with large grains processed by equal channel angular pressing, Materials & Design (1980-2015) 52 (2013) 23-29.
[59] M. Ebrahimi, C. Gode, Severely deformed copper by equal channel angular pressing, Progress in Natural Science: Materials International 27(2) (2017) 244-250.
[60] N. Berndt, N.A. Reiser, M.F.-X. Wagner, Evolution of plastic deformation during multi-pass ECAP of an AA6060 aluminum alloy–An experimental flow line analysis, Journal of Materials Research and Technology 34 (2025) 359-371.
[61] C. Xu, M. Furukawa, Z. Horita, T.G. Langdon, The evolution of homogeneity and grain refinement during equal-channel angular pressing: A model for grain refinement in ECAP, Materials Science and Engineering: A 398(1-2) (2005) 66-76.
[62] S. Yoon, P. Quang, S. Hong, H. Kim, Die design for homogeneous plastic deformation during equal channel angular pressing, Journal of Materials Processing Technology 187 (2007) 46-50.
[63] R. Srinivasan, Computer simulation of the equichannel angular extrusion (ECAE) process, Scripta Materialia 44(1) (2001) 91-96.
[64] E. Cerri, P. De Marco, P. Leo, FEM and metallurgical analysis of modified 6082 aluminium alloys processed by multipass ECAP: Influence of material properties and different process settings on induced plastic strain, journal of materials processing technology 209(3) (2009) 1550-1564.
[65] C. Su, L. Lu, M. Lai, 3D finite element analysis on strain uniformity during ECAP process, Materials science and technology 23(6) (2007) 727-735.
[66] A. Perig, I.S. Galan, The experimental verification of the known flow line models describing local flow during ECAE (ECAP), Letters on materials 7(3) (2017) 209-217.
[67] A. Hasani, R. Lapovok, L.S. Tóth, A. Molinari, Deformation field variations in equal channel angular extrusion due to back pressure, Scripta Materialia 58(9) (2008) 771-774.
[68] I.J. Beyerlein, C.N. Tomé, Analytical modeling of material flow in equal channel angular extrusion (ECAE), Materials Science and Engineering: A 380(1-2) (2004) 171-190.
[69] A. Hasani, L.S. Tóth, A fan-type flow-line model in equal channel angular extrusion, Scripta Materialia 61(1) (2009) 24-27.
[70] R. Arruffat-Massion, L.S. Toth, J.-P. Mathieu, Modeling of deformation and texture development of copper in a 120 ECAE die, Scripta Materialia 54(9) (2006) 1667-1672.
[71] A. Hasani, L. Toth, S. Mardokh Rouhani, A New Flow Line Function for Modeling Material Trajectory and Textures in Nonequal-Channel Angular Pressing, Advances in Materials Science and Engineering 2019(1) (2019) 5682585.
[72] A. Hasani, L.S. Toth, Deformation field analysis in equal channel angular extrusion of metals using asymmetric flow function, Advanced Engineering Materials 17(12) (2015) 1760-1772.
[73] M.-X. Wagner, N. Nostitz, S. Frint, P. Frint, J. Ihlemann, Plastic flow during equal-channel angular pressing with arbitrary tool angles, International Journal of Plasticity 134 (2020) 102755.
[74] T. Nakamura, S. Tanaka, M. Hiraiwa, H. Imaizumi, Y. Tomizawa, K. Osakada, Friction—assisted extrusion of thin strips of aluminium composite material from powder metals, CIRP annals 41(1) (1992) 281-284.

[75] T. Nakamura, M. Hiraiwa, H. Imaizumi, Y. Tomizawa, Development of friction-assisted extrusion process for producing thin metal strips, JSME international journal. Ser. C, Dynamics, control, robotics, design and manufacturing 38(1) (1995) 143-148.
[76] V.Q. Vu, L.S. Toth, Y. Beygelzimer, Y. Zhao, Microstructure, texture and mechanical properties in aluminum produced by friction-assisted lateral extrusion, Materials 14(9) (2021) 2465.
[77] L.S. Tóth, M. Sepsi, M. Szűcs, S.N. Kumaran, T.C. Lowe, The mechanics of the friction-assisted lateral extrusion process, Journal of Materials Science 59(14) (2024) 6059-6074.
[78] A. Pariyar, V.Q. Vu, S.V. Kailas, L.S. Toth, Room-temperature single-step production of ultrafine-grained bulk metallic sheets from Al powder, Journal of Manufacturing Science and Engineering 145(10) (2023) 101001.
[79] C.L. Adams, M. Sepsi, S.N. Kumaran, L.S. Toth, D.P. Field, Residual stresses in multilayered aluminum sheets produced by the friction assisted lateral extrusion process, Materials Characterization 219 (2025) 114653.
[80] B. Beausir, J. Fundenberger, Analysis Tools for Electron and X-ray diffraction, ATEX-software, www. atex-software. eu, Université de Lorraine-Metz 201(7) (2017)
[81] L. Toth, C. Gu, B. Beausir, J.J. Fundenberger, M. Hoffman, Geometrically necessary dislocations favor the Taylor uniform deformation mode in ultra-fine-grained polycrystals, Acta Materialia 117 (2016) 35-42.
[82] C. Gu, M. Hoffman, L.S. Toth, Y.D. Zhang, Grain size dependent texture evolution in severely rolled pure copper, Materials Characterization 101 (2015) 180-188.
[83] C. Chen, Y. Beygelzimer, L.S. Toth, J.-J. Fundenberger, Microstructure and strain in protrusions formed during severe plastic deformation of aluminum, Materials Letters 159 (2015) 253-256.
[84] R.Z. Valiev, R.K. Islamgaliev, I.V. Alexandrov, Bulk nanostructured materials from severe plastic deformation, Progress in materials science 45(2) (2000) 103-189.
[85] E. Hall, The deformation and ageing of mild steel: III discussion of results, Proceedings of the Physical Society. Section B 64(9) (1951) 747.
[86] F.J. Humphreys, M. Hatherly, Recrystallization and related annealing phenomena, elsevier (2012).
[87] O. Rezvanian, M. Zikry, A. Rajendran, Statistically stored, geometrically necessary and grain boundary dislocation densities: microstructural representation and modelling, Proceedings of the Royal Society A: Mathematical, Physical and Engineering Sciences 463(2087) (2007) 2833-2853.
[88] S. Naghdy, P. Verleysen, R. Petrov, L. Kestens, Resolving the geometrically necessary dislocation content in severely deformed aluminum by transmission Kikuchi diffraction, Materials Characterization 140 (2018) 225-232.
[89] A. Shabani, M.R. Toroghinejad, M. Aminaei, P. Cavaliere, Dynamic recrystallization nanoarchitectonics of FeCrCuMnNi multi-phase high entropy alloy, Journal of Alloys and Compounds 968 (2023) 172001.
[90] M. Suresh, A. Sharma, A. More, R. Kalsar, A. Bisht, N. Nayan, S. Suwas, Effect of equal channel angular pressing (ECAP) on the evolution of texture, microstructure and mechanical properties in the Al-Cu-Li alloy AA2195, Journal of Alloys and Compounds 785 (2019) 972-983.
[91] R. Pippan, S. Scheriau, A. Taylor, M. Hafok, A. Hohenwarter, A. Bachmaier, Saturation of fragmentation during severe plastic deformation, Annual Review of Materials Research 40(1) (2010) 319-343.
[92] O. Renk, A. Hohenwarter, S. Wurster, R. Pippan, Direct evidence for grain boundary motion as the dominant restoration mechanism in the steady-state regime of extremely cold-rolled copper, Acta materialia 77 (2014) 401-410.
[93] O. Renk, R. Pippan, Saturation of grain refinement during severe plastic deformation of single phase materials: reconsiderations, current status and open questions, Materials transactions 60(7) (2019) 1270-1282.
[94] Y. Ivanisenko, W. Skrotzki, R. Chulist, T. Lippmann, K. Yang, L. Kurmanaeva, H.-J. Fecht, Information on deformation mechanisms in nanocrystalline Pd–10% Au inferred from texture analysis, Journal of materials science 45(17) (2010) 4571-4577.
[95] Y.B. Wang, J.C. Ho, X.Z. Liao, H.Q. Li, S.P. Ringer, Y.T. Zhu, Mechanism of grain growth during severe plastic deformation of a nanocrystalline Ni-Fe alloy, Applied Physics Letters 94(1) (2009).
[96] Y.B. Wang, B.Q. Li, M.L. Sui, S.X. Mao, Deformation-induced grain rotation and growth in nanocrystalline Ni, Applied Physics Letters 92(1) (2008).

[97] Q. Zhu, G. Cao, J. Wang, C. Deng, J. Li, Z. Zhang, S.X. Mao, In situ atomistic observation of disconnection-mediated grain boundary migration, Nature communications 10(1) (2019) 156.
[98] M. Jin, A. Minor, E. Stach, J. Morris Jr, Direct observation of deformation-induced grain growth during the nanoindentation of ultrafine-grained Al at room temperature, Acta Materialia 52(18) (2004) 5381-5387.
[99] M. Legros, D.S. Gianola, K.J. Hemker, In situ TEM observations of fast grain-boundary motion in stressed nanocrystalline aluminum films, Acta Materialia 56(14) (2008) 3380-3393.
[100] S. Naghdy, H. Pirgazi, P. Verleysen, R. Petrov, L. Kestens, Morphological and crystallographic anisotropy of severely deformed commercially pure aluminium by three-dimensional electron backscatter diffraction, Applied Crystallography 50(5) (2017) 1512-1523.
[101] A. Khalfallah, H. Azzeddine, T. Baudin, F. Brisset, Y. Huang, T.G. Langdon, Texture and microstructural evolution in an Al-6061 alloy processed by high-pressure torsion, Materials Characterization 212 (2024) 114020.
[102] S. Gourdet, F. Montheillet, A model of continuous dynamic recrystallization, Acta Materialia 51(9) (2003) 2685-2699.
[103] K. Frydrych, K. Kowalczyk-Gajewska, A three-scale crystal plasticity model accounting for grain refinement in fcc metals subjected to severe plastic deformations, Materials Science and Engineering: A 658 (2016) 490-502.
[104] K. Frydrych, K. Kowalczyk-Gajewska, Grain refinement in the equal channel angular pressing process: simulations using the crystal plasticity finite element method, Modelling and Simulation in Materials Science and Engineering 26(6) (2018) 065015.
[105] X. Liu, J. Zhu, Y. He, H. Jia, B. Li, G. Fang, State-of-the-art review of the simulation of dynamic recrystallization, Metals 14(11) (2024) 1230.
[106] M. Azarbarmas, Modeling the Dynamic Recrystallization by Using Cellular Automaton: The Current Status, Challenges and Future Prospects, Iran J Mater Sci Eng 17(4) (2020) 103-129.10.22068/ijmse.17.4.11.
[107] N. Yazdipour, C.H. Davies, P.D. Hodgson, Microstructural modeling of dynamic recrystallization using irregular cellular automata, Computational Materials Science 44(2) (2008) 566-576.
[108] M. Azarbarmas, S.S. Mirjavadi, A. Ghasemi, A.M. Hamouda, A combined method to model dynamic recrystallization based on cellular automaton and a phenomenological (CAP) approach, Metals 8(11) (2018) 923.
[109] D.S. Svyetlichnyy, K. Muszka, J. Majta, Three-dimensional frontal cellular automata modeling of the grain refinement during severe plastic deformation of microalloyed steel, Computational Materials Science 102 (2015) 159-166.
[110] L.S. Tóth, Y. Estrin, R. Lapovok, C. Gu, A model of grain fragmentation based on lattice curvature, Acta Materialia 58(5) (2010) 1782-1794.
[111] D. Raabe, Z. Zhao, S.-J. Park, F. Roters, Theory of orientation gradients in plastically strained crystals, Acta Materialia 50(2) (2002) 421-440.
[112] M. Barnett, F. Montheillet, The generation of new high-angle boundaries in aluminium during hot torsion, Acta materialia 50(9) (2002) 2285-2296.
[113] C. Gu, L.S. Toth, S. Rusz, M. Bova, Texture induced grain coarsening in severe plastic deformed low carbon steel, Scripta Materialia 86 (2014) 36-39.
[114] C. Zhang, L.S. Toth, Polycrystal simulation of texture-induced grain coarsening during severe plastic deformation, Materials 13(24) (2020) 5834.
[115] H.H. Bernardi, H.R.Z. Sandim, K.D. Zilnyk, B. Verlinden, D. Raabe, Microstructural stability of a niobium single crystal deformed by equal channel angular pressing, Materials Research 20(5) (2017) 1238-1247.
[116] S.-S. Rui, L.-S. Niu, H.-J. Shi, S. Wei, C.C. Tasan, Diffraction-based misorientation mapping: A continuum mechanics description, Journal of the Mechanics and Physics of Solids 133 (2019) 103709.
[117] L. Toth, P. Gilormini, J. Jonas, Effect of rate sensitivity on the stability of torsion textures, Acta Metallurgica 36(12) (1988) 3077-3091.
[118] U. Ayachit, The paraview guide: a parallel visualization application, Kitware, Inc. (2015).
[119] L. Tóth, K. Neale, J. Jonas, Stress response and persistence characteristics of the ideal orientations of shear textures, Acta Metallurgica 37(8) (1989) 2197-2210.

[120] S. Li, Orientation stability in equal channel angular extrusion. Part I: Face-centered cubic and body-centered cubic materials, Acta materialia 56(5) (2008) 1018-1030.
[121] H. Pirgazi, On the alignment of 3D EBSD data collected by serial sectioning technique, Materials Characterization 152 (2019) 223-229.
[122] G. Rohrer, J. Li, S. Lee, A. Rollett, M. Groeber, M. Uchic, Deriving grain boundary character distributions and relative grain boundary energies from three-dimensional EBSD data, Materials Science and Technology 26(6) (2010) 661-669.